GEOMETRICALLY EXPLICIT FINITE ELEMENT MODELING OF AA7075-T651 MICROSTRUCTURE WITH FATIGUE CRACKS

A Dissertation

Presented to the Faculty of the Graduate School

of Cornell University

in Partial Fulfillment of the Requirements for the Degree of

Doctor of Philosophy

by

Michael Gilbert Veilleux

January 2011

GEOMETRICALLY EXPLICIT FINITE ELEMENT MODELING OF AA7075-T651 MICROSTRUCTURE WITH FATIGUE CRACKS

Michael Gilbert Veilleux, Ph.D.

Cornell University 2011

This dissertation is divided into three chapters, where each is an independent paper intended to be submitted as a refereed journal article. The main thrust of the research project overarching all three papers is to develop a high fidelity, geometrically explicit approach to finite element modeling fatigue at the microstructural length scale. Each paper is a study within this thrust, and the following is a sweeping overview of each study. More detailed abstracts for each paper are given at the beginning of each chapter.

The paper in the first chapter is the fourth in a series of papers focused on implementing, calibrating, and validating criteria for simulating microstructurally small fatigue crack (MSFC) evolution, with high strain conditions in aluminum alloy (AA)7075-T651 as the proof-test application. MSFC evolution is divided into three stages: incubation, nucleation, and propagation. The specific focus of this paper is on the last stage, MSFC propagation, which is microstructure-governed fatigue crack growth through grains and/or along grain boundaries. Three simulated field metrics, crack tip displacement, crack-induced plastic slip localization, and maximum tangential stress ahead of the crack, previously investigated for prediction of nucleation, are investigated in this paper to determine their dependence on microstructural heterogeneities after nucleation. A total of 21 simulations are performed on a simplified baseline model of an AA7075-T651 microstructural region containing an MSFC. All three metrics are determined to be significantly

dependent on the local microstructure immediately subsequent to nucleation. The particle spawning the crack and the orientation(s) of the grain(s) immediately surrounding the nucleated MSFC most influence the MSFC metrics.

The paper in the second chapter focuses on the implementation of a computational framework that accurately and probabilistically models fatigue crack propagation at the microstructural scale, once again with high strain conditions in AA7075-T651 as the proof-test application. Toolsets are presented that generate and discretize statistically accurate microstructure geometry models and explicitly simulate the evolution of microstructurally small fatigue cracks. The concept is demonstrated through two model simulations and feasibility of the approach is critically evaluated.

The paper in the third chapter is the fifth in the same series of papers described above for the first chapter. The focus of this paper is again on the last MSFC evolution stage, MSFC propagation. High resolution, micro-scale images of three propagating MSFC's are analyzed to determine dependencies of MSFC propagation on microstructural heterogeneities. Additionally, the three MSFC metrics studied in the first chapter - maximum tangential stresses, plastic slip localization, and crack displacements local to the crack front - are simulated in a finite element model that replicates an observed MSFC and the surrounding microstructure. The detailed observations and simulation reveal that MSFC propagation in AA7075-T651 is highly dependent on the local microstructure, and MSFC behavior due to these dependencies can be predicted by the computed field metrics.

BIOGRAPHICAL SKETCH

Mike was born in Waterville, Maine on February 11, 1981. He graduated from Messalonskee High School in Oakland, Maine in June 1999. From there, he enrolled in undergraduate studies at Worcester Polytechnic Institute (WPI) in Worcester, Massachusetts, where he earned a Bachelor of Science degree in Civil and Environmental Engineering in May 2003. Following his studies at WPI, he enrolled in graduate study at Cornell University, where he earned a Master of Science degree in Civil and Environmental Engineering and he continued to pursue his Doctor of Philosophy degree in Structural Engineering. His Ph.D. research, presented in this thesis, was focused in Computational Fracture Mechanics and advised by Professor Anthony Ingraffea, with Professor Alan Zehnder and Professor Christopher Earls as minor advisors.

In loving memory of my dad,

and to my wife Andrea.

The architect and the constructor often never meet,

but without either the engineer has no structure.

ACKNOWLEDGEMENTS

I owe many thanks to my research advisors and Cornell Fracture Group colleagues. Professor Ingraffea, thanks for being an outstanding teacher of both professional and life lessons, whether it be in the office, on the golf course, or places inbetween. Professor Earls and Professor Zehnder, thanks for helping me through my M.S. and Ph.D., and for providing much needed guidance as I searched for the best occupation to suit my professional niche. Bruce, Gerd, and Wash, it would have been difficult, if not impossible, for me to finish this thesis without your combined computational expertise and willingness to help others. Jake and Jeff, I will forever remember the trials, tribulations, and laughs we shared as we tempted numerical fate by combining cracks with crystal plasticity. John, thanks for getting me to the office as fast as possible for three years and for giving helpful insight whenever I was lost in the mechanics, code, and important decisions.

I would also like to thank the United States Department of Energy for providing funding through the Computational Science Graduate Fellowship Program of the Office of Science and National Nuclear Security Administration under contract DE-FG02-97ER25308, and for awarding computational resources at the National Energy Research Scientific Computing Center under contract DE-AC02-05CH11231. I would also like to thank the United States Defense Advanced Research Projects Agency and Northrop Grumman Corporation, for being the sponsors and principal investigators, respectively, of my research as part of the Structural Integrity Prognosis System (SIPS) project under contract HR0011-04-C-0003.

Most importantly, I owe endless thanks to my family. Mom, you taught me to persevere, to always hold my head high, and so much more! Andrea, my wife and best friend, I am so lucky we found each other, I truly do not think I would have made it to my Ph.D., and to the many places we will go beyond, without

you. Chat, thanks for being such an amazing sister and role model, and for always being there for mom and me.

TABLE OF CONTENTS

Biographical Sketch . . . iii
Dedication . . . iv
Acknowledgements . . . v
Table of Contents . . . vii
List of Tables . . . ix
List of Figures . . . x

1 A geometric approach to modeling microstructurally small fatigue crack formation: IV. Simulation of material heterogeneity and crack size influence on propagation mechanisms 1
1.1 Introduction . . . 2
1.1.1 Background . . . 3
1.1.2 Baseline model . . . 12
1.1.3 Baseline simulation methodology . . . 20
1.2 Mesh convergence . . . 20
1.2.1 Qualitative evaluation . . . 21
1.2.2 Quantitative evaluation . . . 23
1.3 Parametric studies . . . 26
1.3.1 Particle influence domain . . . 27
1.3.2 Transgranular domain . . . 31
1.3.3 Orientation influence on an intragranularly nucleated crack . . . 33
1.3.3.1 Crack size a_1 . . . 33
1.3.3.2 Crack size a_2 . . . 36
1.3.3.3 Crack size a_3 . . . 37
1.3.4 Misorientation influence on a transgranularly nucleated crack 39
1.3.5 Summary of all simulation results . . . 41
1.4 Conclusions and future work . . . 45

2 Geometrically explicit, three-dimensional finite element modeling of statistically realistic microstructures with fatigue cracks 49
2.1 Introduction . . . 50
2.1.1 Background . . . 53
2.1.1.1 Geometry model generation . . . 54
2.1.1.2 Finite element meshing . . . 62
2.1.1.3 Microstructurally small fatigue crack simulation . . . 64
2.1.2 Observations of proof-test application . . . 66
2.1.3 Modeling framework . . . 69
2.2 Finite element model generation and adaptation . . . 70
2.2.1 First-phase statistics* . . . 72
2.2.2 Second-phase statistics* . . . 76
2.2.3 First-phase statistical realization model* . . . 78
2.2.4 First-phase surface mesh* . . . 82

2.2.5 First-phase volume mesh . . . 86
2.2.6 Second-phase statistical realization model . . . 88
2.2.7 Second-phase surface mesh . . . 91
2.2.8 Microstructure geometry and mesh adaptation for particle and fatigue crack representation . . . 94
2.2.9 Material state mapping . . . 98
2.3 Criteria for microstructurally small fatigue crack stages . . . 100
2.3.1 Incubation . . . 100
2.3.2 Nucleation . . . 101
2.3.3 MSFC propagation . . . 104
2.4 Proof-of-concept simulations . . . 106
2.4.1 Stress fields prior to incubation . . . 107
2.4.2 Field metrics in the neighborhood of an incubated crack . . . 109
2.5 Summary, feasibility, and limitations of approach . . . 112

3 A geometric approach to modeling microstructurally small fatigue crack formation: V. Observation and simulation of propagation dependence on microstructural heterogeneity 115
3.1 Introduction . . . 116
3.1.1 Background . . . 117
3.1.2 Methodology of MSFC observation and replicated microstructure simulation . . . 123
3.2 Observations of propagation subsequent to nucleation . . . 124
3.2.1 Propagation direction characteristics . . . 125
3.2.2 Propagation rate characteristics . . . 132
3.3 Replicated-microstructure simulation of an MSFC immediately following nucleation . . . 141
3.3.1 Maximum tangential stress magnitude and direction . . . 144
3.3.2 Magnitude and cyclic change of irreversible slip . . . 145
3.3.3 Cyclic change in crack tip displacement . . . 147
3.4 Summary and future work . . . 150

A Crystal plasticity constitutive model 154

Bibliography 157

LIST OF TABLES

1.1 Three face-centered cubic (FCC) grain orientations investigated in the baseline model. 16
1.2 Schmid factors for the FCC grain orientations in Table 1.1 and loading along RD. 16
1.3 All permutations of crack sizes and region properties simulated for the baseline model shown in Figure 1.4. Region properties are identified as 'elastic' for linear elastic, isotropic or one of the three texture orientation identifiers from Table 1.1 for crystal plastic. . . 19
1.4 Averages of MSFC metrics calculated along the crack front for all baseline models listed in Table 1.3. Horizontal lines between datasets divide the three crack sizes: a_1 is at the top, a_2 is in the middle, and a_3 is on the bottom. *Italics texts* are models that have the rotated orientation for grain A and/or grain B. **Bold texts** are models that do not have a particle. ΔCTD, $\Delta CTOD$, and $\Delta CTSD$ are in μm, θ is in degrees, and $\sigma_{\theta\theta}^{max}$ is in MPa. 43

2.1 Grain size and shape distribution parameters for the distributions shown in Figure 2.4, derived from data in [76]. 75
2.2 Particle size and shape distribution parameters, derived from data in [29]. 78
2.3 Maximum particle stresses computed by the response surface from Bozek *et al.* [7] and by simulation of the microstructure finite element model (μstructure FEM) of three uncracked particles shown in Figure 2.20. 108

3.1 Recorded propagation rates of 4 previously nucleated microstructurally small fatigue cracks. Rates are determined from high resolution microscopic images taken at 30, 100, 300, 1000, and 3000 load cycles. Observation data interpreted for this table were provided by Northrop Grumman Corporation. 139
3.2 Computed field metrics for the MSFC length observed at the 1000^{th} load cycle in P124, and the observed propagation rates of the two observed crack tips between the 1000^{th} and 3000^{th} load cycles. . . . 149

A.1 Crystal plasticity parameters for AA7075-T651, from [7]. 155

LIST OF FIGURES

1.1 Observations of fatigue crack propagation from a particle 7
1.2 Nomenclature of crack tip displacement vectors 9
1.3 Nomenclature and loading conditions for proof-test application . . 9
1.4 Baseline model geometry 15
1.5 Coarse and fine meshes for mesh convergence study 21
1.6 Deformed shape and contours of RD-displacement for two mesh densities 22
1.7 Contours of σ_{xx} for two mesh densities 23
1.8 Contours of D_1 for two mesh densities 23
1.9 Delineation of crack data measurement locations 24
1.10 Mesh convergence plots of crack displacement profile 25
1.11 Mesh convergence plots of CTD, $\sigma_{\theta\theta}^{max}$, and D_3^{avg} along crack front 26
1.12 Line plots of particle influence on microstructural fatigue metrics . 29
1.13 Contour plots of particle influence on slip-based metric 30
1.14 Contour plots of particle influence on first principal stress 30
1.15 Contour plots of transgranular influence on slip-based metric . . . 32
1.16 Contour plots of transgranular influence on first principal stress . . 32
1.17 Line plots of grain orientation influence on microstructural fatigue metrics of a nucleated crack 35
1.18 Contour plots of grain orientation influence on slip-based metric . . 36
1.19 Contour plots of grain orientation influence on first principal stress 37
1.20 Line plots of grain orientation influence on microstructural fatigue metrics of an intragranular crack 38
1.21 Line plots of grain orientation influence on microstructural fatigue metrics of a transgranular crack 40
1.22 Line plots of grain boundary misorientation influence on microstructural fatigue metrics of a nucleated crack 42

2.1 Experimental observations of microstructurally small fatigue crack propagation 52
2.2 Material axes and loading conditions for proof-test application . . . 68
2.3 Three main steps of the realization modeling framework 71
2.4 Grain size and shape histograms and distributions of AA7075-T651 74
2.5 Grain texture data of AA7075-T651 from electron backscatter diffraction 76
2.6 Grain texture data from X-ray of AA7075-T651 76
2.7 Representative volume element of first-phase microstructure 80
2.8 Comparison of grain size and shape distributions from RVE's and observations 81
2.9 Cropped statistical realization geometry models from a larger RVE 82
2.10 Triangular surface meshes of a first-phase realization model 86

2.11 Element quality histogram of a volume-meshed first-phase realization model . . . 88
2.12 A 10,000 Al_7Cu_2Fe particle realization . . . 91
2.13 2D illustration of particle geometry generation procedure . . . 93
2.14 Triangular surface mesh of a typical surface particle geometry . . . 93
2.15 Subvolume routines for local finite element model adaptation . . . 97
2.16 Process of crack trimming along a material interface . . . 98
2.17 Delineation of crack data measurement locations . . . 103
2.18 Illustration of nucleation dependence on slip and stress . . . 104
2.19 Contour plots of grain orientation influence on first principal stress ahead of a nucleated fatigue crack . . . 106
2.20 Simulated stresses in a microstructure model before incubation . . . 108
2.21 Simulated fields in a microstructure model with 3 incubated cracks 110
2.22 Line plots of field metrics near 3 incubated cracks . . . 111

3.1 Scanning electron micrograph of MSFC observation region P87 . . . 126
3.2 Scanning electron micrograph of MSFC observation region P22 . . . 126
3.3 Scanning electron micrograph of MSFC observation region P50 . . . 126
3.4 Scanning electron micrograph of MSFC observation region P187 . . . 127
3.5 Scanning electron micrograph of MSFC observation region P208 . . . 127
3.6 Scanning electron micrograph of MSFC observation region P124 . . . 128
3.7 Scanning electron micrograph of MSFC observation region P91 . . . 128
3.8 Highest Schmid factor plot of the texture in MSFC observation region P187 . . . 131
3.9 Second highest Schmid factor plot of the texture in MSFC observation region P187 . . . 132
3.10 Highest Schmid factor plot of the texture in MSFC observation region P91 . . . 133
3.11 Second highest Schmid factor plot of the texture in MSFC observation region P91 . . . 134
3.12 Highest Schmid factor plot of the texture in MSFC observation region P208 . . . 135
3.13 Second highest Schmid factor plot of the texture in MSFC observation region P208 . . . 136
3.14 Highest Schmid factor plot of the texture in MSFC observation region P124 . . . 137
3.15 Second highest Schmid factor plot of the texture in MSFC observation region P124 . . . 138
3.16 Replication model of the experimentally observed crack propagating in observation region P124 . . . 143
3.17 Inverse pole figure showing the texture surrounding the MSFC in observation region P124 . . . 143
3.18 Maximum principal stress contours at the second load peak for the nucleated crack in observation region P124 . . . 146

3.19 Irreversible slip contours at the second load peak for the nucleated crack in observation region P124 148

CHAPTER 1

A GEOMETRIC APPROACH TO MODELING MICROSTRUCTURALLY SMALL FATIGUE CRACK FORMATION: IV. SIMULATION OF MATERIAL HETEROGENEITY AND CRACK SIZE INFLUENCE ON PROPAGATION MECHANISMS

This series of papers is motivated by the need for high fidelity fatigue life predictions of aging aerospace structures where much of the life is spent in the microstructurally small fatigue crack (MSFC) propagation phase. The overarching goal of the research presented in this series is to implement and validate a geometrically explicit, mechanistic approach to modeling microstructurally small fatigue crack evolution, where the proof-test material is aluminum alloy (AA)7075-T651. This paper focuses on field metrics that gauge the mechanisms governing a MSFC immediately following matrix crack nucleation, where nucleation in this material is extension of a through-particle crack into the surrounding grain(s). A mesh convergence study is performed to determine the appropriate mesh size for convergence of three non-locally calculated MSFC metrics: crack tip displacement, maximum tangential stress, and plastic slip accumulation. A ratio of crack front element size to crack size of 0.01 is deemed necessary for convergence. Subsequently, meshes with this ratio are used in a baseline model to perform scoping studies on the influences of various microstructural heterogeneities on the MSFC metrics. Three crack sizes are investigated: a crack nucleated a short distance into the grain(s) containing the particle, a crack extended half-way through the grain(s) containing the particle, and a crack approaching the grain boundaries between the grain(s) containing the particle and their neighboring grains. The influences of the particle containing the crack, and grain orientations and misorientations in the neighbor-

hood of the crack are calculated and compared. It is found that the particle and grain orientation most significantly influence metrics, but particle influences decay completely as the crack propagates through the first grain after nucleation. Orientations with one or no high Schmid factors have higher maximum tangential stress and crack tip displacement than orientations with two high Schmid factors, but the orientations with two high Schmid factors have the highest cyclic plastic slip accumulation.

1.1 Introduction

Studies by Bozek *et al.* [7] and Hochhalter *et al.* [31] give detailed motivations for, and descriptions of, the geometric modeling approach being developed in this series of papers. In this series, the incubation, nucleation, and MSFC propagation stages are being individually investigated and modeled through high resolution observation and detailed finite element modeling of the microstructure. The proof-test application is high strain fatigue in AA7075-T651. For this application, incubation is the through-cracking of Al_7Cu_2Fe particles, nucleation is the extension of a previously incubated crack across the particle-grain interface, and MSFC propagation is all microstructurally-governed crack propagation after nucleation. When the microstructure no longer governs, the crack is in the microstructurally large fatigue crack (MLFC) propagation phase. In the first paper of this series, Bozek *et al.* [7] addressed the incubation stage by developing a highly efficient, fracture mechanics-based procedure for predicting particle cracking. This procedure accounts for particle cracking dependence on particle aspect ratio, size, location, strain level, and surrounding grain orientation. In the second paper of this series, Hochhalter *et al.* [31] developed a non-local approach to calculating irreversible plastic slip metrics ahead of an incubated crack and elucidated, through baseline

model simulations and two experimental replication simulations, a relationship between accumulated slip and the occurrence of nucleation. In the third paper in this series, through additional experimental replication simulations, Hochhalter *et al.* [32] revealed a distinct power-law relationship between the accumulation of irreversible slip and the maximum tangential stress immediately ahead of an incubated crack at the load cycle of nucleation occurrence. The nucleation direction was found to be approximately normal to maximum tangential stress. Additionally, a direct relationship was shown between crack displacement magnitude of an incubated crack and the number of cycles to nucleation, which is consistent with previous findings that MSFC growth rate is dependent on the amount of crack blunting [49].

This paper complements the prior papers of this series by investigating simulated field metrics that gauge mechanisms governing MSFC propagation, the final stage of the MSFC phase. The three metrics studied for nucleation - accumulated slip, maximum tangential stress, and crack displacement - are critically evaluated for prediction of MSFC propagation rate and direction. Simulations are performed on polycrystalline baseline models to better understand the dependence of these metrics on various microstructural heterogeneities. First, however, related previous studies are reviewed to motivate further the MSFC simulation approach, and to reveal the objectives of this study and how they facilitate novel contributions to the fatigue community.

1.1.1 Background

All three MSFC stages have been studied for many years. In general, a thorough understanding of the MSFC stages is important to the fatigue community because

it is well known that:

- A majority of the fatigue life is often consumed by the MSFC phase [10,17,77];
- MSFC propagation rates are under-estimated by the Paris model that pertains to larger crack lengths [57, 77];
- Crack growth increments and cyclic crack front plastic zone sizes are typically at the length scale of the microstructure, or smaller [40, 66, 67]; and,
- MSFC propagation rates fluctuate greatly, likely due to the individual influences of microstructural heterogeneities [40, 67].

This paper is not directly focused on relating microstructural features to crack growth rate; instead, the focus is on relating microstructural features to metrics of the mechanisms governing MSFC growth rate. In a subsequent paper in this series, a crack growth rate model based on these metrics will be calibrated through finite element simulation of replicated experimental observation. The first two MSFC stages are also not the focus in this background study, because previous papers in this series have provided background studies of, and novel contributions to, incubation and nucleation [7, 31, 32]. The MSFC propagation stage is of primary focus here and the first two stages are only mentioned in references to the latter stage.

In 1967, Laird [39] reviewed many of the MSFC propagation characteristics observed and hypothesized in the state of the practice at that time. The focus was on the crack blunting behaviour of a microstructurally small crack under cyclic loading and the influence that microstructure has on blunting. Crack blunting, the one mechanism theorized by Laird to govern MSFC propagation, is subdivided into two stages: Stage I and Stage II, as originally defined by Forsyth [20]. Stage I is

primarily a crack sliding mode caused by plastic slip along one system aligned with the propagation direction. In contrast, Stage II is primarily a crack opening mode caused by large plastic slip accumulations on two or more systems generally not aligned with the propagation direction. When nucleation occurs along a single slip band, Stage I precedes Stage II and transition to the latter is caused by an increase in the crack driving forces with crack size, which consequently activates plastic slip on more than one system. Laird further states that microstructural heterogeneities do not change the crack propagation mechanism. However, heterogeneities can change the magnitudes and directions of plasticity, and thusly influence the rate of crack blunting and Stage I/II transitions.

Subsequent studies augmented and modified understanding of the characteristics presented by Laird. Koss and Chan [36] theorized that a Stage I crack in a homogeneous single crystal continually propagates in Stage I since crack resistance is weakest along the slip plane of propagation and the increase in crack driving force normal to the slip plane further increases the irreversible work done on that plane, in a manner similar to the formulation later given by Fatemi and Socie [18]. However, microstructural heterogeneities present in polycrystals and crack morphology can significantly influence MSFC propagation. Zhai *et al.* [89] analytically and experimentally illustrate how grain boundaries can act to cause deflection, rate change, arrest, and/or branching of a Stage I MSFC. It is also theorized that grain boundaries can force Stage I to Stage II transition, because an initially Stage I crack will eventually encounter a grain where Stage I is less favorable than Stage II due to misalignment between the slip system directions and the maximum shear stress directions [37, 43, 49]. McClintock [49] suggests Stage II is a statistical average of many small Stage I facets growing on multiple active slip planes, and between Stage I and Stage II there can be an alternating Stage I phase where the

crack extends along one slip direction in loading and along another slip direction in unloading. The average behaviour of a Stage II crack is propagation approximately normal to the local maximum tensile stress direction, *i.e.* the direction of maximum tangential stress ahead of the crack. Consequently, a misperception is that Stage II propagation is synonymous with Mode I microstructurally large fatigue crack (MLFC) propagation, where MLFC is a crack at a length scale large enough that microstructure negligibly influences propagation. However, this is not always true since microstructural heterogeneities can substantially reorient the maximum tangential stress direction for sufficiently small Stage II cracks, and favorably oriented sub-grain boundaries can introduce local weaknesses along which a MSFC will propagate within grains [58]. One objective of this paper is to present simulation results that further clarify the difference between a Stage II MSFC and a Mode I MLFC.

Further complicating the overall material behaviour but likely eliminating one of the two MSFC propagation stages in AA7075-T651 is the presence of brittle second-phase particles. Specifically, the combined incubation and nucleation mechanisms occurring at these particles enforce apparent Stage II MSFC propagation immediately following nucleation. Observations of fatigue crack incubation in AA7075-T651 show the incubation mechanism, Al_7Cu_2Fe particle cracking, occurs in a direction approximately normal to the far-field loading axis [59, 86]. Furthermore, subsequent nucleation from these incubated cracks closely aligns normal to maximum tangential stress rather than along a direction of shear strain localization or on a single slip system [32]. Based on these prior results and additional experimental observations that propagation after nucleation remains self-similar through the first grain, *e.g.* Figure 1.1, it is assumed that MSFC propagation is Stage II immediately following nucleation in AA7075-T651. The validity of this

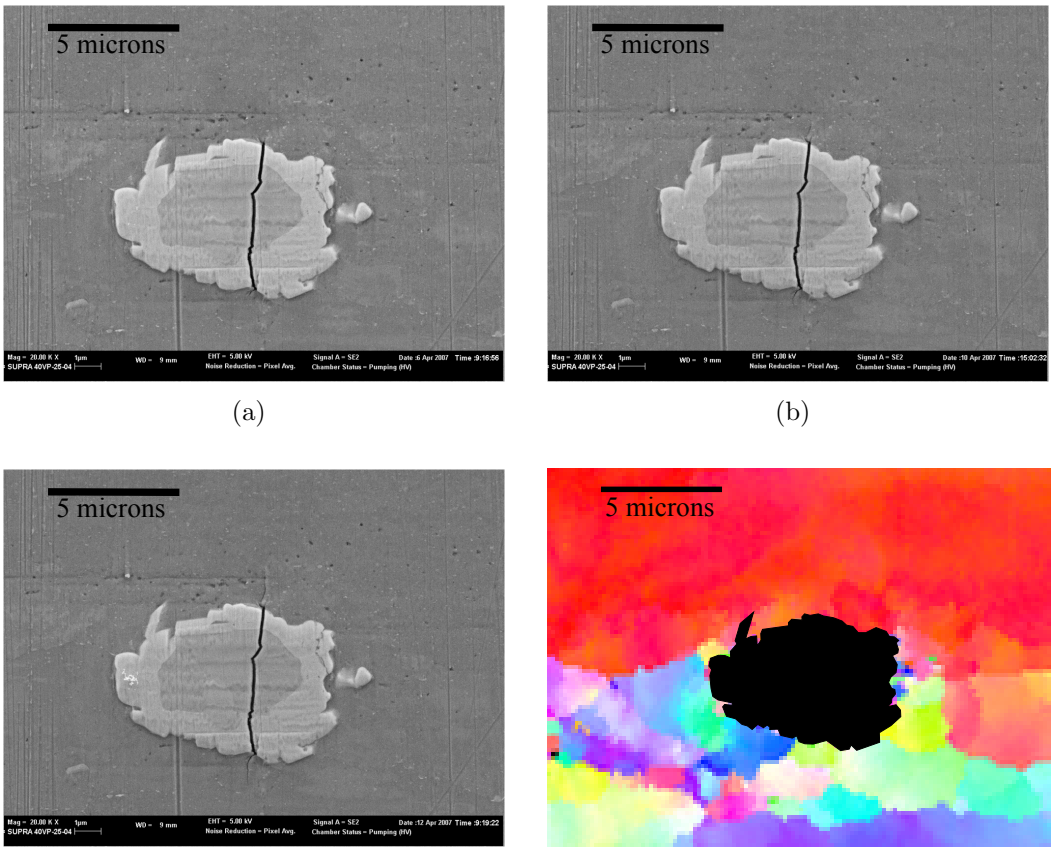

(a) (b)

(c) (d)

Figure 1.1: Scanning electron micrographs of MSFC nucleation and propagation from a particle after (a) 100, (b) 300, and (c) 1000 load cycles, and (d) inverse pole figure showing textures of grains near the particle. Loading direction, RD, is horizontal and ND is vertical. Images courtesy of Northrop Grumman Corporation.

assumption is determined in the next paper of this series.

Since crack blunting is the commonly theorized mechanism governing MSFC propagation, the relationship between blunting and MSFC propagation has been frequently studied in the fatigue literature, and is being studied herein, since a complete understanding has yet to be achieved. Blunting is typically measured as cyclic change in crack displacement near the crack tip, *i.e.* a discrete point along the crack front. The measurement for displacement, sliding, opening, or some com-

bination thereof, varies among researchers. Figure 1.2 is an illustration of the crack tip displacement vector nomenclature used in this series of papers. The orthogonal basis in this figure is composed of the material axes for rolled microstructure, Figure 1.3: RD is the rolling direction, TD is the transverse direction, and ND is the normal direction. The vector formulas of crack tip displacements are given in Equation 1.1 and Equation 1.2.

$$\overline{CTSD} = \overline{CTSD_I} + \overline{CTSD_{II}} \tag{1.1}$$

$$\overline{CTD} = \overline{CTOD} + \overline{CTSD_I} + \overline{CTSD_{II}} \tag{1.2}$$

$\overline{CTOD}$, $\overline{CTSD_I}$, and $\overline{CTSD_{II}}$ are the RD, ND, and TD components, respectively, for a crack in the TD-ND plane, which is the common crack plane for the proof-test application studied here. The corresponding vector magnitudes are symbolized by $CTOD$, $CTSD_I$, $CTSD_{II}$, $CTSD$, and CTD. $CTOD$ is the crack tip opening displacement, $CTSD$ is the crack tip sliding displacement, and CTD is the crack tip displacement. Crack displacement is differentiated from the cyclic amplitude of crack displacement by including 'Δ' in symbols for the latter, *e.g.* $\Delta\overline{CTD}$ and ΔCTD. ΔCTD is primarily investigated in this paper since this is a measure of the total change in crack blunting during one load cycle.

One area of modeling research is focused on developing empirical, semi-empirical, and phenomenological formulae that implicitly incorporate crack blunting in predictions of MSFC growth rates. In the early 1980's, a group of researchers, including Ritchie and Suresh [67] and Lankford *et al.* [40], studied whether the common ΔK_{eff} term of elastic-plastic fracture mechanics could be modified by incorporating observed microstructural heterogeneity influence on crack closure through local variations in plasticity, surface roughness, and corrosion. However, after extensively comparing crack growth behavior of small and long cracks in

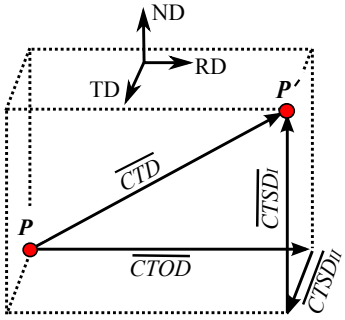

Figure 1.2: Nomenclature of crack tip displacement vectors. Points P and P' are on or near the crack front and overlapping prior to deformation. $\overline{CTD}$ is the vector addition of $\overline{CTOD}$, $\overline{CTSD_I}$, and $\overline{CTSD_{II}}$, the RD, TD, and ND components, respectively, for a crack in the TD-ND plane. This is an adaptation of a figure from [32].

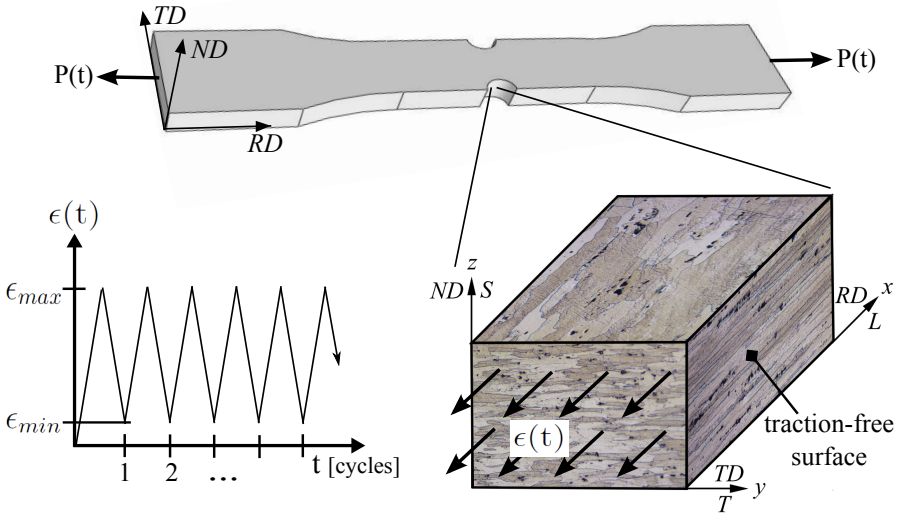

Figure 1.3: Illustration of a double edge-notched specimen from [59] with a magnified view of the notch-root region simulated at the microstructural length scale. The magnified region is shown with scanning electron microscopy images and nomenclature of the orthogonal planes and axes in AA7075-T651 microstructure, from [11]. Etching was performed to delineate grain boundaries. The simulated constant amplitude cyclic loading conditions, representative of the notch root strain, are also illustrated.

AA7075-T651, Lankford *et al.* concluded ΔK_{eff} was likely not the driving force of small fatigue cracks; instead, crack growth rate was more directly correlated to crack opening. Consequently, subsequent studies utilized the continual improvements in microscale observation methods to observe and understand better the relationship between CTD and MSFC growth rates. As a result, modelers have recently employed such relationships in semi-empirical or phenomenological MSFC propagation formulae [51,88]. McDowell *et al.* [51] delineate incubation, nucleation, and MSFC propagation as two stages, incubation and microstructurally small crack propagation, where their 'incubation' term includes incubation, nucleation, and part of MSFC propagation, as defined here. Specifically, McDowell *et al.* define incubation as the fatigue processes leading up to a crack that extends through the small-scale plasticity region created by the particle where cracking begins. Consequently, this definition does not apply for large-scale yielding within the microstructure. Within the limitations of this model, McDowell *et al.* propose a Coffin-Manson relationship to compute the number of cycles to extend an MSFC beyond the micro-notch influence region of the particle. Subsequently, a linear relationship between crack growth rate and ΔCTD is used in the MSFC propagation stage, where ΔCTD is semi-empirically computed. Xue *et al.* [88] proposed revisions of this MSFC growth rate formula to include parameters for grain orientation and grain size effects, but neither were included in calibrating the formula to model MSFC growth in AA7075-T651 due to a lack of knowledge of MSFC propagation dependence on these microstructural heterogeneities. Thus, an objective of the studies in this paper is to quantify CTD dependence on microstructural heterogeneities such that these findings can be incorporated into semi-empirical, phenomenological, and/or statistical models.

Another area of modeling research is focused on explicitly determining crack blunting dependence on microstructural heterogeneities and incorporating this in MSFC propagation predictions. Likely due to simplicity and computational ease, more explicit MSFC propagation simulations have been performed in two dimensions than three dimensions. Li [42] developed a two-dimensional analytical formula for CTD with respect to grain orientation by applying the predominantly Stage I crack assumptions of Koss and Chan [36]. Rice *et al.* [65] developed a two-dimensional finite element constitutive model for crystal plasticity with which planar double-slip was simulated ahead of a Stage II crack for two grain orientations. The deformed shapes show the crack opening to crack sliding ratio to be significantly larger for one orientation than the other. Bennett and McDowell [3] also applied a planar double slip finite element constitutive model to study $CTOD$ and $CTSD$ at strains below far-field yielding (the studies herein are for far-field yielding of the microstructure) for material properties representative of a high strength alloy. Bennett and McDowell found that $CTOD$ is more dependent on local orientation discontinuity than $CTSD$, and $CTOD$ is always dominant under tensile loading conditions. Wang *et al.* [84] employed a three-dimensional, rate dependent crystal plasticity finite element formulation to study parametrically microstructure heterogeneity influence on a MSFC spanning approximately two grains in AA7075-T651. Two model geometries were studied: in one, the crack was propagating toward a grain boundary, and in the other, the crack was propagating toward a second-phase particle. The grain boundary study is similar to a study performed here, but in the study by Wang *et al.* , the crack length is twice as large, and the maximum load is one-tenth what is studied herein. For this larger crack size and lower load, Wang *et al.* showed that orientation of the grain containing the crack more significantly influences the minimum stress required to

open the crack than the grain boundary misorientation; heterogeneity influences on CTD were not investigated. Although there are significant differences between all of these prior studies and the present study, another objective in this paper is to compare and contrast results with prior findings and determine other relationships among microstructural heterogeneities, fields near the crack front, and CTD. In the process of achieving this and the other objectives, an overarching goal is to illustrate why MSFC propagation characteristics need to be incorporated in high fidelity fatigue life predictions.

In summary, four main objectives in this paper are to:

1. Elucidate the differences between a Stage II MSFC and a MLFC;
2. Determine physical relationships among microstructural heterogeneities, near crack stress fields, plastic strain localizations, and CTD of an MSFC;
3. Quantify CTD dependence on microstructural heterogeneities to incorporate in semi-empirical, phenomenological, and/or statistical models; and,
4. Illustrate why MSFC propagation needs to be incorporated in high fidelity fatigue life predictions.

The vehicle for achieving these objectives is the following baseline model.

1.1.2 Baseline model

A simplified baseline model is created to represent what has been observed in two fatigue experiments on AA7075-T651 double edge-notched (DEN) specimens [59]. In these experiments, observations of MSFC incubation, nucleation, and

propagation were made in a 1.50 mm x 0.50 mm region within one of the two notch roots [32]. The loading condition in the notch root is approximately R=0.1 (min/max strain ratio) with 1% maximum strain in the RD. Figure 1.3 illustrates the DEN notch root, the three-dimensional microstructure, and the notch root loading conditions simulated here and in previous studies [7,31,32]. The simulated boundary conditions in this study are the same as those detailed by Bozek *et al.* [7]: constrained, axial tension with R and maximum strain as given above.

The DEN experiments revealed MSFC nucleation occurs within $O(10^1)$ to $O(10^3)$ load cycles, and subsequent MSFC propagation through the first grain requires another $O(10^2)$ to $O(10^3)$, or more, load cycles. The upper bound on the number of cycles to propagate a nucleated MSFC through the first grain could not be determined, because the DEN specimens failed prior to this occurring for some of the observed cracks. Figure 1.1 is a set of microstructural images from one of the observed MSFC's that propagated the fastest. A comparison of the inverse pole figure, Figure 1.1(d), to the scanning electron micrographs, Figure 1.1(a) through Figure 1.1(c), shows the crack nucleated between 100 and 300 cycles, and propagated through the first grain by approximately 1000 cycles.

Due to the computational intractability of modeling all load cycles through incubation, nucleation, and early MSFC propagation, this baseline study simulates an MSFC as stationary during two cycles of loading. From the mesh convergence study presented in Section 1.2, it was determined that the mesh size required for convergence of near crack front fields consumes approximately 10 thousand CPU hours of run-time per load cycle. This is computationally tractable to thousands of load cycles for one model simulation, assuming access to a large computational cluster with approximately 10 million CPU hours of available run-time, but repe-

tition of this task for multiple model simulations is currently intractable. Since the cracks are instead modeled as stationary, the plastic wake of a propagating MSFC is not captured. This wake is likely to reduce CTD at any load and can theoretically cause crack closure at low applied tensile loads. However, for the loading considered here, it is assumed (observations of closure were not made) the crack does not close at minimum load. Therefore, ΔCTD computed for a stationary MSFC model should be a sufficient approximation of a propagating MSFC. Since MSFC propagation is not simulated here, the actual stress and plastic slip states near the cracks are not accurately produced. However, the intent of this study - to compare results from a parametric study and begin to understand the relative influence of variations among microstructural heterogeneities on MSFC propagation metrics - can be satisfied by modeling a stationary crack.

The baseline model geometry, Figure 1.4, represents four grains of typical ND dimension for AA7075-T651 and a surface particle likely to crack under the aforementioned loads. The ND grain dimension, L_g^{ND}, is 20 μm because this is a typical dimension observed in AA7075-T651 microstructure [76]. Observed RD and TD grain dimensions are not used or necessary in the baseline model, because the largest MSFC size modeled is much smaller than either dimension. RD and TD dimensions of L_g^{RD}=60 μm and L_g^{TD}=40 μm, respectively, are used to eliminate boundary effects on the crack. The particle radii in the ND and TD, L_p^{ND} and L_p^{TD}, respectively, are both 2 μm, because these are common radii in both dimensions for Al_7Cu_2Fe particles in this material, based on statistical data recorded by Harlow *et al.* [29]. The RD particle radius, L_p^{RD}, is 6 μm, because this is also a common radius and the resulting particle size and aspect ratios frequently cause particle cracking, as predicted by the incubation filter from Bozek *et al.* [7]. More importantly, this particle is predicted to crack for all of the following grain

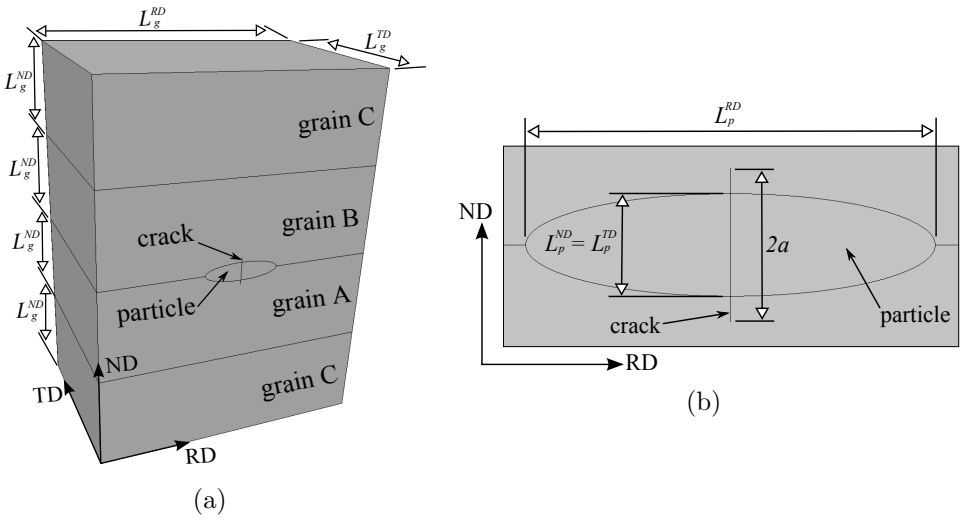

Figure 1.4: Baseline model geometry. (a) Perspective view of entire model with grain identifier and dimension labels. (b) Magnified view of particle and crack with particle and crack dimension labels.

orientations modeled here. The particle-grain interface and all grain boundaries are simulated as perfectly bonded, because no debonding was observed at these material interfaces during experiments.

Three grain orientations are modeled with the crystal plasticity formulation from Matous and Maniatty [48] and the AA7075-T651 constitutive parameters given by Bozek *et al.* [7] and in Appendix A. Each texture, Table 1.1, is common in AA7075-T651, and together they represent three different plastic slip characteristics, revealed by the Schmid factors of their 12 primary slip systems, Table 1.2. The three orientations are referred here as the 'weak', 'rotated', and 'strong' orientations. The weak orientation has one slip system with Schmid factor close to 0.50, which will result in early onset of plastic slip in comparison to an orientation with no high Schmid factors. The rotated orientation can also be categorized as weak since it actually has two high Schmid factors, but the delineation refers to the rotated (or twisted) cube texture family to which this orientation belongs [58, 76].

Table 1.1: Three face-centered cubic (FCC) grain orientations investigated in the baseline model.

	Bunge Euler angles [rads]		
orientation ID	ϕ_1	Φ	ϕ_2
weak	3.988913	0.730795	2.806933
rotated	3.803586	-0.661472	2.590874
strong	4.390221	0.721284	1.114852

Table 1.2: Schmid factors for the FCC grain orientations in Table 1.1 and loading along RD.

	12 slip systems											
	1	2	3	4	5	6	7	8	9	10	11	12
weak	0.00	0.00	0.00	0.20	0.33	0.13	0.33	0.20	0.13	0.46	0.13	0.33
rotated	0.49	0.29	0.20	0.29	0.21	0.08	0.29	0.20	0.49	0.21	0.29	0.08
strong	0.02	0.22	0.24	0.03	0.24	0.26	0.33	0.01	0.32	0.07	0.09	0.02

The strong orientation has no high Schmid factors and a higher yield strain than the other two orientations. Three unique types of plasticity are expected to occur in the weak, rotated, and strong orienations, respectively: early yielding with initial slip localization in one direction, early yielding with initial slip localization in two directions, and late yielding with slip localization in three or more directions. The reader must be aware that the word choices of 'weak' and 'strong' are referring to the relative yield strengths, and *not* the fracture toughnesses, of these orientations.

Three crack lengths, *i.e.* radii, a, of a semi-circular surface crack, are also modeled to simulate three sizes of an MSFC inside the first grain(s) encountered after nucleation. The first crack length is a=a_1=3μm to simulate an MSFC immediately subsequent to nucleation, when the crack is likely still within the micro-notch root influence of the particle, *i.e.* the region of elevated stresses due to the high stiffness of the particle relative to the grain stiffness. The second crack length is a=a_2=11μm to simulate an intragranular MSFC that is equi-distant from both the particle-grain interface and the next grain boundary. The third crack length is a=a_3=19μm to simulate a transgranular MSFC as it is 1μm from reaching grain C on the RD-ND surface shown in Figure 1.4(a). The crystal plasticity model employed in this study has no inherent length scale, but the crack varying in size and location with respect to the fixed sizes and locations of microstructural features will influence the computed fields among modeled crack sizes.

Table 1.3 is a summary of all orientations and crack lengths studied for the baseline model in Figure 1.4. For each orientation and at each crack length, a model is simulated where grains A and B both have the same orientation to resemble a crack nucleating inside a grain. Conversely, there are other models where grains A and B have differing orientations to resemble a crack nucleating on a grain boundary. In all but three models, the particle is modeled to best represent Al_7Cu_2Fe: linear elastic, isotropic with a Young's Modulus of 166 GPa and a Poisson's Ratio of 0.3. However, for the strong orientation and an intragranularly nucleated crack, alternate models are made for all three crack lengths where the particle is assigned the strong FCC orientation. These alternate models are compared to the models where the elastic particle is present to determine the influence of the particle on MSFC metrics.

Multiple microstructural fatigue metrics are followed in the neighborhood of the crack. For the previously motivated reasons, ΔCTD is utilized to measure crack blunting. Since blunting is caused by permanent deformation in the neighborhood of the crack, the mechanism of such deformation for FCC materials - accumulated irreversible slip on the 12 primary slip planes - is to be calculated and compared with CTD. The same five slip-based metrics studied by Hochhalter *et al.* [31, 32] for nucleation, Equation 1.3 through Equation 1.7, are used here.

$$D_1 = \max_{\alpha} \gamma^{\alpha} \tag{1.3}$$

$$D_2 = \max_{p} \gamma^{p} \tag{1.4}$$

$$D_3 = \gamma = \sum_{\alpha=0}^{N_s} \gamma^{\alpha} \tag{1.5}$$

$$D_4 = \max_{p} \int_0^t \sum_{\alpha=0}^{N_d} \left| \dot{\gamma}_p^{\alpha} \tau_p^{\alpha} \right| dt \tag{1.6}$$

$$D_5 = \max_{p} \int_0^t \sum_{\alpha=0}^{N_d} \left| \dot{\gamma}_p^{\alpha} \right| \left(1 + k \frac{\langle \sigma_n^p \rangle}{g_o} \right) dt \tag{1.7}$$

D_1 is the maximum of the slips, γ^{α}, accumulated on the 12 slip systems, α. D_2 is the maximum of the slips, γ^p, accumulated on the 4 slip planes, p. D_3 is the sum of all slips accumulated on the 12 slip systems. D_4 is a measure of the maximum of energies dissipated due to plastic slip on the 4 slip planes, where energy is the product of the slip rate, $\dot{\gamma}_p^{\alpha}$, and resolved shear stress, τ_p^{α}, on a plane. D_5 is also a measure of the maximum of energies dissipated on the 4 slip planes, but this last metric includes stress normal to the plane, σ_n^p. Since Hochhalter *et al.* [32] found the increase rate of irreversible slip per cycle, ΔD_i for $i = 1...5$, to be related to the number of cycles required for nucleation, this metric is also analyzed here. Maximum stress, both the maximum principal stress, σ_1, and the maximum tangential stress, $\sigma_{\theta\theta}^{max}$, in the neighborhood of the crack and angular location, θ, of

Table 1.3: All permutations of crack sizes and region properties simulated for the baseline model shown in Figure 1.4. Region properties are identified as 'elastic' for linear elastic, isotropic or one of the three texture orientation identifiers from Table 1.1 for crystal plastic.

			region properties		
model ID	crack size	particle	grain A	grain B	grain C
M1	a_1	elastic	strong	strong	rotated
M2	a_1	strong	strong	strong	rotated
M3	a_1	elastic	rotated	rotated	rotated
M4	a_1	elastic	weak	weak	rotated
M5	a_1	elastic	strong	weak	rotated
M6	a_1	elastic	strong	rotated	weak
M7	a_1	elastic	rotated	weak	strong
M8	a_2	elastic	strong	strong	rotated
M9	a_2	strong	strong	strong	rotated
M10	a_2	elastic	rotated	rotated	rotated
M11	a_2	elastic	weak	weak	rotated
M12	a_2	elastic	strong	weak	rotated
M13	a_2	elastic	strong	rotated	weak
M14	a_2	elastic	rotated	weak	strong
M15	a_3	elastic	strong	strong	rotated
M16	a_3	strong	strong	strong	rotated
M17	a_3	elastic	rotated	rotated	rotated
M18	a_3	elastic	weak	weak	rotated
M19	a_3	elastic	strong	weak	rotated
M20	a_3	elastic	strong	rotated	weak
M21	a_3	elastic	rotated	weak	strong

$\sigma_{\theta\theta}^{max}$ along the non-local arc are also investigated, because Hochhalter *et al.* found maximum tangential stress to also be related to the number of cycles to nucleation and θ to align with the direction of nucleation.

1.1.3 Baseline simulation methodology

The remainder of this paper presents the significant findings from simulations performed on the baseline model. First, Section 1.2 summarizes a mesh convergence study performed to determine the mesh density required for convergence of the computed MSFC metrics. Subsequently, Section 1.3 parametrically evaluates dependence of MSFC metrics on the various microstructural heterogeneities represented by the 21 baseline model configurations. In conclusion, Section 1.4 summarizes the significant findings and motivates subsequent studies where the MSFC metrics will be calibrated and validated for simulating MSFC propagation rates and directions.

1.2 Mesh convergence

In this mesh convergence study, simulation results are compared along and near the nucleated crack front for the two meshes in Figure 1.5. For the coarse mesh, Figure 1.5(b), the ratio of element size along the crack front, h_f, to crack diameter, $2a$, is approximately 0.01. Hochhalter *et al.* [31] found this ratio to be necessary for convergence of non-local slip-based metrics ahead of an incubated crack. To determine whether this element size is also sufficient for convergence in this study, a fine mesh, Figure 1.5(c), with h_f to $2a$ ratio of approximately 0.0025, is used as a basis for comparison. The fields in both meshes are extracted at 0.75% applied strain in the RD during the first half-cycle of loading. The baseline model discussed here is M1; however, similar results were observed for mesh convergence studies performed on five baseline models. Additionally, the only slip-based metrics from [31] discussed here are D_1 and D_3; however, similar mesh convergence results

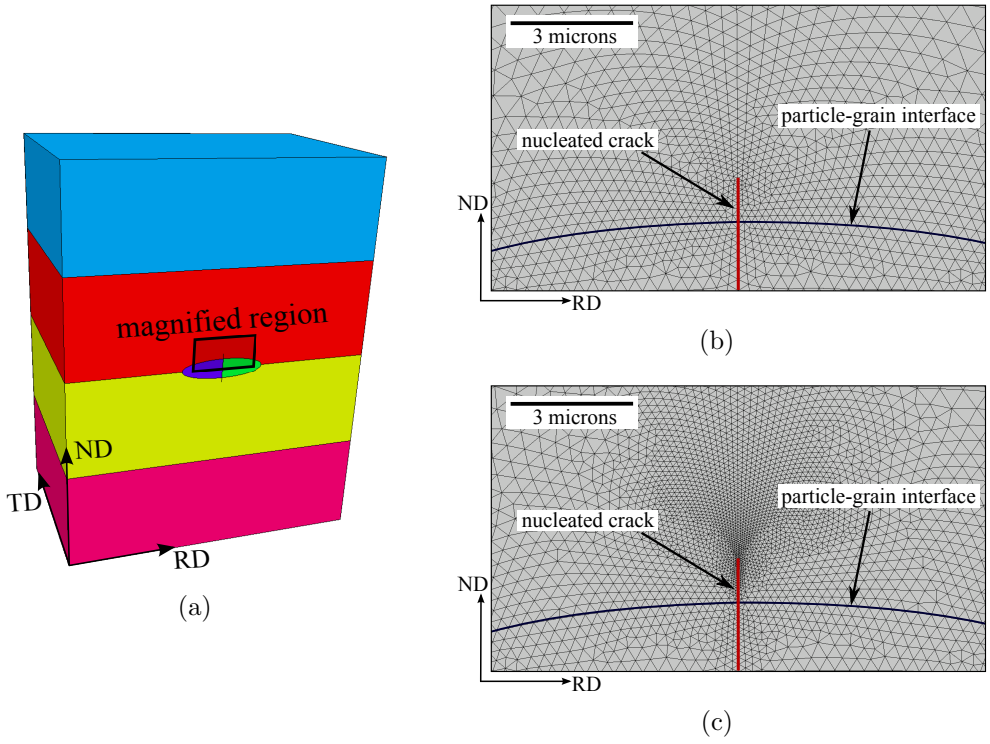

Figure 1.5: (a) Baseline model with magnified view of nucleated crack showing (b) coarse and (c) fine meshes used in the mesh convergence study.

were observed for all five slip-based metrics, D_1 through D_5. Also, the commonly used bases of material and model directions are used: rolling direction (RD) is x, transverse directiorn (TD) is y, and normal direction (ND) is z.

1.2.1 Qualitative evaluation

Qualitative comparisons of the two meshes suggest convergence is achieved with the coarse mesh. The RD-displacement field contours are plotted on the 3X magnification of the deformed shape in Figure 1.6. Although the blunting near the crack front is marginally different between the two meshes, the RD-displacement

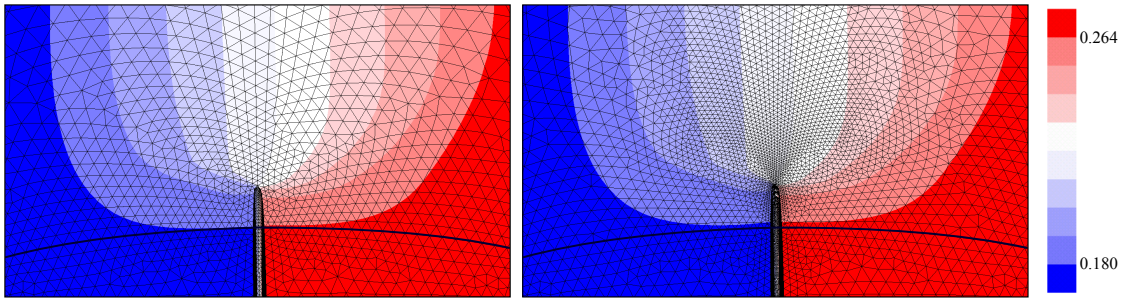

(a) (b)

Figure 1.6: 3X magnification of deformed shape and contours of RD-displacement [μm] for the (a) coarse mesh and (b) fine mesh within the magnified region shown in Figure 1.5.

fields and crack opening profiles are very similar away from the front. As described by [31], the finite element solution at the crack front is divergent with mesh refinement because quadratic finite elements are being applied to approximate a singularity of an unknown degree. Thus, computation of all crack front fields must be non-local. Further numerical studies are described below to determine the appropriate location for CTD computation, *i.e.* some distance close to the crack front where mesh convergence is achieved. The σ_{xx} stress component and the D_1 slip-based metric fields, Figure 1.7 and Figure 1.8, respectively, are also qualitatively similar. However, the D_1 localization lobes are marginally longer in the fine mesh, because the finer mesh is able to better approximate these lobes. This seemingly small difference can significantly change the non-locally calculated slip-based metric values between the coarse and fine meshes if the non-local sampling region intersects these lobes. This is further revealed in the following quantitative mesh convergence evaluation.

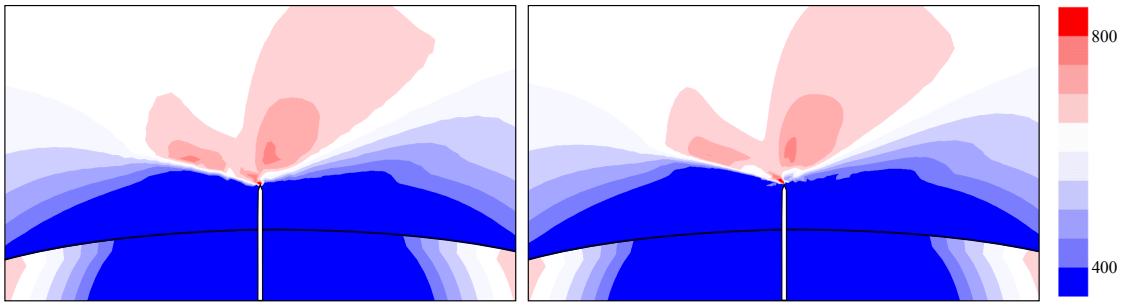

(a) (b)

Figure 1.7: Contours of σ_{xx} [MPa] for the (a) coarse mesh and (b) fine mesh within the magnified region shown in Figure 1.5.

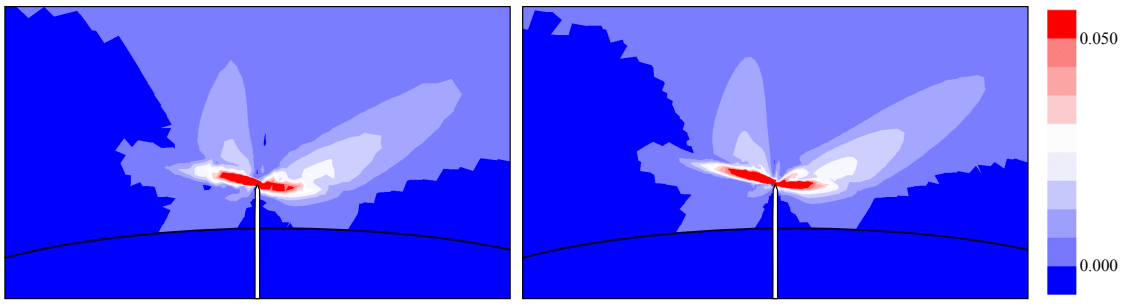

(a) (b)

Figure 1.8: Contours of D_1 for the (a) coarse mesh and (b) fine mesh within the magnified region shown in Figure 1.5.

1.2.2 Quantitative evaluation

To determine quantitatively whether convergence is achieved, the fields near the crack front are considered. Specifically, CTD, D_3^{avg}, and $\sigma_{\theta\theta}^{max}$ are computed non-locally along the entire front. For a point on the crack front, fields are sampled at the locations illustrated in Figure 1.9(a). CTD is the vector magnitude of crack displacement computed at a fixed distance, d, behind the crack front, and D_3^{avg} and $\sigma_{\theta\theta}^{max}$ are the average D_3 and maximum $\sigma_{\theta\theta}$, respectively, computed along a non-local arc at a fixed distance, r, ahead of the crack front. Thus, single values of CTD, D_3^{avg}, and $\sigma_{\theta\theta}^{max}$ are computed for each point along the crack front. For

the coarse element size studied here, Hochhalter *et al.* [31] determined the ratio of r to $2a$ must be at least 0.10 to be sampling within a region of converged fields.

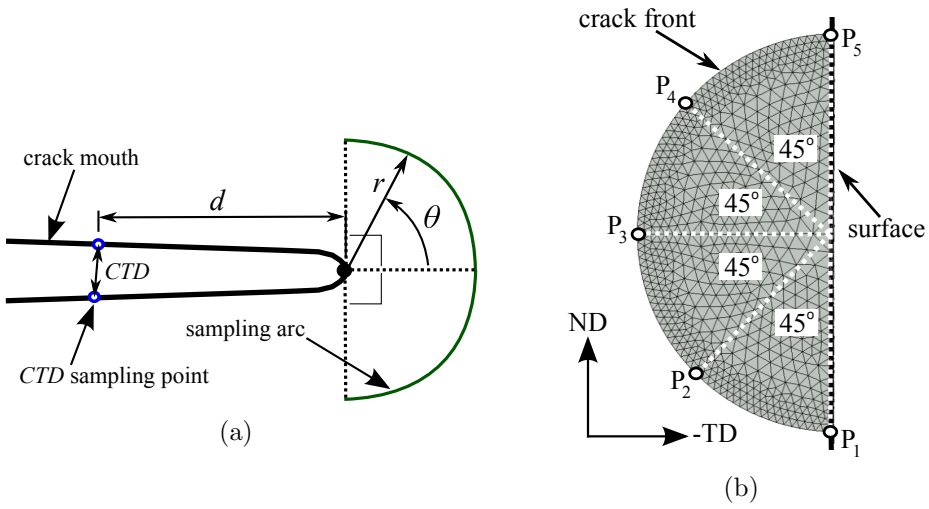

Figure 1.9: Delineation of crack data measurement locations. (a) Sampling arc and CTD sampling point in relation to a typical point on the crack front. (b) Coarse mesh of crack with labels of crack front points P_1 through P_5.

The non-local distance behind the crack front where CTD converges is determined from plots of crack displacement magnitudes, Figure 1.10, along the straight line from point P_1 to point P_5 shown in Figure 1.9(b). Also shown in Figure 1.10 is the percent difference in the displacement magnitudes computed for the two meshes. For this 3 μm crack radius, a, the CTD values for the coarse mesh converge within 5% of the values for the fine mesh at d greater than or equal to approximately 0.2 μm. Thus, a d to $2a$ ratio greater than or equal to 0.05 is deemed necessary for measuring converged displacements in the coarse mesh. For the nucleated crack model studied here, where $2a$ is 6 μm, an r of 1.2 μm and a d of 1.0 μm are chosen for computing CTD, D_3^{avg}, and $\sigma_{\theta\theta}^{max}$, because this was determined to be close enough to the crack front to capture the local fields and, yet, far enough from the crack front for convergence with the coarse mesh.

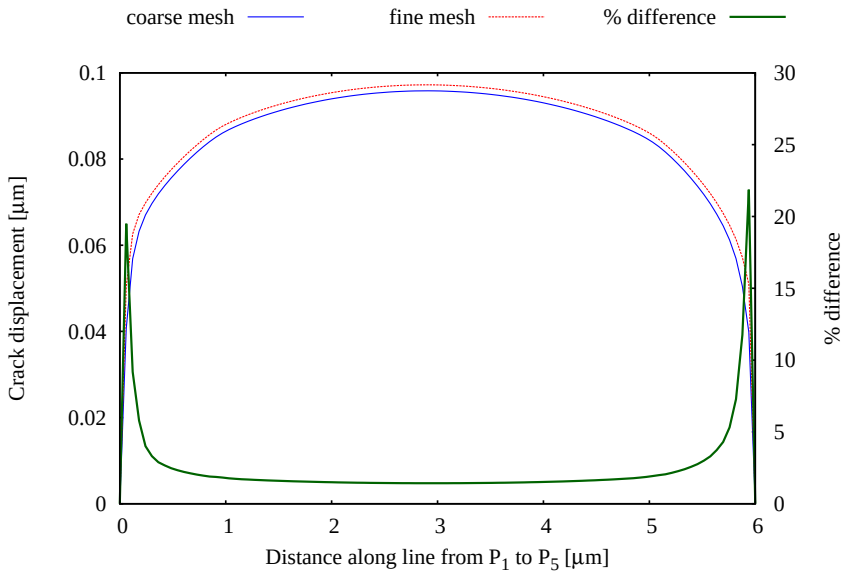

Figure 1.10: Crack displacement magnitudes, and percent differences thereof, for the two mesh densities in Figure 1.5. Measurements are along the line from P_1 to P_5 shown in Figure 1.9(b).

Line plots of CTD, D_3^{avg}, and $\sigma_{\theta\theta}^{max}$ along the crack front are generated by performing non-local calculations at 100 evenly spaced points along the crack front, *i.e.* traversing from point P1 to point P5 in Figure 1.9(b). Figure 1.11 presents three line plots of the percent differences in CTD, D_3^{avg}, and $\sigma_{\theta\theta}^{max}$ calculated from the two meshes. CTD and $\sigma_{\theta\theta}^{max}$ are converged along the entire crack front, with less than 3% and 2% difference, respectively, between the computed values for the coarse and fine meshes. However, differences between the computed values of D_3^{avg} range between 3% and 14%, with an average at approximately 7.5%. Better convergence of D_3^{avg} is preferred, but since the intent of this study is to elucidate trends in various MSFC metrics, this intent can be achieved by always using the same mesh density.

A comparison of the approximate computation times required for the two densities further motivates using the coarse mesh. For this convergence study, the

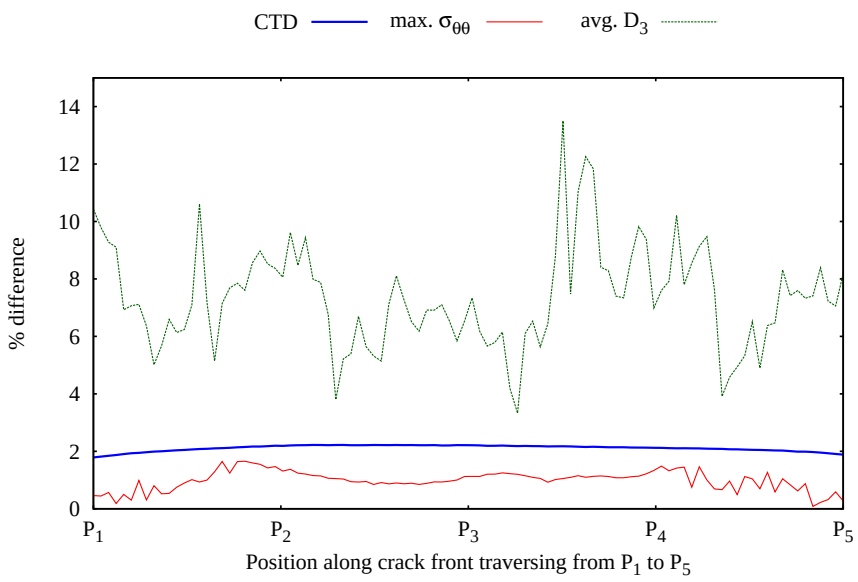

Figure 1.11: % difference plots of CTD, $\sigma_{\theta\theta}^{max}$, and D_3^{avg} measured along crack the front for the two mesh densities in Figure 1.5.

average computation times were approximately 3,000 CPU hours (on a Cray XT4 system with Opteron 2.3 GHz Quad Core processors) for the coarse mesh and approximately 90,000 CPU hours for the fine mesh, a 30X increase in computation time for a 4X increase in mesh density. Therefore, the coarse mesh is deemed sufficient and was used to compute the following results.

1.3 Parametric studies

Through the following parametric studies, relationships among microstructural features and MSFC metrics are revealed. These metrics are calculated from finite element results recorded for the baseline model, Figure 1.4, with the coarse mesh, Figure 1.5(b), and 21 variations of microstructural features, Table 1.3. In all of these scoping studies, the distance behind the crack front, d, where CTD is measured is kept constant at 1.0 μm. However, the non-local arc distance, r, for mea-

suring slip-based metrics and tangential stresses must be varied in length to remain within the regions of mesh convergence and crack front influence. Therefore, the ratio of r to crack diameter, $2a$, is kept constant at 20% for the three crack lengths. The angle, θ, shown in Figure 1.9, is defined here as the angle about a crack front point where $\sigma_{\theta\theta}^{max}$ is computed along the non-local arc. The influence of the particle from which the crack nucleates is investigated in Section 1.3.1. The influence of the grains immediately adjacent to the grain(s) containing a nucleated crack is the focus of Section 1.3.2. Texture influence of the grain(s) containing a nucleated crack is studied in Section 1.3.3. Misorientation influence of the grain boundary containing a transgranularly nucleated crack is investigated in Section 1.3.4. Finally, the calculated metrics for all models are summarized in Section 1.3.5, and, from this summary, overall trends are revealed. For all of these parametric studies, simulations were run to the peak of the second load cycle, unless otherwise specified. Also unless otherwise specified, computed ΔCTD is from valley to peak of the second load cycle, $\sigma_{\theta\theta}^{max}$, θ, and D_3^{avg} are from the peak of the second load cycle, and ΔD_3^{avg} is from the peak of the first load cycle to the peak of the second load cycle. When comparing results among the studies presented here, the reader must be aware the ranges of ordinate values in the line plots vary among the studies. These variations were deemed necessary to best present results within each study.

1.3.1 Particle influence domain

The intent of this first study is to determine the crack sizes where the particle from which the crack is nucleating significantly influences the MSFC metrics, and the degree to which each MSFC metric is influenced. For all three crack sizes, the orientations of grains A, B, and C are kept the same and only the properties of the

particle are varied. Grains A and B are assigned the strong orientation and grain C is assigned the weak orientation. Results are then compared for the particle region having its typical linear elastic, isotropic properties versus the particle region being given the same, strong orientation as its neighboring grains, grain A and grain B. The models compared are M1 and M2 for crack size a_1, M8 and M9 for crack size a_2, and M15 and M16 for crack size a_3.

Figure 1.12 presents the line plots of percent differences in MSFC metrics between the models having and not having the elastic particle for the three crack sizes. This clearly reveals that the particle only influences MSFC metrics for the smallest crack size, a_1. At this crack size, the particle causes ΔCTD, Figure 1.12(a), to increase by approximately 11% at the endpoints of the crack front and approximately 7.5% at the midpoint. Therefore, plane stress conditions increase the effects of the particle for sufficiently small crack sizes. At crack size a_1, the ratio of MSFC size to incubated crack size, a/L_p^{ND}, is 1.5, and at crack size a_2, this ratio is 5.5. Based on this limited study, the notch root influence region of the particle appears to extend between 1.5 and 5.5 times the particle ND radius beyond the particle. Within this notch root influence region, ΔCTD is the most influenced of the investigated MSFC metrics. D_3^{avg}, Figure 1.12(c), is influenced the second most and it follows the same pattern as ΔCTD along the crack front: varying from approximately 6% near the endpoints to 0% at the midpoint. $\sigma_{\theta\theta}^{max}$, Figure 1.12(d), and angular location, θ, of $\sigma_{\theta\theta}^{max}$ on the non-local sampling arc, Figure 1.12(b), vary negligibly, even at crack size a_1. θ is measured from -90° to +90° with 0° being no kink angle, *i.e.* in the same plane as the crack. θ in this particle influence study was typically at 0° and always between -10° and +10°. Therefore, if the crack is propagating in Stage II, it will do so in a self-similar manner.

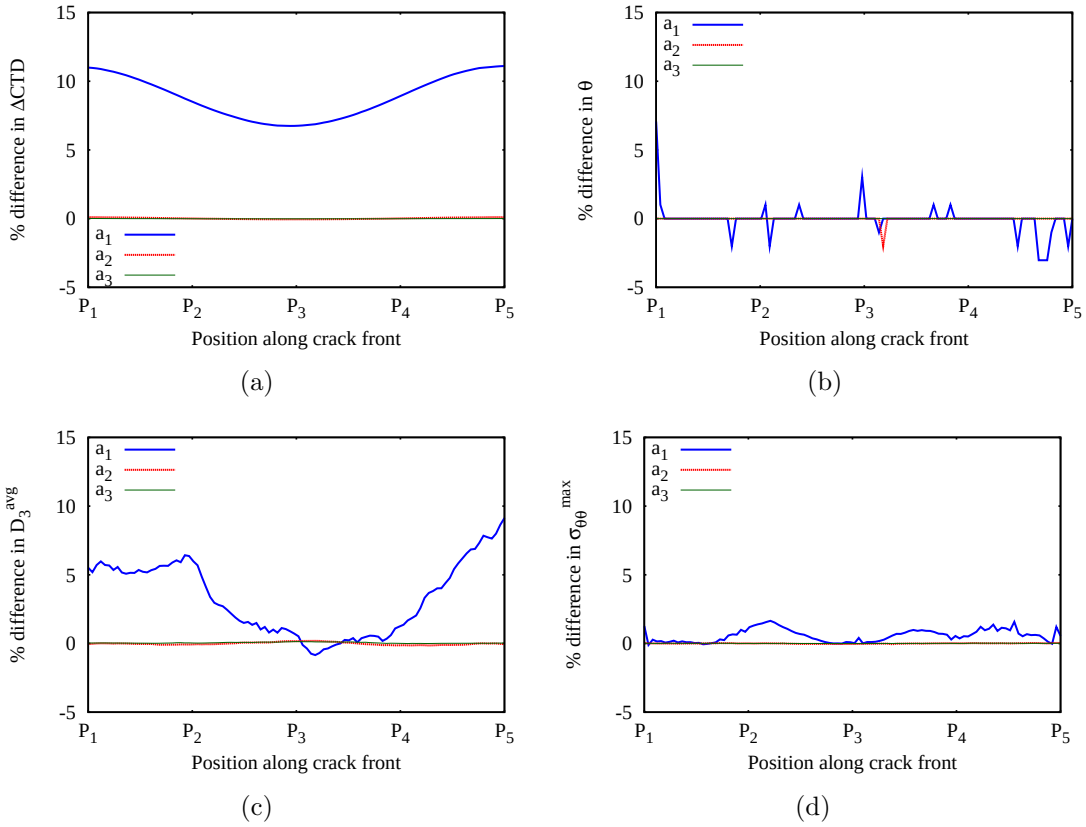

Figure 1.12: Line plots of particle influence on microstructural fatigue metrics: (a) ΔCTD; (b) θ; D_3^{avg}; and, (d) $\sigma_{\theta\theta}^{max}$. Percent difference in each metric is from a model with a particle to a model without a particle for crack lengths a_1, a_2, and a_3.

Figure 1.13 and Figure 1.14 are magnified views of D_3 contours and first principal stress, σ_1, contours, respectively, in the neighborhood of the length a_1 crack. The region shown is on the RD-ND free surface containing the particle. σ_1 in the presence of an elastic particle, Figure 1.14(a), increases noticeably at the RD_{min} and RD_{max} tips of the particle. Even though in Figure 1.12(c) D_3^{avg} is shown to increase at crack length a_1 due to the presence of the particle, this is not noticeable in the D_3 contour plots; the D_3 contours for an elastic particle, Figure 1.13(a), appear almost identical to the contours without the elastic particle, Figure 1.13(b). It is likely that the high stresses at the tips of the particle at crack length a_1 (com-

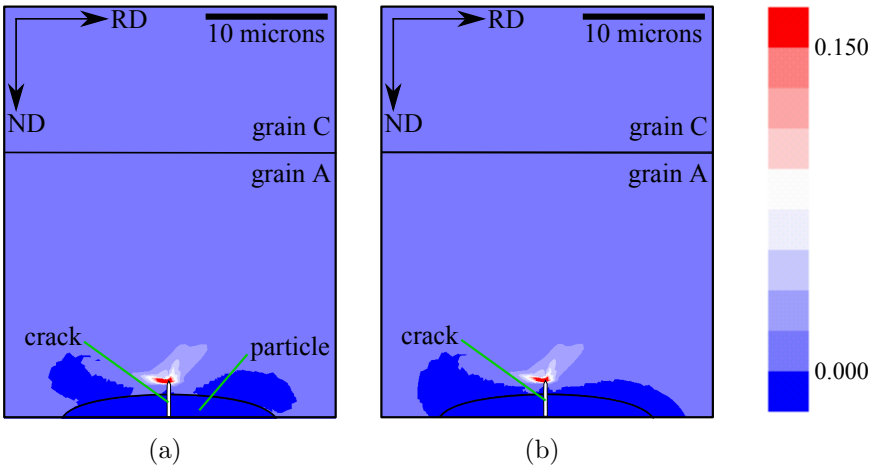

Figure 1.13: Contour plots of particle influence on slip-based metric D_3^{avg} for crack length a_1. (a) Strong orientation for grain A and linear elastic, isotropic for the particle. (b) Strong orientation for grain A and for the domain that is the particle in (a).

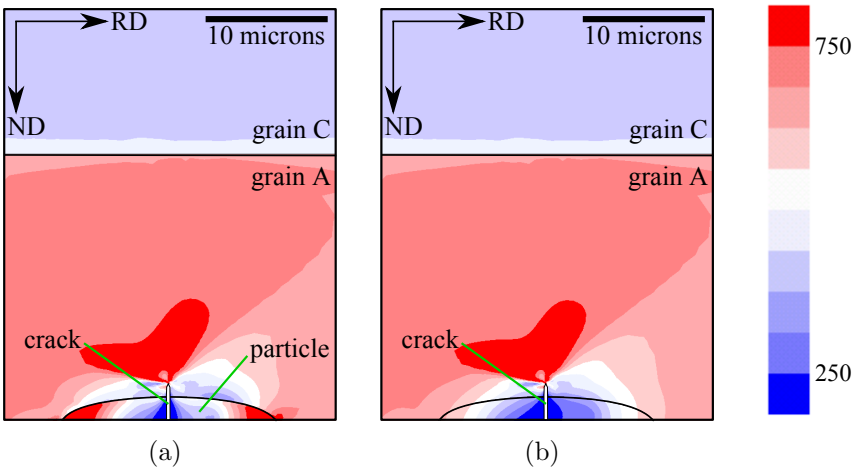

Figure 1.14: Contour plots of particle influence on first principal stress σ_1 [MPa] for crack length a_1. (a) Strong orientation for grain A and linear elastic, isotropic for the particle. (b) Strong orientation for grain A and for the domain that is the particle in (a).

pare Figure 1.14(a) to Figure 1.14(b)) increases the driving forces on the crack, thus resulting in the increased ΔCTD and D_3^{avg} along the crack front observed in Figure 1.12.

1.3.2 Transgranular domain

The goal of this second study is to determine at which crack sizes an intragranularly nucleated MSFC behaves transgranularly. A transgranular crack is one that is close enough to one or multiple grain boundaries that multiple grains influence the crack propagation rate and direction. Assuming the metrics studied here gauge the mechanisms of MSFC propagation, then the fields from which these metrics are computed are also likely to be influenced by multiple grains for a transgranular crack. Therefore, these fields are evaluated here to get insight as to when the crack transitions from intragranular to transgranular.

Figure 1.15 and Figure 1.16 show contour plots of D_3 and σ_1, respectively, as an intragranularly nucleated crack grows from a_1 to a_3. The models compared are M2, M9, and M16. In all three models, the particle region, grain A, and grain B are the strong orientation, and grain C is the rotated orientation; the only material interface is at grain boundary A/C in the figures shown. D_3 is not influenced by the misorientation at the grain boundary until it grows to crack length a_3, which is 1 μm from the grain boundary. However, σ_1 appears to be influenced by the misorientation at the grain boundary when the crack is at length a_2, which is 9 μm from the grain boundary. Since grains are commonly around 20 μm in width in the ND [76], stresses in the neighborhood of the crack will be frequently, if not always, influenced by the heterogeneity of neighboring grains. The influence of neighboring grains on CTD is not evaluated here, because none of the 21 simulated baseline model configurations separate crack size influence on CTD from neighboring grain influence, *i.e.* the crack is always moved closer to the neighboring grain by increasing the crack size.

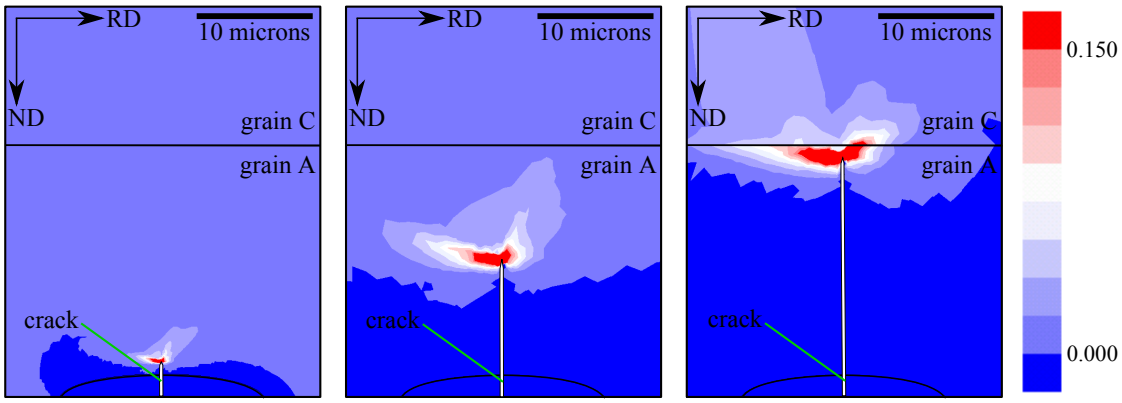

Figure 1.15: Contour plots of transgranular influence on slip-based metric D_3 for crack lengths (a) a_1, (b) a_2, and (c) a_3. In all three plots, the particle region and grain A are the strong orientation and grain C is the rotated orientation.

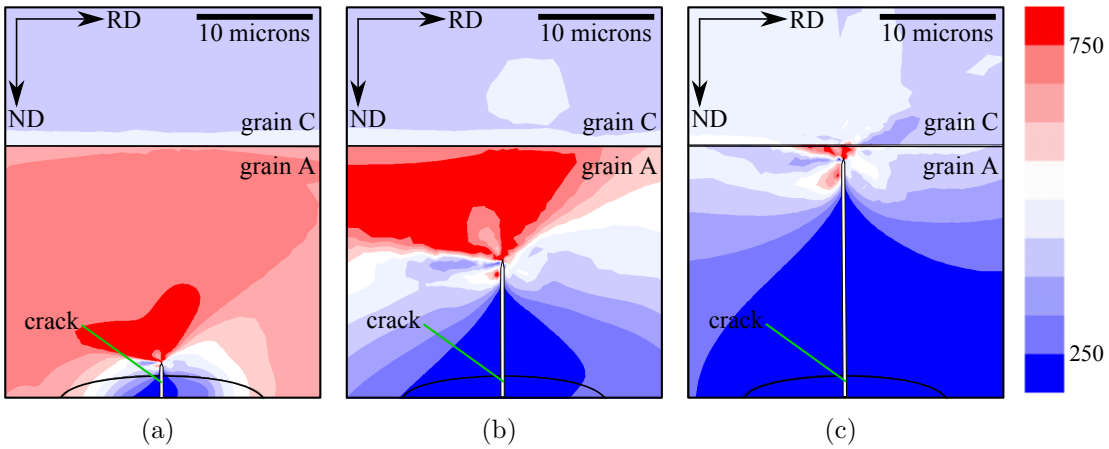

Figure 1.16: Contour plots of transgranular influence on first principal stress σ_1 [MPa] for crack lengths (a) a_1, (b) a_2, and (c) a_3. In all three plots, the particle region and grain A are the strong orientation and grain C is the rotated orientation.

1.3.3 Orientation influence on an intragranularly nucleated crack

The goal of this study is to determine orientation influence on an intragranularly nucleated crack. Grains A and B are always the same orientation, grain C is always the rotated orientation, and the particle is always elastic. Orientation influence is studied by varying the orientation of grain A/B. Results of this study for crack sizes a_1, a_2, and a_3 are presented and evaluated in Section 1.3.3.1, Section 1.3.3.2, and Section 1.3.3.3, respectively. At crack length a_1, models M1, M3, and M4 are compared, at crack length a_2, models M8, M10, and M11 are compared, and at crack length a_3, models M15, M17, and M18 are compared.

1.3.3.1 Crack size a_1

Line plots of the MSFC metrics for all three orientations and crack length a_1 are shown in Figure 1.17. The shapes of ΔCTD along the crack front, Figure 1.17(a), are nearly identical for all three orientations: between 0.08 and 0.085 μm at the endpoints and between 0.06 and 0.07 μm at the midpoint. The percent differences in ΔCTD, Figure 1.17(b), show 6% or less variation in the metrics with changes in orientation, and the difference in ΔCTD between the strong and weak orientations is approximately twice the difference between the weak and rotated orientations. The angle θ, in Figure 1.17(c), is very similar for the weak and strong orientations, but differs slightly for the rotated orientation. The average θ stays close to 0° along the entire crack front for the rotated orientation, while it slopes from approximately +15° at P_1 to -15° at P_5 for the weak and strong orientations. The rotated orientation is known to cause symmetric slip, so it is not surprising

that this orientation produces more symmetric results along the crack front. If θ is determined to be a good predictor of MSFC propagation direction in AA7075-T651, then the crack should be propagated at a slight tilt angle in grains with orientations that align close to the weak and strong orientations.

Interestingly, the rotated orientation and the weak/strong orientations demonstrate competing MSFC metrics if combined high stress and high slip indicate faster MSFC propagation in the same manner that this combination is found to indicate earlier nucleation [32]. For nucleation, it was determined that higher $\sigma_{\theta\theta}^{max}$ required a lower D_3^{avg} for nucleation to occur, and that a higher ΔD_3^{avg} can result in reaching the required D_3^{avg} in fewer cycles. Figure 1.17(d), Figure 1.17(e), and Figure 1.17(f) are evaluated here under the assumption that these same indicators are true for MSFC propagation rate. The $\sigma_{\theta\theta}^{max}$ result is very similar for the weak and strong orientations and approximately 60% higher than $\sigma_{\theta\theta}^{max}$ for the weak orientation. However, D_3^{avg} values are similar for all three orientations and ΔD_3^{avg} increases fastest for the rotated orientation, especially at the crack front endpoints. In fact, for the weak orientation, D_3^{avg} does not increase at all between the first and second load cycles. Therefore, it appears that an MSFC nucleating in a weak orientation grain will never propagate if the stress is not high enough for it to do so in the first load cycle after nucleation. Furthermore, since the rotated orientation has the highest ΔD_3^{avg}, that orientation could lead to the fastest MSFC propagation rates even though the driving force, $\sigma_{\theta\theta}^{max}$, is significantly lower. Replication simulations of actual experiments, like those done in Hochhalter *et al.* [32], are required to understand which, if any, of these seemingly competing mechanisms lends to faster MSFC propagation.

Contour plots of D_3 and σ_1, Figure 1.18 and Figure 1.19, respectively, show

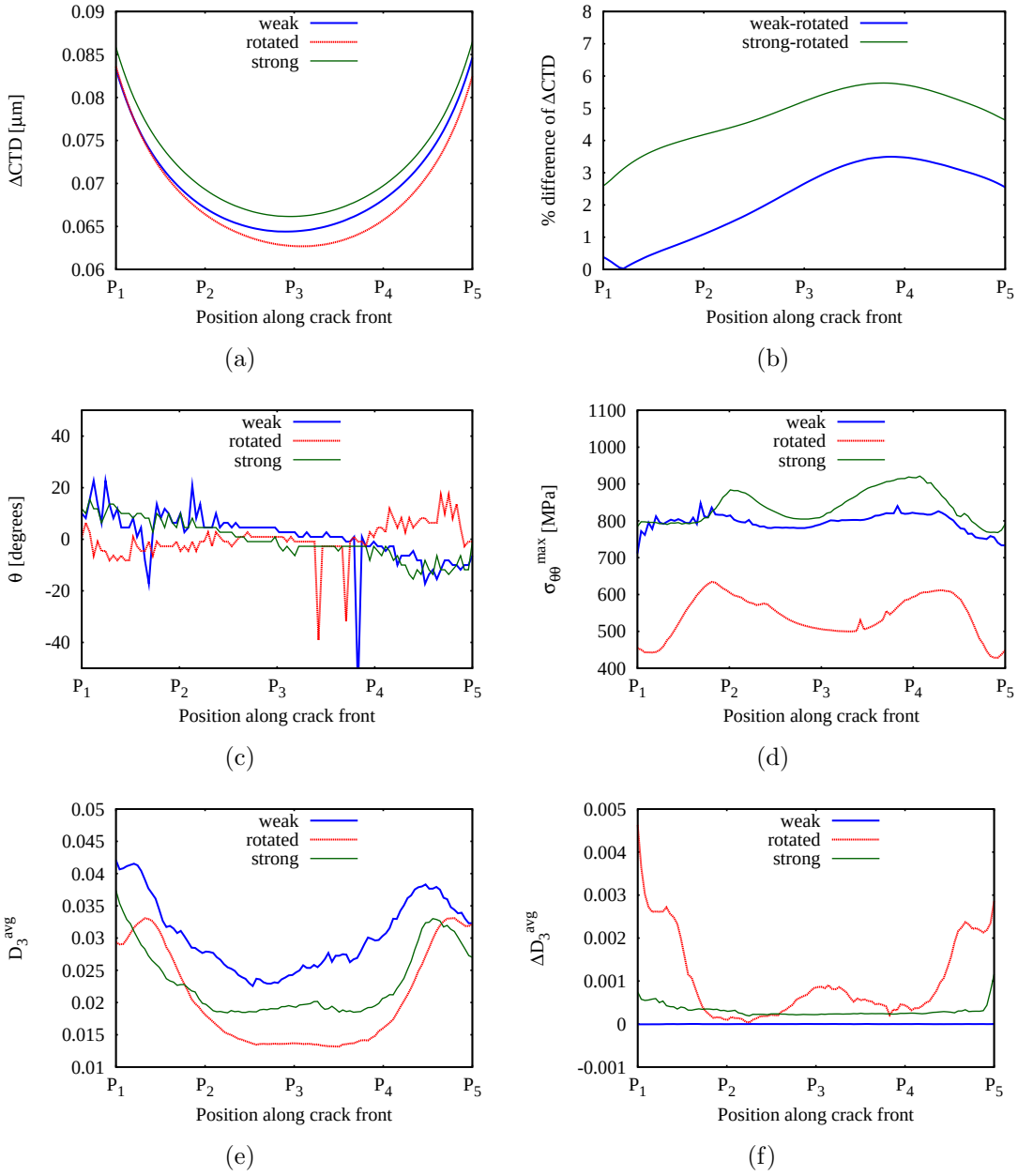

Figure 1.17: Line plots of grain A orientation influence on microstructural fatigue metrics at crack length a_1. (a) ΔCTD; (b) % difference of ΔCTD; (c) θ; (d) $\sigma_{\theta\theta}^{max}$; (e) D_3^{avg}; and, (f) ΔD_3^{avg}.

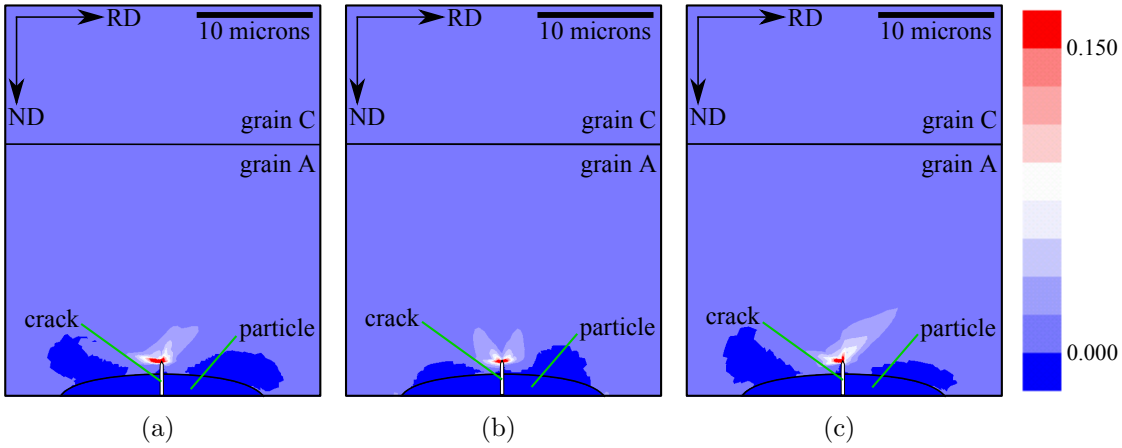

Figure 1.18: Contour plots of grain A orientation influence on slip-based metric D_3 for the three baseline model orientations: (a) strong; (b) rotated; and, (c) weak. In all three plots, the crack length is a_1 and grain C is the rotated orientation.

the differences of these two metrics in the neighborhood of one of the crack front endpoints. The strong and weak orientations cause unsymmetric D_3 about the crack and the rotated orientation causes symmetric D_3. Even though both the weak and rotated orientations have a much higher maximum Schmid factor than the strong orientation, only the rotated orientation shows significant softening, noticed by the much lower stresses away from the crack. This shows one reason why the stresses calculated along the non-local sampling arc, Figure 1.17(d), are much lower for the rotated orientation.

1.3.3.2 Crack size a_2

Line plots of the MSFC metrics for all three orientations and crack length a_2 are shown in Figure 1.20. Again, the shapes of ΔCTD along the crack front, Figure 1.20(a), are nearly identical for all three orientations: between 0.15 and 0.17 μm at the endpoints and between 0.12 and 0.13 μm at the midpoint. The percent

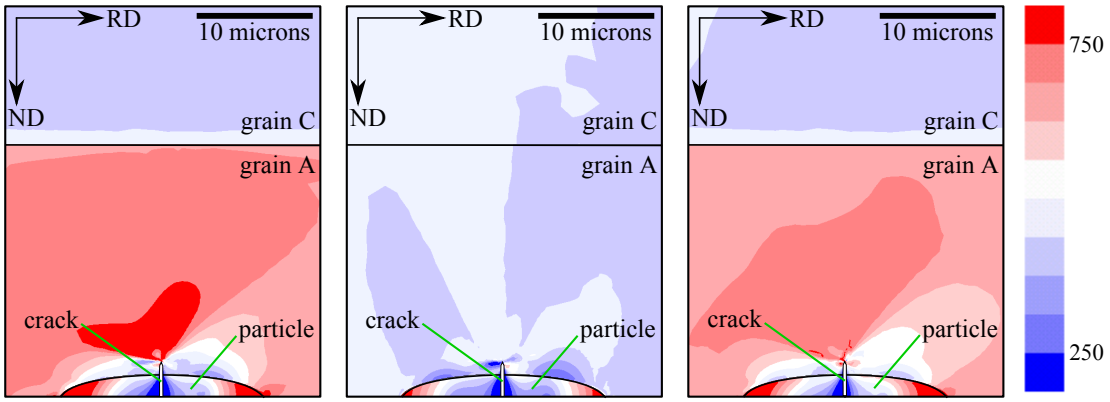

Figure 1.19: Contour plots of grain A orientation influence on first principal stress σ_1 [MPa] for the three baseline model orientations: (a) strong; (b) rotated; and, (c) weak. In all three plots, the crack length is a_1 and grain C is the rotated orientation.

differences in ΔCTD, Figure 1.20(b), show 8% or less variation in the metrics with changes in orientation, but at this crack length, the difference in ΔCTD between the strong and weak orientations is approximately the same as the difference between the weak and rotated orientations. The angle θ, in Figure 1.20(c), is again very similar for the weak and strong orientations and differs slightly for the rotated orientation. $\sigma_{\theta\theta}^{max}$, Figure 1.20(d), is very similar for the weak and strong orientations and approximately 50% higher than $\sigma_{\theta\theta}^{max}$ for the rotated orientation. Also like a_1, D_3^{avg} values, Figure 1.20(e), are similar for all three orientations, but unlike a_1, ΔD_3^{avg}, Figure 1.20(f), is near zero and does not vary much among the orientations.

1.3.3.3 Crack size a_3

Line plots of the MSFC metrics for all three orientations and crack length a_3 are shown in Figure 1.21. Similar trends as a_2 are noticed, except near the crack front

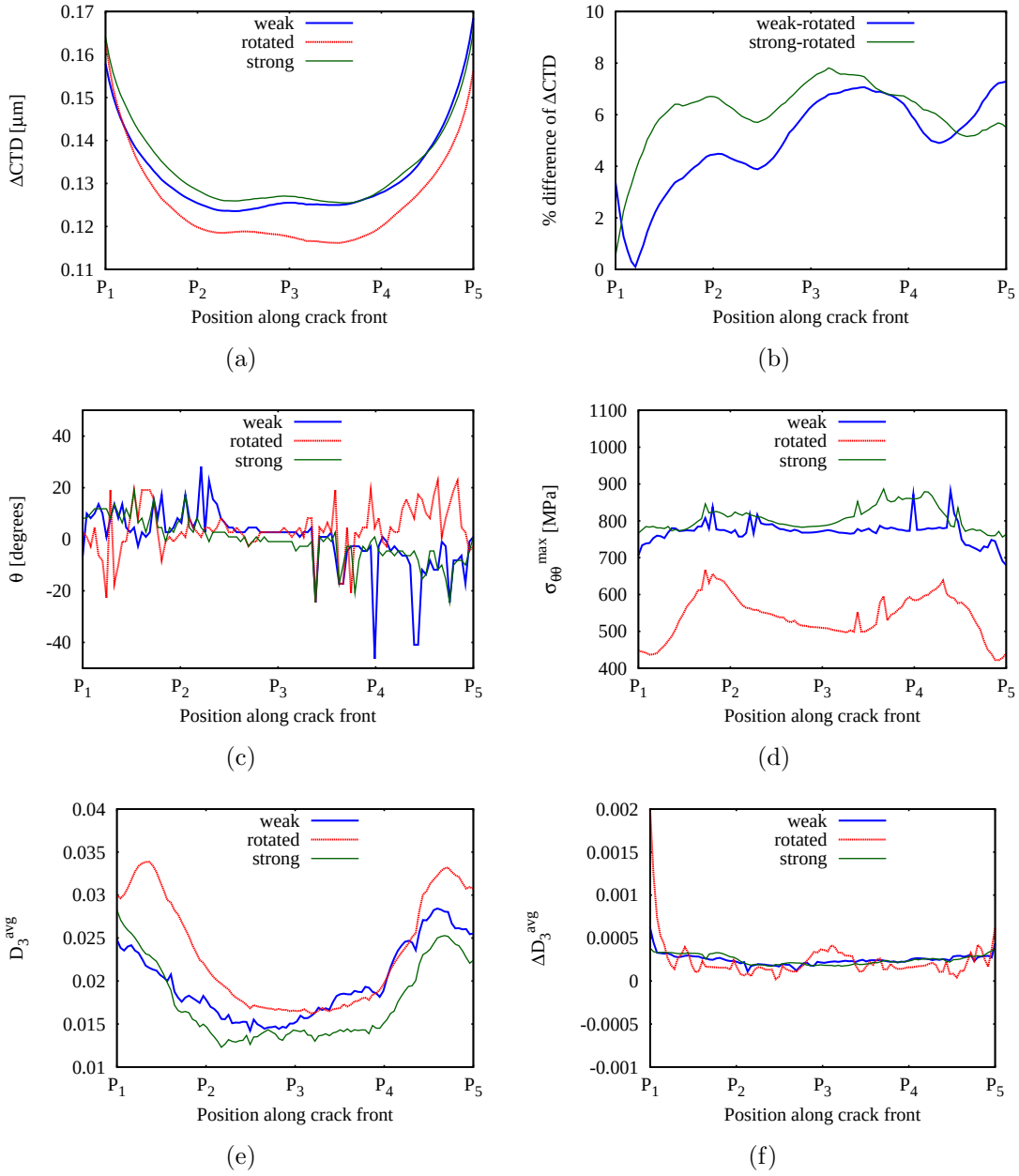

Figure 1.20: Line plots of grain A orientation influence on microstructural fatigue metrics at crack length a_2. (a) ΔCTD; (b) % difference of ΔCTD; (c) θ; (d) $\sigma_{\theta\theta}^{max}$; (e) D_3^{avg}; and, (f) ΔD_3^{avg}.

endpoints, the maximum tangential stresses, Figure 1.21(d), are nearly identical and lower in magnitude than what was recorded for a_2. This is because the crack is very near the grain boundaries with grain C, a rotated orientation grain, at this crack length. In fact, the non-local sampling arcs for D_3^{avg} and $\sigma_{\theta\theta}^{max}$ computation cross into grain C near the crack front endpoints at crack length a_3.

1.3.4 Misorientation influence on a transgranularly nucleated crack

The goal of this fifth study is to determine misorientation influence on a transgranularly nucleated crack, *i.e.* a crack that nucleates on a grain boundary. The case where grains A and B have differing orientation (transgranular nucleation) is compared to the case where grains A and B have the same orientation (intragranular nucleation) to study the influence of the former case. For grains A and B having differing orientation, grain A is the strong orientation and grain B is the weak orientation. For grains A and B having the same orientation, both grains are the strong orientation. The particle is always elastic and grain C is always the rotated orientation. Results of this study for crack sizes a_1, a_2, and a_3 were generated, but since all three crack sizes gave similar trends, only crack size a_1 is discussed here. Models M1 and M5 are compared at this crack length.

Line plots of the MSFC metrics for the two models are shown in Figure 1.22. Overall, the strong/weak misorientation causes very little deviation in MSFC metrics from a crack nucleating completely inside a strong orientation grain. The ΔCTD values, Figure 1.22(a), and their percent difference between the two models, Figure 1.22(b), show that ΔCTD is almost identical with approximately 1%

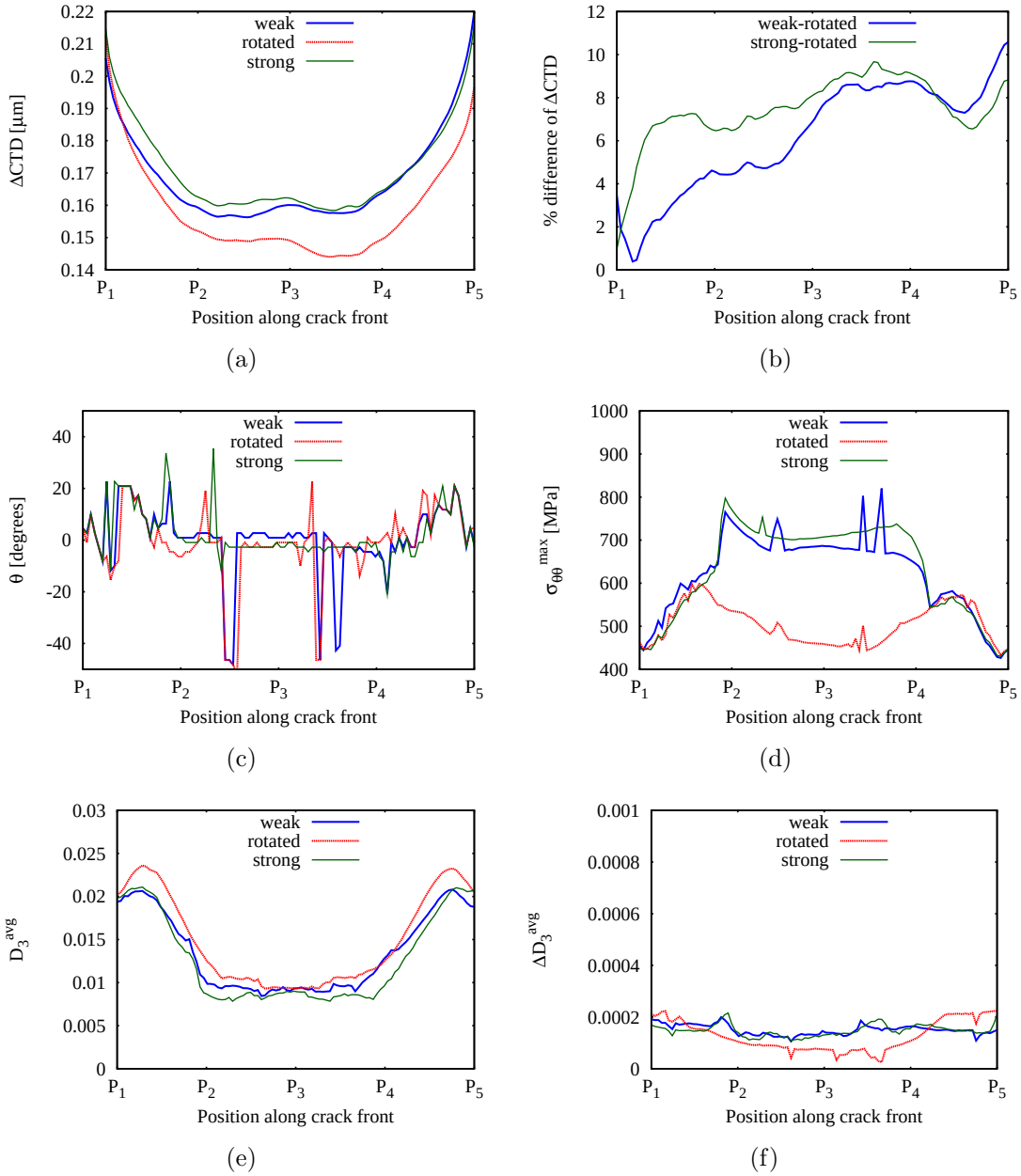

Figure 1.21: Line plots of grain A orientation influence on microstructural fatigue metrics at crack length a_3. (a) ΔCTD; (b) % difference of ΔCTD; (c) θ; (d) $\sigma_{\theta\theta}^{max}$; (e) D_3^{avg}; and, (f) ΔD_3^{avg}.

difference along the entire crack front. The angle of maximum tangential stress, Figure 1.22(c), and ΔD_3^{avg}, Figure 1.22(f), are also almost identical. The values of the maximum tangential stress, Figure 1.22(d), do deviate some in grain B which is not surprising, since grain B is the grain that changes orientation from one model to the other. Furthermore, as expected, grain B being the weak orientation gives slightly lower stress than grain B being the strong orientation. Also, grain B being weak results in higher D_3^{avg} along the entire crack front, as shown in Figure 1.22(e). An intuitive assumption is that an increase in plasticity, *e.g.* an increase in D_3^{avg}, would further blunt the crack, which would be reflected by an increase in ΔCTD. However, this relationship is not observed, possibly because the crack driving force, $\sigma_{\theta\theta}^{max}$, is decreased slightly for the same model where D_3^{avg} is increased slightly.

1.3.5 Summary of all simulation results

Table 1.4 summarizes the averages of MSFC metrics for all simulated baseline models and reveals several distinct trends in MSFC characteristics. Horizontal lines between sets of models delineate the different crack sizes. The top seven models all have crack size a_1, the middle seven models all have crack size a_2, and the bottom seven models all have crack size a_3. Within each crack size grouping, the models are organized from top to bottom by highest ΔCTD to lowest ΔCTD. Here, ΔCTD and the six metrics shown are the averages of the metric values computed along the crack front. If $\Delta CTD(P_j)$ is the ΔCTD computed at point P_j on the crack front, then ΔCTD given for each model in Table 1.4 is the average of all $\Delta CTD(P_j)$ values for that model. The bold texts in the table are models that did not have a particle, and the italics texts are models that had the rotated orientation in grain A and/or B.

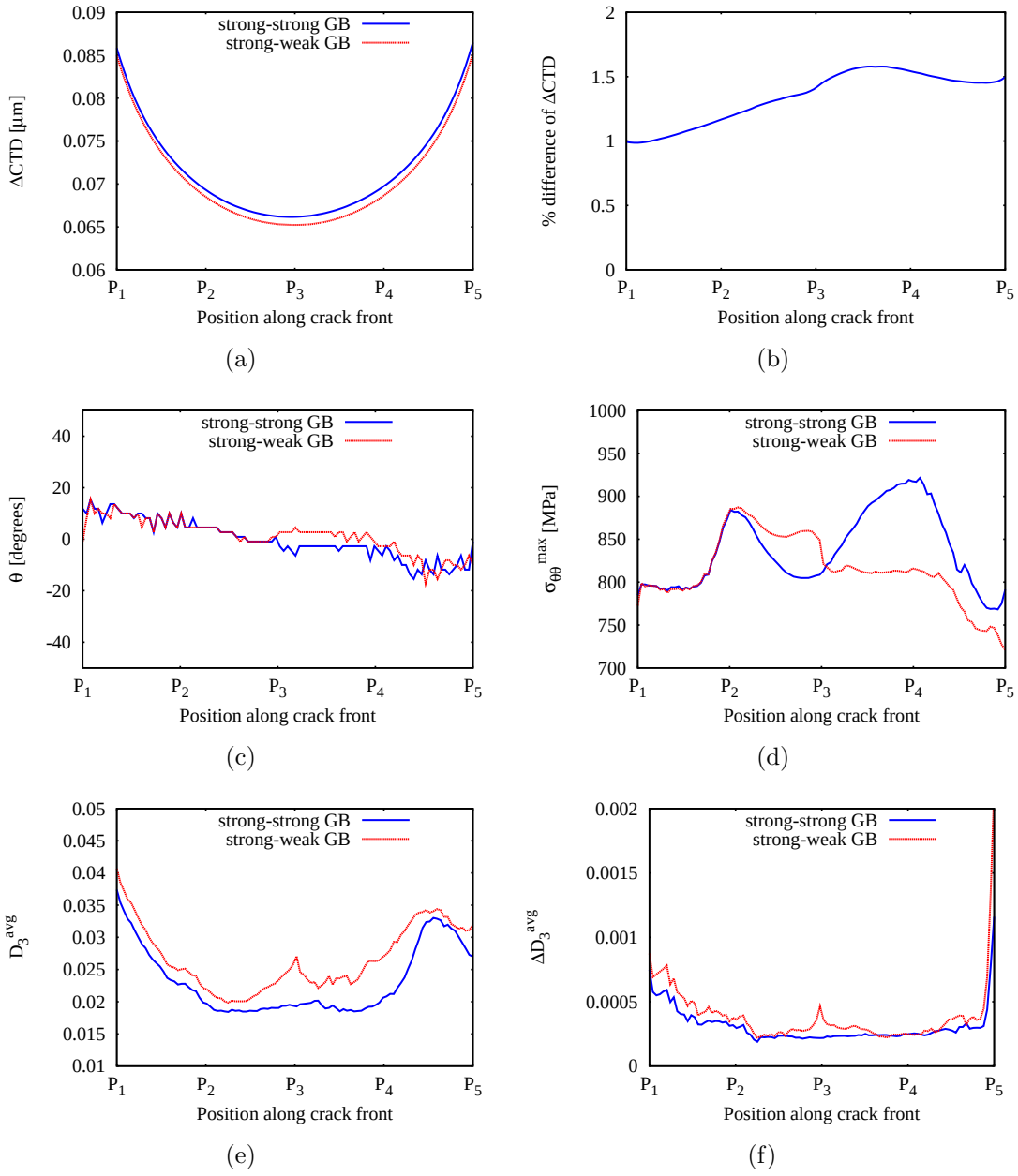

Figure 1.22: Line plots of grain boundary A/B misorientation influence on microstructural fatigue metrics at crack length a_1 and for grain C having the rotated orientation. (a) ΔCTD; (b) % difference of ΔCTD; (c) θ; (d) $\sigma_{\theta\theta}^{max}$; (e) D_3^{avg}; and, (f) ΔD_3^{avg}.

Table 1.4: Averages of MSFC metrics calculated along the crack front for all baseline models listed in Table 1.3. Horizontal lines between datasets divide the three crack sizes: a_1 is at the top, a_2 is in the middle, and a_3 is on the bottom. *Italics texts* are models that have the rotated orientation for grain A and/or grain B. **Bold texts** are models that do not have a particle. ΔCTD, $\Delta CTOD$, and $\Delta CTSD$ are in μm, θ is in degrees, and $\sigma_{\theta\theta}^{max}$ is in MPa.

	average of values along crack front						
model ID	ΔCTD	$\Delta CTOD$	$\Delta CTSD$	θ	$\sigma_{\theta\theta}^{max}$	D_3^{avg}	ΔD_3^{avg}
M1	7.16E-2	7.19E-2	4.57E-4	-0.20	837	2.32E-2	3.10E-4
M5	7.07E-2	7.18E-2	1.93E-3	1.22	814	2.68E-2	3.90E-4
M4	6.97E-2	7.09E-2	8.12E-4	1.04	795	3.05E-2	0.00
M7	*6.88E-2*	*6.97E-2*	*7.16E-4*	*-0.64*	*668*	*2.30E-2*	*6.41E-4*
M3	*6.82E-2*	*6.84E-2*	*2.24E-3*	*-0.16*	*540*	*2.07E-2*	*1.02E-3*
M6	*6.81E-2*	*6.96E-2*	*1.04E-3*	*0.40*	*666*	*1.84E-2*	*6.03E-4*
M2	**6.52E-2**	**6.54E-2**	**2.90E-4**	**-0.13**	**832**	**2.24E-2**	**2.58E-4**
M8	1.34E-1	1.34E-1	2.16E-3	-0.40	807	1.75E-2	2.48E-4
M9	**1.34E-1**	**1.34E-1**	**2.15E-3**	**-0.36**	**807**	**1.75E-2**	**2.51E-4**
M12	1.33E-1	1.34E-1	5.12E-3	-0.60	784	1.90E-2	2.56E-4
M11	1.32E-1	1.33E-1	4.92E-3	0.00	770	1.98E-2	2.48E-4
M14	*1.28E-1*	*1.29E-1*	*4.70E-3*	*0.07*	*662*	*1.75E-2*	*1.80E-4*
M13	*1.27E-1*	*1.29E-1*	*5.09E-3*	*3.20*	*665*	*1.64E-2*	*1.74E-4*
M10	*1.26E-1*	*1.27E-1*	*6.70E-3*	*3.84*	*540*	*2.33E-2*	*2.40E-4*
M15	1.71E-1	1.72E-1	3.75E-3	2.38	632	1.27E-2	1.48E-4
M16	**1.71E-1**	**1.72E-1**	**3.75E-3**	**2.38**	**631**	**1.27E-2**	**1.48E-4**
M19	1.70E-1	1.72E-1	7.00E-3	1.69	625	1.31E-2	1.55E-4
M18	1.69E-1	1.71E-1	8.30E-3	0.40	624	1.36E-2	1.50E-4
M21	*1.63E-1*	*1.64E-1*	*7.99E-3*	*-1.75*	*691*	*1.16E-2*	*1.52E-4*
M20	*1.62E-1*	*1.65E-1*	*6.14E-3*	*0.13*	*675*	*1.11E-2*	*1.28E-4*
M17	*1.59E-1*	*1.61E-1*	*9.64E-3*	*-0.98*	*504*	*1.50E-2*	*1.27E-4*

A comparison of ΔCTD to $\Delta CTOD$ and $\Delta CTSD$, reveals that ΔCTD is opening dominated for all grain orientations and crack sizes. $\Delta CTOD$ is approximately the same value as ΔCTD and $\Delta CTSD$ is always one or two orders of magnitude less than $\Delta CTOD$. Since Stage I is sliding dominated and Stage II is opening dominated, these results suggest the MSFC's studied here are all Stage II.

Even in Stage II, however, significant variations in ΔCTD result from microstructural heterogeneities. At crack size a_1, M2 having a significantly lower ΔCTD shows that particle influences are greater than all other microstructural heterogeneity influences. However, at the other two crack sizes, the absence of the particle in M9 and M16 results in no differences from the comparable models that have particles, M8 and M15, respectively. At all crack lengths, the models not in italics have higher average ΔCTD than the models in italics. This suggests that the rotated orientation causes lower ΔCTD. However, for crack size a_1, ΔD_3^{avg} is higher for cracks inside a rotated orientation grain, which will presumably cause a faster cyclic increase in crack blunting than the other two orientations. This pattern then seemingly reverses at crack size a_2: the cracks not inside rotated orientation grains have higher ΔD_3^{avg}. Although, the two models that have much lower ΔD_3^{avg} at a_2, M13 and M14, are the only two models that do not have the rotated orientation for grain C. Presumably, when a nucleated crack grows to halfway through the first grain (crack size a_2), the plastic slip localization at the crack front is influenced by the next grain ahead of the crack (grain C), and rotated orientations in the next grain favor higher ΔD_3^{avg} than the other orientations. The trend of the rotated orientation favoring higher ΔD_3^{avg} then discontinues at crack length a_3, but observation of the slip fields revealed that slip localization is impeded by model boundaries at this crack length when grain C is the rotated orientation.

1.4 Conclusions and future work

This paper investigated metrics that gauge mechanisms governing a MSFC immediately following matrix crack nucleation, where nucleation in the material studied, AA7075-T651, is extension of a through-particle crack into the surrounding grain(s). Prior related research was reviewed to motivate the MSFC simulation approach, and to determine the main objectives intended to facilitate novel contributions to the fatigue community. The vehicle for achieving these objectives is a simplified, four grain, one surface particle baseline model. A mesh convergence study was performed on this model to determine the appropriate mesh density for convergence of three non-locally calculated MSFC metrics: CTD, maximum tangential stress, and plastic slip accumulation. A ratio of crack front element size to crack size of 0.01 was deemed adequate for mesh convergence of: (a) CTD computed 1.0 μm behind the crack front; and, (b) tangential stresses and slip-based metrics computed 20% of the crack diameter ahead of the crack front. Parametric studies were then performed out to two load cycles to determine the dependence of these metrics on crack size, the particle containing the crack, orientations of grains ahead of the crack, and orientation(s) of grain(s) containing the crack. Significant findings of these parametric studies are summarized here with respect to the four main objectives:

1. *Elucidate the differences between a Stage II MSFC and a MLFC.* For all simulated orientations, $\Delta CTOD$ is the same order of magnitude as ΔCTD and one to two orders of magnitude greater than $\Delta CTSD$, so a Stage II crack is prevalent in these studies. However, immediately following nucleation, when the Stage II crack is 150% of the particle ND size, the particle notch root causes a 10% increase in ΔCTD. Similarly, variation in orientation of

the grain containing a nucleated crack can cause upwards of 6% variation in ΔCTD. Contrarily, a MLFC, by definition, is large enough that influence of microstructural heterogeneity is negligible.

2. *Determine physical relationships among microstructural heterogeneities, near crack stress fields, plastic strain localizations, and ΔCTD of a Stage II MSFC.* In addition to the above findings, other distinct relationships are prevalent among microstructuctural heterogeneities and Stage II MSFC metrics. Immediately after nucleation, when the crack is 150% of the particle ND size, grain orientations with no high Schmid factors, *i.e.* the 'strong' orientation, have the highest ΔCTD and tangential stresses at the second load cycle, while grain orientations with symmetric high Schmid factors, *i.e.* the rotated cube family, have the lowest ΔCTD and tangential stresses. However, based on a comparison of the change in irreversible slip localization from the first to second load cycle, it can be concluded that grain orientations with only one high Schmid factor will not see an increase in crack blunting after the first load cycle, while grain orientations with symmetric high Schmid factors will see significant increase in crack blunting after the first load cycle. Therefore, cracks nucleating in grains with one high Schmid factor will arrest if the initial blunting is not enough to cause propagation during the first load cycle after nucleation. Other significant findings are: MSFC metrics of a transgranularly nucleated crack do not significantly deviate from those of an intragranularly nucleated crack; a nucleated MSFC transitions to trangranular characteristics when it is within approximately 10 μm of the grains immediately adjacent to the grain(s) containing the particle of crack origin; and, the particle notch root influence on the crack disappears by the time the crack has grown to approximately 550% of the particle ND

size.

3. *Quantify ΔCTD dependence on microstructural heterogeneities to incorporate in semi-empirical, phenomenological, and/or statistical models.* In addition to the many generalized quantifications given above, modelers can: extract variations in these quantifications along the crack front by fitting polynomials to the included line plots; and/or, sample statistical descriptors of grain orientations to bin all orientations into the three grain orientations studied here and determine the probability that a nucleated MSFC will encounter each of the 21 microstructural configurations and their respective MSFC metrics.

4. *Illustrate why MSFC propagation needs to be incorporated in high fidelity fatigue life predictions.* Unfortunately, only part of this objective is satisfied here. It is now clear that microstructural heterogeneities substantially influence MSFC metrics. A subsequent paper in this series completes this objective by using replication models of experimental observations to validate MSFC propagation dependence on the MSFC metrics.

ACKNOWLEDGEMENTS

Dr. Gerd Heber developed the parallel finite element code that was used for the finite element simulations presented here. The crystal plasticity model was implemented by Dr. Antoinette Maniatty, Dr. David Littlewood, and Dr. Paul Wawrzynek. Experimental observations were made by Joel Payne and Dr. Elias Anagnostou at the Northrop Grumman Corporation. This work is sponsored by the Defense Advanced Research Projects Agency under contract HR0011-04-C-0003 with Dr. Leo Christodoulou as the DARPA Program Manager. This work is also funded by NASA under contract ARMD-NNX07AB69A with Dr. Ed Glaessgen as the NASA Contract Monitor, and by the U.S. Department of Energy Computational Science Graduate Fellowship Program of the Office of Science and National Nuclear Security Administration in the Department of Energy under contract DE-FG02-97ER25308. The simulations needed to complete this study were carried out on a NASA AMES supercomputer, Pleiades, and on resources of the National Energy Research Scientific Computing Center, which is supported by the Office of Science of the U.S. Department of Energy under contract DE-AC02-05CH11231.

CHAPTER 2

GEOMETRICALLY EXPLICIT, THREE-DIMENSIONAL FINITE ELEMENT MODELING OF STATISTICALLY REALISTIC MICROSTRUCTURES WITH FATIGUE CRACKS

Modern computational capabilities provide the opportunity to model accurately fatigue damage evolution over all governing length scales. For many materials and loading conditions, the governing length scale for a majority of the fatigue life is the microstructural scale. However, fatigue crack growth models have traditionally simplified or ignored the propagation mechanisms and inherent heterogeneities contributing to the stochasticity in fatigue damage evolution at this scale. The main thrust of the work presented here is toward the creation of a computational framework that accurately and probabilistically models fatigue crack propagation at the microstructural scale for a proof-test material, aluminum alloy 7075-T651. Toolsets are presented that generate and discretize statistically accurate microstructure geometry models and explicitly simulate the evolution of microstructurally small fatigue cracks. Analysis results are given for a typical microstructure finite element model prior to and immediately following the incubation of fatigue cracks. In conclusion, the computational feasibility, limitations, and future applications of this approach are critically evaluated. The high computational demand of this approach currently limits its application to only a few simulations. However, this approach can be incorporated into a probabilistic framework wherein a few, high fidelity microstructure-scale fatigue simulations can be performed on pre-determined fatigue life limiting microstructural features to greatly improve fidelity in the minimum life tail of a probabilistic fatigue life distribution.

2.1 Introduction

The aging of existing airframes and the development of novel materials engineering, experimental observation, sensing, and computational simulation approaches are increasingly motivating and facilitating new structural prognosis philosophies in the aerospace community. The traditional structural integrity philosophies of the United States Air Force and Navy, damage tolerance and safe-life, respectively, are known to be overly conservative, because they simplify or ignore, altogether, the mechanisms governing fatigue. Moreover, due to budgetary constraints not allowing for premature replacement of structural components, fleet managers are often required to reduce the safety and functional capabilities of aircraft by using airframes beyond their designed fatigue lives. Therefore, more physically accurate fatigue life approaches are demanded to simultaneously maximize usage and safety of aging aircraft structures [35]. This demand and the extensive supply of structural fatigue knowledge gained since incorporation of the damage tolerance and safe-life approaches have increased the need for a modern structural life management philosophy that combines the inherent physics and stochastics of fatigue damage evolution to predict probabilistically the number of cycles to failure for structural components by considering their load and environmental histories [14]. The locations of life limiting hot spots in a structural component can usually be determined through component-scale fatigue crack propagation simulations [16]. However, a majority of the fatigue life, and the inherent stochasticity in the number of load cycles to generate a life-limiting crack, are governed by microstructural processes [10, 14, 17, 77]. The goal of the work presented here is to create a computational framework, as part of a modern structural integrity prognosis system, that accurately and probabilistically models fatigue crack propagation at the microstructural length scale for a proof-test material, aluminum alloy (AA)7075-

T651. This alloy, used for decades, presents an immediate need for prognosis of its late age fatigue behavior, and a rich history of its usage and experimental data from which prognosis models can be validated. However, the framework is intended to be generalizable to structural prognoses involving other materials and, possibly, to engineering microstructurally more fatigue resistant materials.

In the microstructurally small fatigue crack (MSFC) phase, heterogeneities in microstructural features govern when and where cracks will originate and propagate. Consider, for example, the scanning electron micrographs and inverse pole figure of AA7075-T651 in Figure 2.1. In this material, cracks are known to originate at some, but not all, of the Al_7Cu_2Fe constituent particles [7, 59, 86]: notice the cracks (dark regions) starting, in a seemingly random manner, from some of the particles (white regions) in Figure 2.1(a), such as the particle in Figure 2.1(b). Subsequent MSFC propagation directions and rates are largely dependent on the grain orientations and geometries: notice the distinct changes in propagation direction at grain boundaries in Figure 2.1(c). Since location, geometry, and material property distributions of these governing microstructural heterogeneities are random, the resulting MSFC locations and lengths are spatially and temporally stochastic.

Frequently in the fatigue literature, the appearance and some small amount of MSFC propagation is recognized as one event, 'initiation'. However, initiation is actually a combination of three physically unique stages, defined here, and in previous studies [7, 31, 32, 82], as 'incubation', 'nucleation', and 'MSFC propagation', illustrated by (i), (ii), and (iii), respectively, in Figure 2.1(c). For AA 7075-T651 in high strain fatigue, incubation is the cracking of Al_7Cu_2Fe particle inclusions [7,59,86], nucleation is the extension of a previously incubated crack across the particle-grain interface [31, 32], and MSFC propagation is microstructure-

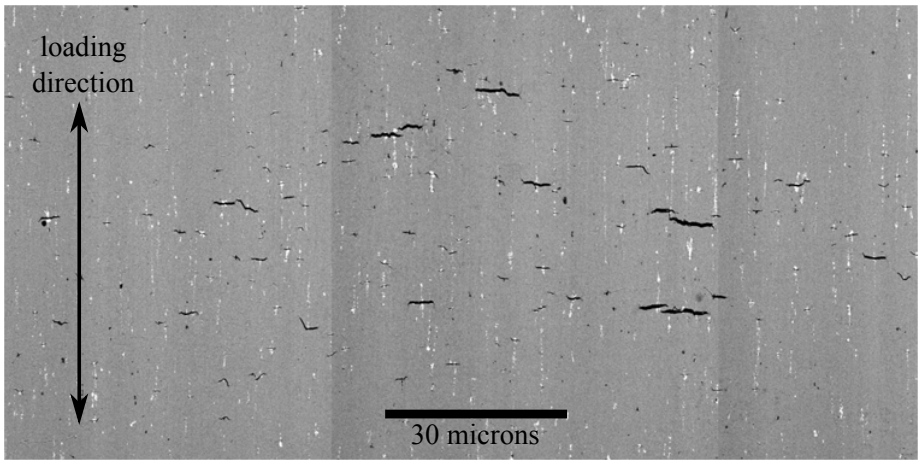

(a)

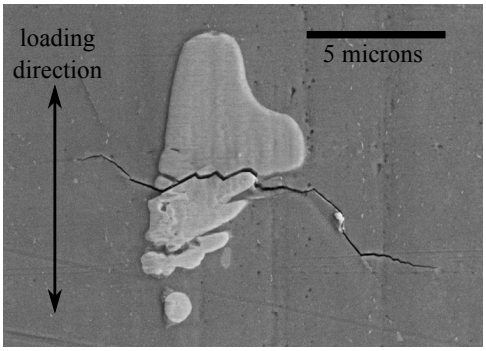

(b)

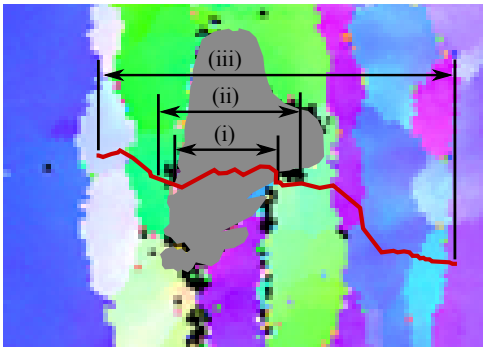

(c)

Figure 2.1: (a) Scanning electron micrograph of AA7075-T651 microstructure at a highly stressed region with many MSFC's. (b) Magnified scanning electron micrograph of a typical MSFC growing from a second-phase particle. (c) Inverse pole figure of the same MSFC with highlight of the crack path and demarcation of the three MSFC stages: (i) incubation, (ii) nucleation, and (iii) MSFC propagation. Images courtesy of Northrop Grumman Corporation.

governed growth of a previously nucleated crack [82]. When the crack has grown large enough that microstructure no longer governs, *e.g.* when traditional linear elastic fracture mechanics (LEFM) and elastic-plastic fracture mechanics (EPFM) can accurately prognose fatigue crack propagation, the crack is in the microstructurally large fatigue crack (MLFC) phase.

The novel contribution presented to the fatigue community in this paper is a three-dimensional, geometrically and mechanistically explicit approach to finite element modeling of statistically accurate microstructures with multiple propagating MSFC's. MSFC locations and propagation rates are computed by the length-scale-appropriate fatigue mechanisms and their stochasticity results from the randomly generated, heterogeneous microstructures. These highly detailed MSFC models are intended to be combined with a statistical, multiscale fatigue simulation framework that determines which microstructure models to simulate to improve stochastic predictions of total component fatigue life [16].

This approach is motivated in part by other simulation approaches extensively documented in the literature. Although a complete review of this literature cannot be covered completely in this paper, a summary of the most relevant work is given in the following sub-section. This is followed by a description of the proof-test application, and then this section concludes with an overview of the MSFC modeling framework detailed in subsequent sections.

2.1.1 Background

Explicit MSFC finite element modeling is divided into three main steps: geometry model generation, finite element meshing, and MSFC simulation. Therefore,

Section 2.2 and Section 2.3 of this paper and this background study are organized according to these three steps.

2.1.1.1 Geometry model generation

The geometry model generation stage is focused on both, or sometimes one, of two main goals: digitally representing observed microstructure and creating a topological representation that can be meshed to a high enough quality for the desired level of simulation accuracy. To achieve these goals, four general types of geometry models are created: experimental replication models, synthetic representation models, statistical realization models, and digital database models.

Experimental replication modelers are focused on creating a highly accurate digital representation of one set of experimental observations, with these observations commonly being in the form of serial scans. Several methods have been developed for converting experimental observations into topological representations. For highly heterogeneous and complex microstructural morphologies, where representing the heterogeneities is much more important than representing surface morphology, modelers often focus the experimental replication method accordingly. For example, when second-phase particle locations significantly influence the spatial distributions of strain concentrations and/or MSFC origins, but the exact shapes of these particles are both complex and negligibly influential on the simulation, modelers have reduced the representation of the particles to ellipses (in two dimensions) or ellipsoids (in three dimensions) [24, 47]. However, material modelers are frequently less fortunate, because decreased morphological resolution of some or all microstructural features can come at the cost of decreased simulation fidelity.

Therefore, the most common experimental replication approaches are focused on reconstructing, as accurately as possible, the observed morphology, and, if necessary, smoothing the topology to eliminate imaging and/or reconstruction artifacts that can reduce both the physical accuracy of the model and mesh quality. For instance, Ghosh *et al.* [23] and Bhandari *et al.* [5] convert combined focused ion beam (FIB) and scanning electron microscope (SEM) data into highly accurate, three-dimensional, polycrystalline microstructure models using techniques common to computer aided design (CAD). For similar purposes, another approach is to convert serial sections to grain and phase boundary surface triangulations through grid construction followed by the multiple material marching tetrahedra algorithm [56]; however, subsequent adaptation algorithms are then required to eliminate stair-stepping and poor quality triangles along surfaces [15, 53]. Additional approaches for digital replication of multiple material serial scan data include Delaunay tetrahedral discretization [6], isosurface construction from irregular grids [72], and decimation of a fine grid into an equivalent, lower resolution topology by edge and surface smoothing [38]. Experimental replication techniques have advanced greatly, but the extensive experimentation required for such techniques diminishes their desirability for some material modelers, such as the authors of this paper, who are interested in representing many realizations of an inherently random microstructure.

At the opposite extremes in physical fidelity and mass simulation feasibility are *synthetic representation models*. Since simplified geometries commonly result in fewer and better quality finite elements to represent phase and grain boundaries than their more realistic counterparts, the former are frequently used in parametric studies of microstructural heterogeneity influences on MSFC's. For example, Bennett and McDowell [3] generated a two-dimensional, staggered layout of rectangular

grains to study grain size and orientation influences on stationary surface cracks in single-phase polycrystals. Simonovski *et al.* [75] and Simonovski and Cizelj [74] generated a finite element mesh of a two-dimensional, Voronoi tessellation with approximately equi-axed, polygonal grain shapes to study grain orientation and crack size influences on crack tip displacements. Similarly, Kunkler *et al.* [37] generated a two-dimensional Voronoi tessellation, where they then used the boundary element method with hybrid crack and sensor elements to simulate MSFC propagation in multi-phase microstructures. In three dimensions, Voronoi tessellations have also been applied to create qualitatively similar grain shapes to observed equi-axed grain structures [1, 4, 54].

Other synthetic representation models are classified here as simplified baseline models. In such models, one or a few grains, possibly with an included second-phase constituent, are represented by a simplified geometry to study the highly localized influences of microstructure on a crack that is significantly smaller than the baseline model dimensions. Either the crack is assumed to be small enough that morphologies at interfaces are assumed to have negligible influence on fatigue behavior or the morphological influences on an MSFC are not the concentration of the study. Examples of such baseline model studies are as follows. In two dimensions, Potirniche and Daniewicz [60]and Potirniche *et al.* [61] studied the deformation behavior through two baseline models: a crack inside a single grain and a crack in a bicrystal, crossing the bi-material interface. In three dimensions, Johnston *et al.* [34] modeled an MSFC inside a single crystal (grain) to study grain orientation influence in typical AA7075-T651 grains, and Wang *et al.* [84] studied the same material with simplified bi-crystal and two-phase baseline models to study the behavior of a MSFC as it propagates across a grain boundary and towards a hard constituent particle, respectively. In baseline model studies for

the MSFC propagation metrics implemented herein, Bozek *et al.* [7] and Hochhalter *et al.* [31] used a model of a semi-ellipsoidal particle inside a cubic grain to study the effects of various microstructural heterogeneities on particle cracking and through-particle propagation across the particle-grain interface, and Veilleux *et al.* [82] used a semi-circular MSFC propagating from a semi-ellipsoidal particle inside hexahedral grains to study microstructural heterogeneity influences on the early stages of MSFC propagation. Other researchers have used simplified baseline models to study particle-matrix debonding [73] and three-dimensional strain localization behavior [19].

Unfortunately, synthetic representation models have their obvious limitations. They only give high fidelity results when the crack is much smaller than the microstructural heterogeneities, or when the local morphology of heterogeneities is determined to influence minimally MSFC propagation. However, if the heterogeneities are of enough significance to be modeled in the first place, then it seems logical to assume that the morphology of these heterogeneities will also be of significance. For instance, sharp corners along material interfaces will create much higher stresses than smoothed corners. Even if the researcher assumes morphology is insignificant, the accurate morphologies often need to be modeled at least once to prove this assumption.

A third type of microstructure geometry model, categorized here as *statistical realization models*, is needed when: (a) more accurate geometry/morphology is deemed necessary for high fidelity MSFC simulation; and, (b) the material microstructure is too random to be modeled via one or a few experimental replication models. Since these are primary needs for the geometry models in this study, statistical realization models are utilized for this study and presented herein. The

general procedure for generating statistical realization models is as follows.

1. Record statistical microstructure data from experimental observations.
2. Sample statistics to generate a spatial realization, and manipulate this realization, as necessary, to best fit statistical distributions and any cross-correlations of interdependent microstructural features.
3. If necessary, convert the spatial realization to a representation that can be modeled via finite elements. Synthetic representations are often required to qualitatively match morphological information not represented by the statistical descriptions. Smoothing routines are also commonplace here to remove numerical artifacts of the synthetic representation routine and/or to improve finite element mesh quality.

If all necessary statistical descriptions are recorded to represent accurately all morphological features of a microstructure, and if the spatial realization generation routine was able to model all such morphological features, then the result would be a 100% realistic morphological representation of the observed microstructure. However, this possibly impossible task has not been achieved by statistical realization modelers; therefore, parts of the resulting models are indeed synthetic.

Two prevalent statistical realization modeling codes are Statistically Induced Realistic Instantiations in 3D (*SIRI-3D*) [25–27] and Microstructure Builder (*mbuilder*) [8, 9, 68–71, 76]. *SIRI-3D* takes as input statistical descriptions of grain volume, grain spatial orientation, texture orientations and misorientations, number of neighbors to a grain, sizes of the neighbors to a grain, grain aspect ratios, and surface area to volume ratios. *SIRI-3D* then samples grain size, spatial orientation, and aspect ratios to generate a realization of ellipsoids. These ellip-

soids are subsequently rearranged to best match the grain neighbor distributions. An equivalent, synthetic, volume-filling realization model is generated by a three-dimensional Voronoi tessellation, where the Voronoi cells are combined to best match the realization of ellipsoids.

The *mbuilder* software has algorithms similar to those in *SIRI-3D*, as well as other algorithms for representing grain growth, recrystallization, and multiple material phases. The single-phase statistical representation routine, as described by Saylor *et al.* [71], takes as input three-dimensional statistical descriptions of grain sizes, aspect ratios, orientations, and misorientations, then performs a four step procedure: (1) random generation of overlapping ellipsoids that match the input grain size and aspect ratio statistics; (2) selection and replacement of ellipsoids via 'simulated annealing' [62] to simultaneously minimize overlap and maximize spatial coverage of ellipsoids; (3) space-filling representation of the ellipsoid packing by choosing ellipsoid centroids as nucleation sites in a grid and applying grain growth algorithms to fill the grid in a manner that best matches the ellipsoid packing; and, (4) assignment of grain textures to best match the orientation and misorientation distributions. The grid used by Saylor *et al.* was regular, *i.e.* a hexahedral domain filled with constant-sized voxels, but an irregularly sized and shaped grid, *i.e.* a three-dimensional Voronoi tessellation, was subsequently added to create a qualitatively more realistic representation of grain boundaries for some materials' microstructures [8]. These same techniques have been extended for representing dual-phase materials [70] and recrystallization via Monte-Carlo simulations [9, 69]. Additionally, Rollett *et al.* [68] developed algorithms for generating statistically realistic second-phase particles, which can then be inserted into a first-phase model. Second-phase particle generation required additional considerations for matching pair correlation functions of particle neighbor distances, because, unlike the grains,

particles are not volume filling.

Due to its ability to represent both grains and particles, *mbuilder* is used in this study to generate statistical realization models of AA7075-T651 microstructure. The material statistics and algorithms used for this study are presented in Section 2.2.

Regardless of model type, a common requirement is to be able to create and simulate a sufficiently large microstructural region for the purposes of the study. In many studies, a representative volume element (RVE) is required. Hill [30] originally defined an RVE as a sample of a heterogeneous material large enough that: (a) the average behavior is the same as the whole material (the macroscale behavior); and, (b) slight perturbations in the boundary conditions do not significantly change the physical response. Subsequently, Swaminathan and Ghosh [79] defined a statistically equivalent RVE (SERVE) as one that meets the requirements of an RVE as well as the additional requirement that distributions of the modeled heterogeneities match the statistical distributions for that material. In a follow-up study, Swaminathan and Ghosh [78] determined that the SERVE size increases significantly as damage accumulates inside the models. Bazant and Pang [2] theorized that engineering structures requiring extremely low probability of failure should be modeled at the microstructure scale in a manner that guarantees the microstructural heterogeneities contributing to the fewest cycles to failure are considered. Since such configurations of heterogeneities are often an exceptional occurrence, with typically 10^{-6} or 10^{-7} probability, it is computationally intractable to generate a large enough RVE from statistical data that is guaranteed to have at least one of these configurations. Since extreme behavior is of interest in this study, the modeling approach is not focused on generating an RVE, but rather on

generating a microstructure model large enough to model the entire MSFC phase inside a microstructure with a pre-determined selection of the heterogeneities necessary to grow that crack at the fastest rate. A significant challenge thus lies in pre-determining such heterogeneities. Meeting this challenge, however, is not the objective of the work presented in this paper; rather, the objective is to develop a MSFC modeling framework within which one can generate these heterogeneities and perform high fidelity simulations. Subsequent studies will be required to develop a technique for determining the microstructure models with which this high-fidelity MSFC propagation simulation framework will be utilized to improve fidelity of the minimum life tail of a fatigue life distribution.

The fourth and final type of microstructure geometry model is categorized here as a *digital database model*. If the material heterogeneity is not too random, and the experimentalist is able to record all randomness in serial scans, then all permutations of the microstructural heterogeneity can be converted to digital models and stored in a database for subsequent simulations. For example, Mao *et al.* [47] combined digital database modeling with synthetic representation modeling by first recording the exact shapes of many observed second-phase particle clusters, and then creating models by randomly sampling the observed shapes and approximating the shapes as ellipsoids. However, the inherent randomness of material heterogeneity in most microstructures eliminates feasibility of digital database modeling approaches when modelers, such as the authors of this paper, are interested in accurately simulating stochastic material behavior.

2.1.1.2 Finite element meshing

Finite element meshing is a generally expansive topic in the literature, and still expansive even when narrowed to its usage for polycrystalline microstructure modeling. Therefore, only a highlight of the approaches closely related to this study is given here.

One meshing technique is to generate a volume mesh that is directly a result of the microstructure geometry representation algorithm(s). Groeber *et al.* [27] used the parts of the Voronoi cells representing the grain geometries to construct a tetrahedral mesh: tetrahedron corners are generated from the Voronoi cell vertices and the Voronoi cell centroid and tetrahedron edges are generated by connecting these corners. Ghosh *et al.* [24] created a mesh of Voronoi finite elements to analyze a second-phase microstructure by using the centroids of individual constituent particles as Voronoi cell centroids. A limitation of these two approaches is that the mesh is defined directly by the geometry. To alleviate this limitation, Boltcheva *et al.* [6] implemented a routine that refines, as necessary for finite element modeling purposes, the density of the Delaunay tetrahedral mesh they use to represent the microstructure geometry. However, this is still coupling the geometry resolution and mesh resolution, even though there is no physical constraint suggesting the geometry has to be at the same resolution as the mesh.

One method for circumventing this problem is never to represent explicitly the geometry, but have the mesh conform as best as possible to an implicitly defined geometry. For example, Bernacki *et al.* [4] used level set functions to enforce mesh refinement near the cell boundaries of an implicitly defined, three-dimensional Voronoi tessellation. Resk *et al.* [64] augmented this approach by introducing automatic remeshing and material state mapping of the aforementioned meshes to

maintain satisfactory element qualities when modeling large deformations. However, these meshing techniques do not guarantee that the meshes conform to the boundaries of the implicit geometry; the boundary is estimated by the nearest element boundaries. Thus, again, the resolution of the geometry directly depends upon the mesh resolution. Alternatively, Wang [83] developed an algorithm that generates surface meshes, which conform to the interior and exterior surfaces of implicit geometries. However, all methods for generating meshes of implicit geometries require that the geometries can be represented by analytical formulas. This can be difficult, if not impossible, if the modeler is interested in accurately representing complex microstructural geometries.

A third technique alleviates the aforementioned problems by treating the geometry model as a higher level, explicit representation, which is to be discretized by the finite element mesh; the mesh elements are as dense or more dense than the geometry elements, the mesh conforms to the geometry, and the mesh can be refined, as necessary, for representing fields without changing the geometry. For multiple material models, Zhang *et al.* [93] developed an octree based routine for generating unstructured triangular and quadrilateral meshes in two-dimensions, and tetrahedral and hexahedral meshes in three dimensions. Particular focus of the algorithms is on conformal representation of the geometries at material interfaces. Qian *et al.* [63] augmented the hexahedral meshing routines by using pillowing, geometric flow, and optimization algorithms to improve element quality at material interfaces. The research presented herein again augments the meshing routines of Zhang *et al.* to create high quality triangular surface meshes, which conform to material interfaces and model boundaries, and from which the advancing front tetrahedral meshing techniques of Cavalcante-Neto *et al.* [12,55] are used to generate a volume mesh. This procedure, detailed in Section 2.2, allows for high

fidelity numerical representation of the complex geometries and computed fields in a heterogeneous microstructure with propagating MSFC's. The geometry model is adapted only to represent accurately geometrical features (microstructure and cracks), while the mesh is adapted to represent accurately both the geometries and the computed fields.

2.1.1.3 Microstructurally small fatigue crack simulation

Similar to the microstructure geometry, an MSFC itself can be modeled implicitly or explicitly. Implicit modeling incorporates MSFC behavior through probabilistic formulae, finite element enrichment, softening in the constitutive behavior, phenomenological models, and/or semi-empirical formulae. Tryon and Cruse [80, 81] developed a probabilistic fatigue life model that incorporates variability in fatigue crack formation due to microstructural variability. Therein, the number of cycles to form a fatigue crack is predicted by a phenomenological formula for nucleation and propagation through a single grain, in a single-slip dominated mode. Randomness results from variations in grain size, resolved shear stress, and shear strength. Many other phenomena contributing to variation in MSFC propagation rates, such as multiple material phases, elongated grain sizes, multi-directional slip, latent slip system hardening, grain boundaries, and MSFC propagation beyond one grain, are not considered in this probabilistic approach. Laz and Hillberry [41] also developed a probabilistic fatigue life model where variability results from microstructural variability; however, in their study the variable microstructural feature was second-phase particle size. For the material they studied, aluminum alloy 2024-T3, they found that cracks originated from particles, and by simultaneously assuming that all particles are cracked and that the surrounding microstructure has constant fatigue strength, they determined that variation in particle size leads to the

observed variation in fatigue life. However, Laz and Hillberry did not include additional variations due to grain orientations, grain boundary misorientations, grain sizes, slip system hardening, *etc.* Liao [44] also developed probabilistic models for fatigue crack origination at particles in an aluminum alloy, 2024-T351. Their probabilistic model predicts whether a particle will crack based on the particle size, grain size, and surrounding grain orientation. Similarly, Bozek *et al.* [7] developed a micromechanism-based probabilistic approach to predicting particle cracking in aluminum alloy 7075-T651, wherein particle radii, particle aspect ratio, particle fracture toughness, maximum tensile strain, and surrounding grain orientation were the independent parameters. Such particle cracking models can be used by explicit MSFC modelers to determine where MSFC's originate inside a microstructure model. For example, Section 2.3.2 details how the model by Bozek *et al.* is used in this study.

Alternatively, McDowell *et al.* [51] and Xue *et al.* [88] assumed a crack already originated at a particle or pore, then formulated semi-empirical relationships to model three sequential crack growth stages: growth through the notch-root influence region of the particle/pore, subsequent MSFC growth until microstructure influence becomes negligible, and MLFC growth to failure. The first stage considers the amplified cyclic plastic shear strain caused by the particle/pore, the second stage considers grain size, grain orientation, stress amplitude, and plastic shear strain amplitude, and the third stage considers the effective stress intensity factor amplitude through the traditional Paris model [57]. However, Xue *et al.* concluded more information of MSFC behavior with respect to grain size and orientation is required to calibrate microstructural parameters within the second stage. Hopefully, one outcome of the study presented in this paper is a high fidelity simulation environment for informing and improving these highly efficient, geometrically im-

plicit MSFC models. Although finite element enrichment and constitutive model softening (smeared cracking) approaches are not reviewed here, the simulation environment described herein is intended to improve the formulations within such approaches as well.

For reviews of explicit MSFC modeling approaches, the reader is referred to Bozek *et al.* [7], Hochhalter *et al.* [31, 32], and Veilleux *et al.* [82]. The explicit MSFC simulation approaches developed in those four papers are employed in this study, as detailed in Section 2.3.

Altogether, this review of prior research in microstructure geometry modeling, finite element meshing, and MSFC simulation reveals that all three steps have been developed to varying levels of fidelity, dependent on the requirements of the modeling approaches. However, high fidelity geometry modeling, meshing, and MSFC simulation strategies have not been combined for statistically accurate, geometrically explicit, and physically justified simulation of MSFC evolution; such a combination is the novel contribution intended by the research presented in this paper.

2.1.2 Observations of proof-test application

Figure 2.2 shows common axis labels of AA7075-T651 as well as the simulated loading conditions, which are representative of the highest strains at a notch root of a double edge-notched (DEN) specimen. The microstructural material and loading conditions have been significantly detailed in recent literature, *e.g.* [7, 11, 31, 32, 59, 76, 82], so only a brief summary is given here. As a result of the rolling process, the grains are elongated significantly in the RD, and to a lesser

degreee in the TD. The material processing also causes stringers of second-phase constituent particles aligned most noticeably along the RD. The loading conditions are representative of those experienced in a highly stressed region, *e.g.* a borehole of a bolted airframe component experiencing high-cycle fatigue. The modeled microstructure lies completely within the notch root influence region of the borehole. The average strain fields within this microstructure were determined from a component scale elastic-plastic finite element simulation [59]. The microstructure strain is constant amplitude, constrained axial tension in the RD, with a maximum strain, ϵ_{max}, of approximately 1% and a load ratio, $R = \epsilon_{min}/\epsilon_{max}$, of approximately 0.1. All exterior surfaces of the microstructure model are constrained from out-of-plane displacement, except for the strain loading surface and the traction-free surface illustrated in Figure 2.2. The traction-free surface is coincident with the borehole surface. These loading conditions result in far-field plasticity surrounding the microstructure.

Second-phase constituents of various chemical compositions exist in AA7075-T651, but only one is of significance for this modeling application. The two most prevalent particle compositions are Al_7Cu_2Fe and Mg_2Si, which are commonly referred as 'iron-bearing' and 'silicon-bearing', respectively. Both particle types are observed to cause fatigue crack incubation [59], where through-cracking of the particle is the incubation mechanism for iron-bearing particles and particle-matrix debonding is the incubation mechanism for silicon-bearing particles. However, observations have also shown that further MSFC evolution does not occur from, and is negligibly influenced by, particle-matrix debond sites [59, 86]. These same observations showed that all cracks experiencing MSFC evolution subsequent to incubation had started from the iron-bearing particles. Thus, only the iron-bearing particles are modeled here, and, consequently, all further usage of the term 'parti-

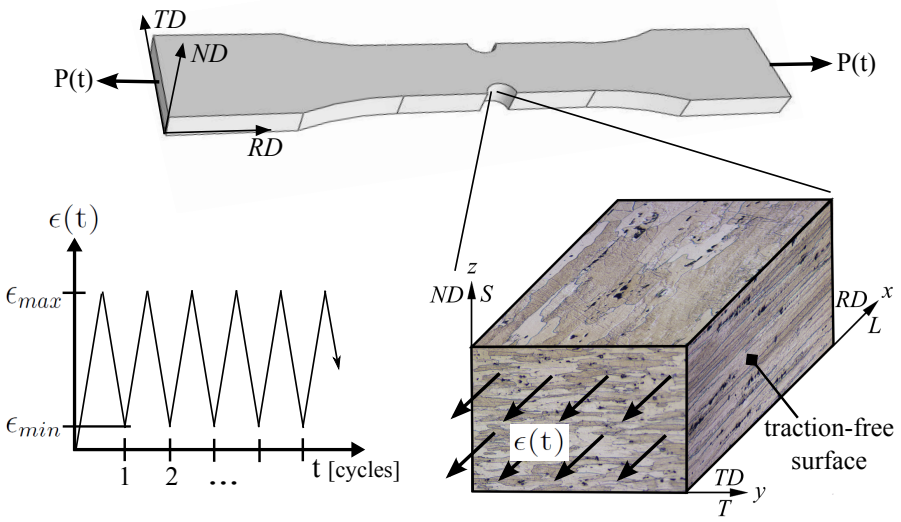

Figure 2.2: Illustration of a double edge-notched specimen from [59] with a magnified view of the notch-root region simulated at the microstructural length scale. The magnified region is shown with scanning electron microscopy images and nomenclature of the orthogonal planes and axes in AA7075-T651 microstructure, from [11]. Etching was performed to delineate grain boundaries. The simulated constant amplitude cyclic loading conditions, representative of the notch root strain, are also illustrated.

cle' refers to these iron-bearing, Al_7Cu_2Fe particles. These particles are the white regions in Figure 2.1(a), which is a microscale image of a DEN borehole surface, and an example of a particle that cracks is in Figure 2.1(b).

The grain and particle material properties elucidate the process of fatigue crack incubation simulated by Bozek *et al.* [7] and summarized further in Section 2.3.1. The grains are face-centered cubic (FCC) crystal plastic with an average RD elastic modulus of 72 GPa and the particles are isotropic, elastic with an average elastic modulus of 166 GPa, *i.e.* over twice the modulus of the surrounding grains. Furthermore, the particles are brittle with an approximate mode-I fracture toughness of 0.5 MPa$\sqrt{\text{m}}$. Observation of particles under load prior to incubation show no particle-grain debonding [59]. Therefore, load transfer is maximized at the particle-

grain interfaces, and stresses concentrate inside particles due to their high stiffness relative to the grains. Consequently, particles that incubate a fatigue crack are assumed to contain a sufficiently large inherent flaw such that the high driving forces and low fracture toughness will cause the flaw to propagate unstably until it reaches the particle-grain interface [7].

The two MSFC stages following incubation, nucleation and MSFC propagation, are also strongly influenced by microstructural heterogeneity. This conclusion is inferred by observations, *e.g.* Figure 2.1(c), which clearly show that MSFC propagation direction is influenced by grain texture. Time series micrographs over thousands of cycles infer that MSFC propagation rate is also microstructure dependent [59]. Studies by Hochhalter *et al.* [31,32] and Veilleux *et al.* [82] elucidate that field metrics related to MSFC nucleation and propagation are dependent on multiple microstructural heterogeneities. The results of these studies are further summarized in Section 2.3.2 and Section 2.3.3.

The significant influence of microstructural heterogeneities on MSFC evolution negates the validity of traditional linear elastic fracture mechanics (LEFM) and elastic-plastic fracture mechanics (EPFM) approaches. Thus, the following approach has been adopted to consider explicitly microstructural heterogeneity and the mechanisms of MSFC incubation, nucleation, and propagation.

2.1.3 Modeling framework

The modeling framework detailed in this paper follows the three main steps in Figure 2.3:

EXPERIMENTAL OBSERVATION Record statistical descriptions of microstructural heterogeneities and locations and rates of crack evolution from experimental observations.

REALIZATION MODEL GENERATION Generate and volume mesh geometrically explicit models that are realizations of the statistics recorded from observations.

MICROSCALE FATIGUE ANALYSIS Within the realization models, perform geometrically explicit microstucturally small fatigue analyses with cracks incubating, nucleating, and propagating by the experimentally validated criteria for each stage. Output high fidelity predictions of the number of load cycles consumed by the MSFC phase, N_{MSFC}.

Section 2.2 details the experimental observation and realization model generation techniques, and then Section 2.3 details the microscale fatigue analysis techniques. A proof-of-concept is then given in Section 2.4, where analysis results are presented for the incubation and nucleation stages of MSFC propagation simulated in a typical AA7075-T651 realization model. The computational requirements for these analyses are also given, and, based on these results, the advantages and drawbacks of the approach are critically evaluated in Section 2.5. Specifically, conclusions are made as to whether high fidelity, stochastic predictions of MSFC growth rates can be formulated through this framework, and, if so, how many repetitions can be performed to get these predictions.

2.2 Finite element model generation and adaptation

The geometry modeling approach detailed here is in the category of *statistical realization modeling*. The process of generating and adapting a statistical realization

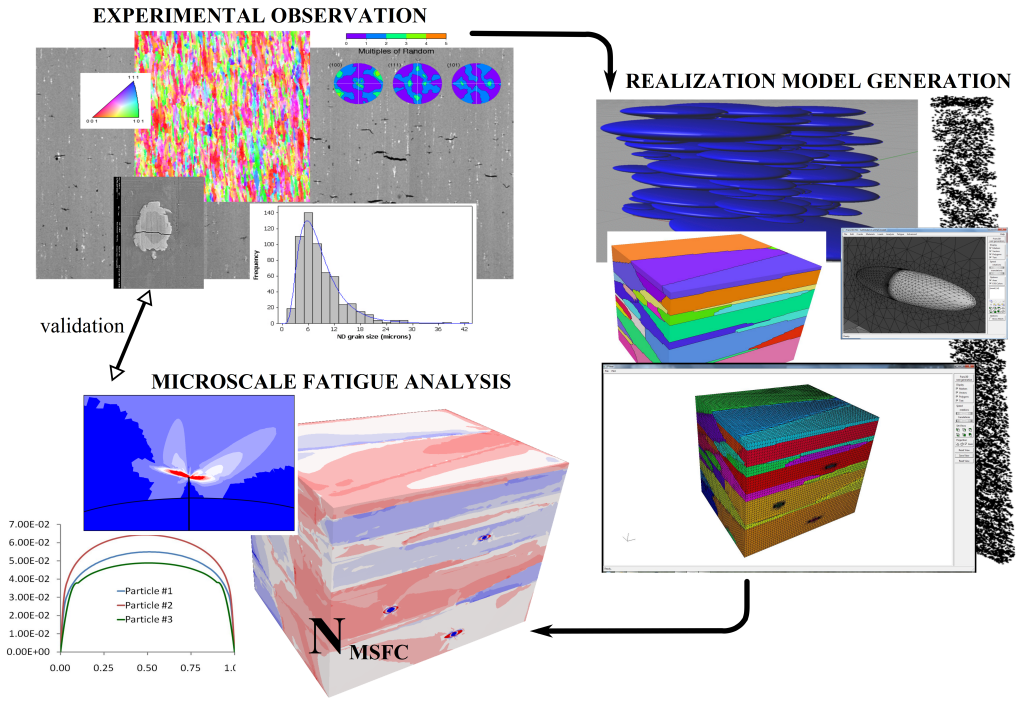

Figure 2.3: Illustration of the three main steps of the realization modeling framework.

geometry model with geometrically explicit MSFC's is divided into nine steps:

1. Record first-phase statistics from observations of grain shapes and textures.
2. Record second-phase statistics from observations of Al_7Cu_2Fe particle shapes and locations.
3. Generate a statistically accurate realization model of first-phase geometries and textures.
4. Surface mesh the first-phase model.
5. Volume mesh the first-phase model.
6. Generate a statistically accurate realization model of second-phase geometries and locations, and filter out all particles not of interest for the modeling application.

7. Surface mesh the second-phase model.
8. Adapt the first-phase model: insert particles and cracks, and propagate cracks.
9. Map material state data when geometry and mesh adaptations are performed for crack propagation during a simulation.

The following nine sections sequentially detail these nine steps for the proof-test application.

2.2.1 First-phase statistics*

Grain data are recorded from observations to statistically describe the sizes, shapes, and textures of the first-phase. Grain size and shape distributions are obtained from electron backscatter diffraction (EBSD) data on orthogonal sections. Due to the large grain sizes in the LT (RD-TD) plane, grain size and shape data are not recorded in this plane. Instead, grain sizes and shapes are recorded from the TS (TD-ND) and LS (RD-ND) planes. The grain boundary network is generated from EBSD images by image recognition software that delineates grain boundaries and image editing software that repairs the images. In this study, a 15° misorientation angle is chosen to delineate grain boundaries. The grain boundary network images are then read into software that converts all grains to ellipses and records the dimensions of all ellipses larger than a specified size, which is 5 μm^2 for this study. For the proof-test example to follow, a total of 1056 ellipses (grains)

*Stephen D. Sintay, the intended second author of the paper presented in this chapter, originally wrote contents of this section in his Ph.D. Dissertation for Carnegie Mellon University, which is referenced herein as [76]. However, modifications are made from the writing in [76] to best suit the context of this paper. As copyright holder, Sintay has granted, by written permission, use of his writing, and the modifications thereof, in this section. The written permission was submitted to Cornell University with this Dissertation.

have been recorded in the TS plane and 583 ellipses have been recorded in the LS plane.

The diameters and aspect ratios of these ellipses are then fit to distributions to statistically describe grain size and shape, respectively. Histograms of the diameters and aspect ratios, and their best-fit distributions, are shown in Figure 2.4. The RD, TD, and ND diameters and RD:ND aspect ratio data are fit to a three parameter lognormal distribution,

$$f(x) = \frac{\exp\{-(\ln[(x-\gamma)/\beta])^2/(2\alpha^2)\}}{(x-\gamma)\alpha\sqrt{2\pi}}, x \geq \gamma; \alpha, \beta > 0, \tag{2.1}$$

where α, β, and γ are the shape, scale, and threshold parameters, respectively. The TD:ND aspect ratio data are fit to a three parameter gamma distribution,

$$f(x) = \frac{((x-\gamma)/\beta)^{\alpha-1}\exp\{-(x-\gamma)/\beta\}}{\beta\Gamma(\alpha)}, x \geq \gamma; \alpha, \beta > 0, \tag{2.2}$$

where α, β, and γ are again the shape, scale, and threshold parameters, respectively. Table 2.1 is a list of the α, β, and γ parameters for all five grain diameter and aspect ratio distributions. Due to the significant elongation of grains in the RD, most grains intersected the boundaries of the EBSD scans in the RD; therefore, the RD grain size data shown here are falsely skewed to smaller sizes. However, this negligibly influences the modeling process for two reasons: (a) the finite element model RD dimensions are typically shorter than the grain RD dimensions recorded here so the modeled grains get cut off in the RD; and, (b) as illustrated in Figure 2.2, the RD is the primary loading axis, and consequently, the plane of crack propagation is approximately normal to the RD; therefore, accurately modeling grain sizes in the TD and ND is much more important than accurately modeling grain sizes in the RD.

First-phase texture distributions are obtained from a combination of X-ray observations and the same EBSD observations as above. The X-ray data come

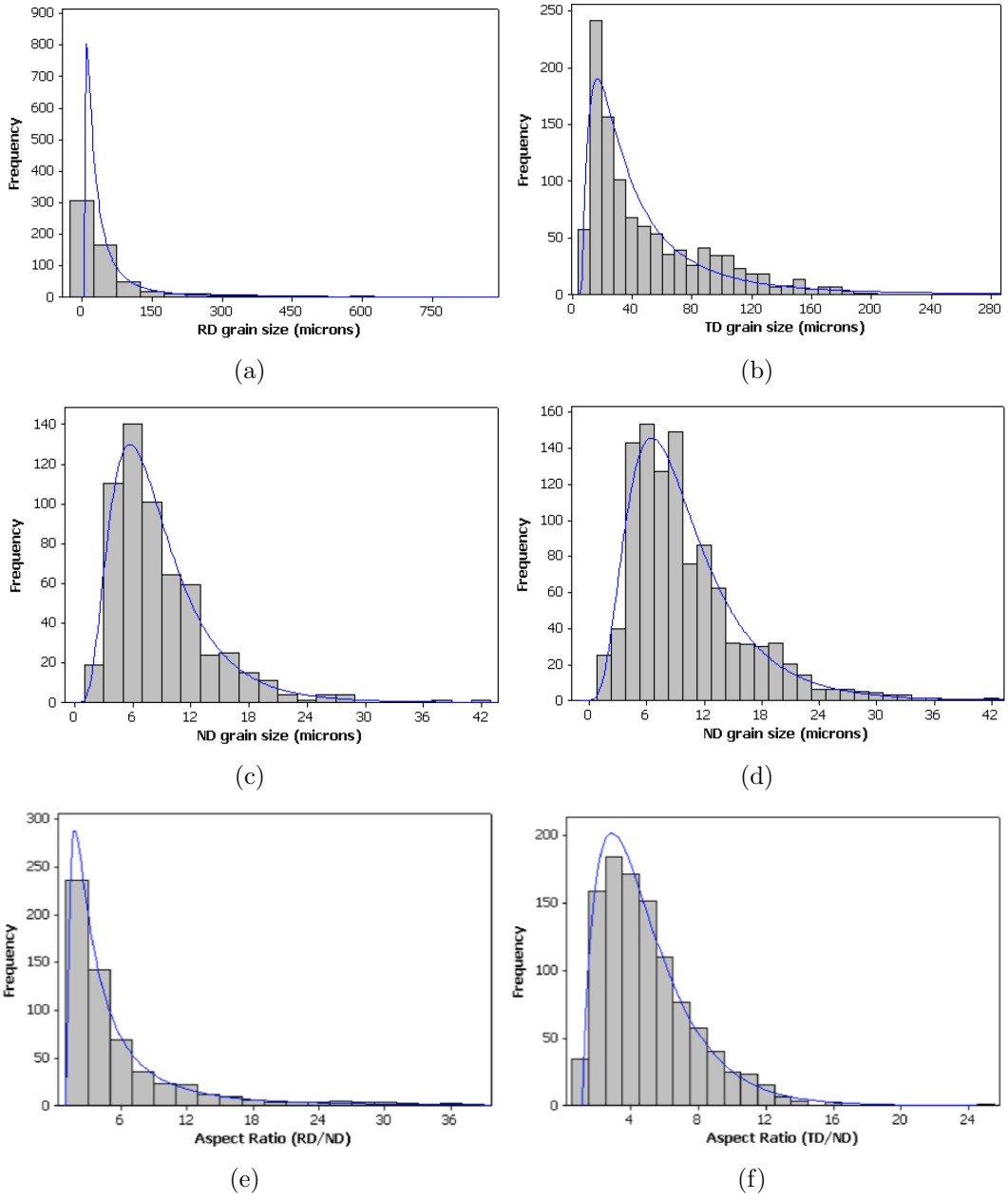

Figure 2.4: Grain size and shape histograms and distributions of AA7075-T651, from [76]. (a) RD diameter; (c) ND diameter from LS plane; (d) ND diameter from TS plane; (e) RD:ND aspect ratio; and, (f) TD:ND aspect ratio.

Table 2.1: Grain size and shape distribution parameters for the distributions shown in Figure 2.4, derived from data in [76].

			Parameters		
Grain Feature	Figure	Distribution	α	β	γ
RD diameter	Figure 2.4(a)	lognormal	3.21	1.20	4.24
TD diameter	Figure 2.4(b)	lognormal	3.38	0.96	5.09
ND diameter (LS)	Figure 2.4(c)	lognormal	2.05	0.53	-0.17
ND diameter (LT)	Figure 2.4(d)	lognormal	2.28	0.51	-0.99
RD:ND aspect ratio	Figure 2.4(e)	lognormal	0.99	1.11	1.00
TD:ND aspect ratio	Figure 2.4(f)	gamma	1.87	2.04	1.10

from a different material sample than the EBSD data, but both samples are from similar regions of the rolled product. Pole figures of the EBSD and X-ray data are shown in Figure 2.5(a) and Figure 2.6, respectively. The scales of these contour plots are in multiples of a random distribution, and the maximum intensities of the two plots, approximately 2.8 and 2.5, respectively, indicate there is no strong preference to any texture. However, the EBSD misorientation distribution with a cutoff at 15°, Figure 2.5(b), shows preference to low angle grain boundaries as a result of the rolling process for this material. All microstructural texture data is stored in a dataset, which is sampled at random to generate a list of grain textures for a statistical realization model.

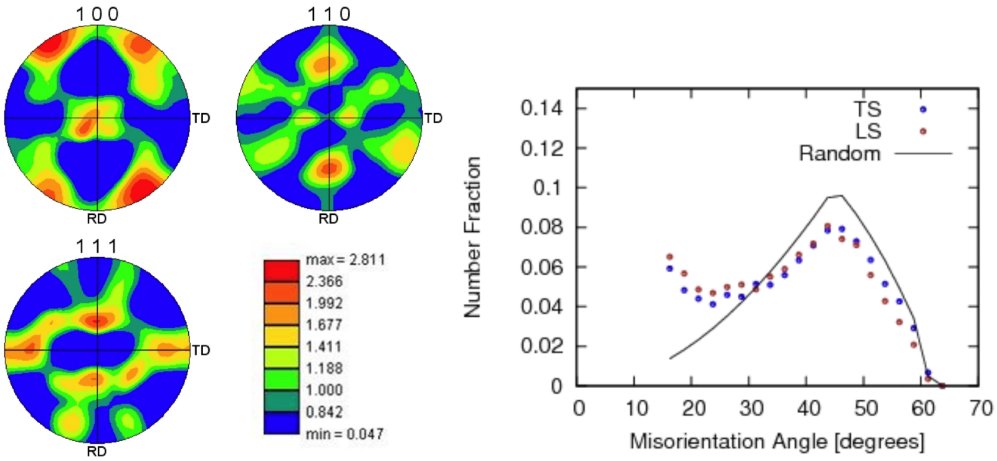

(a) (b)

Figure 2.5: EBSD grain texture data of AA7075-T651, from [76]. (a) Pole figure contour plots of the combined EBSD data from the LS and TS planes. (b) Misorientation angles of the EBSD data from the two planes, with a random distribution shown for comparison.

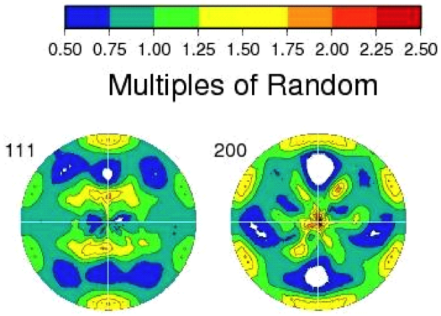

Figure 2.6: Pole figure contour plots of AA7075-T651 grains from X-ray diffraction, from [76].

2.2.2 Second-phase statistics*

Particle size, shape, and location statistics for AA7075-T651 were recorded by Harlow *et al.* [29], Campman [11], and Rollett *et al.* [68]. The reader is referred

*Stephen D. Sintay, the intended second author of the paper presented in this chapter, originally wrote contents of this section in his Ph.D. Dissertation for Carnegie Mellon University, which is referenced herein as [76]. However, modifications are made from the writing in [76] to best suit the context of this paper. As copyright holder, Sintay has granted, by written permission, use of his writing, and the modifications thereof, in this section. The written permission was submitted to Cornell University with this Dissertation.

to those studies for detailed summaries of the observations, methodologies, and recorded statistics of second-phase particles. The findings of those studies are summarized here in the context of this study.

Particle sizes were characterized by Harlow *et al.* [29] as surface areas in the LS, LT, and TS planes, and maximum dimensions in the RD, TD, and ND. The surface area data were fit to a truncated Weibull cumulative distribution function (CDF),

$$F(x) = 1 - \exp\left\{-[(x/\beta)^{\alpha} - (x_p/\beta)^{\alpha}]\right\}, x \geq x_p, \tag{2.3}$$

where α, β, and x_p are the shape, scale, and truncation parameters, respectively. The maximum dimension data were fit to a three-parameter Weibull CDF,

$$F(x) = 1 - \exp\left\{-[(x-\gamma)/\beta]^{\alpha}\right\}, x \geq \gamma, \tag{2.4}$$

where α, β, and γ are the shape, scale, and threshold parameters, respectively. The parameters for best-fits in each observation plane are listed in Table 2.2.

Since the particles are elastic and brittle, their textures are not of interest. However, particles are not space filling and their positions are correlated highly in the RD, and to a lesser degree in the TD, due to stringer formation. To characterize appropriately the correlated nearest neighbor distances, Rollett *et al.* [68] used pair correlation functions (PCF's),

$$f(x,y) = \sum_{i=1}^{n} \frac{P_i(x,y)}{N_i(x,y)}, \tag{2.5}$$

where n is the total number of particles, (x,y) is the two-dimensional location relative to the i^{th} particle centered at the origin, $P_{x,y}$ is the number of particles at (x,y), and $N_{x,y}$ is the number of pixels within the boundaries of an observation at (x,y). The pair correlation functions recorded for particles observed in the

Table 2.2: Particle size and shape distribution parameters, derived from data in [29].

			Parameters			
Particle Feature	Plane	Distribution	α	β	γ	x_p
RD-ND area	LS	truncated Weibull	0.46	5.69	—	10.0
RD-TD area	LT	truncated Weibull	0.33	2.61	—	10.0
TD-ND area	TS	truncated Weibull	0.54	7.46	—	10.0
RD length	LS	3-parameter Weibull	1.13	9.43	4.21	—
ND length	LS	3-parameter Weibull	1.30	3.88	1.87	—
RD:ND aspect ratio	LS	3-parameter Weibull	1.41	1.62	0.99	—
RD length	LT	3-parameter Weibull	0.96	9.78	4.21	—
TD length	LT	3-parameter Weibull	1.13	5.45	1.95	—
RD:TD aspect ratio	LT	3-parameter Weibull	1.20	1.01	1.01	—
TD length	TS	3-parameter Weibull	1.25	6.58	4.21	—
ND length	TS	3-parameter Weibull	1.80	4.76	1.30	—
TD:ND aspect ratio	TS	3-parameter Weibull	1.36	0.96	0.99	—

LS, TS, and LT planes are utilized, in combination with the grain size and shape distributions, to generate particle realizations in this study.

2.2.3 First-phase statistical realization model*

The grain geometry realization models generated here are voxel-based structures and *mbuilder* is used to generate these structures [8,9,68–71,76]. The reader is directed to these references for detailed descriptions of the *mbuilder* algorithms. Five main steps are followed in *mbuilder* to generate a voxel-based statistical realization geometry model from the AA7075-T651 grain size and shape statistics:

*Stephen D. Sintay, the intended second author of the paper presented in this chapter, originally wrote contents of this section in his Ph.D. Dissertation for Carnegie Mellon University, which is referenced herein as [76]. However, modifications are made from the writing in [76] to best suit the context of this paper. As copyright holder, Sintay has granted, by written permission, use of his writing, and the modifications thereof, in this section. The written permission was submitted to Cornell University with this Dissertation.

1. Generate a set of ellipsoids that fit the input statistics.
2. Pack the ellipsoids into the specified volume of the microstructure model.
3. Choose and move a subset of these ellipsoids to maximize volume coverage and minimize overlap among neighbors.
4. Create a volume filling microstructure model by subdividing the microstructure model into voxels and applying grain growth algorithms to combine voxels in a manner that best represents the ellipsoids.
5. Use Monte Carlo grain growth algorithms to relax the microstructure and allow the grain boundaries to become more natural.

A statistically representative volume element (RVE) generated by this process is shown in Figure 2.7. In Figure 2.8, the probability and cumulative distributions of the RVE data for this 4893 grain model and a much smaller 211 grain model are compared with the input observation data from Section 2.2.1. For both RVE models, the TD and ND grain data match the observation data well. However, in the RD, RVE data do not match the observation data, because, as previously stated, the observation data were inaccurate in this dimension. To get more elongated RD grain sizes than the recorded observation data, the RVE RD dimensions were assigned by using a fixed RD:ND aspect ratio of 12:1. By the arguments given in Section 2.2.1, these artificially produced RD dimensions are likely to be inconsequential in MSFC simulations. A 2 μm voxel size was determined to be sufficiently small to represent accurately the ND and TD dimensions and to produce synthetically grain surface morphologies that are qualitatively similar to observations, *e.g.* Figure 2.2.

Large RVE models, such as the 4893 grain RVE in Figure 2.7, are too large for MSFC simulations; therefore, these RVE's are instead utilized as digital database

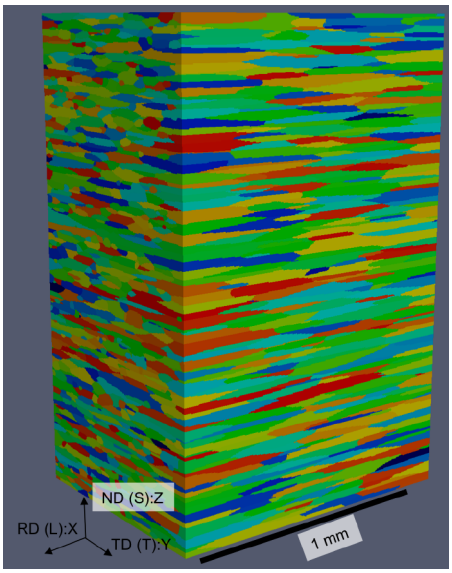

Figure 2.7: Statistically representative volume element of first-phase microstructure geometries with 4893 grains represented by voxels at 2 μm per voxel, from [76].

models from which smaller models are randomly selected and cropped for MSFC simulation. These cropped models are likely not RVE's of geometrical and texture distributions, but by the arguments given in Section 2.1.1, RVE's are unnecessary for the MSFC simulation framework herein. Four cropped models are shown in Figure 2.9. Each of these is a 120 μm cube with approximately 75 grains. Although the grain textures are not shown here, *mbuilder* algorithms are also utilized for assigning textures to an RVE or a cropped model by simultaneously matching the orientation and misorientation distribution functions. The following section details how these cropped, voxel-based models are converted into high quality, multiple material surface meshes.

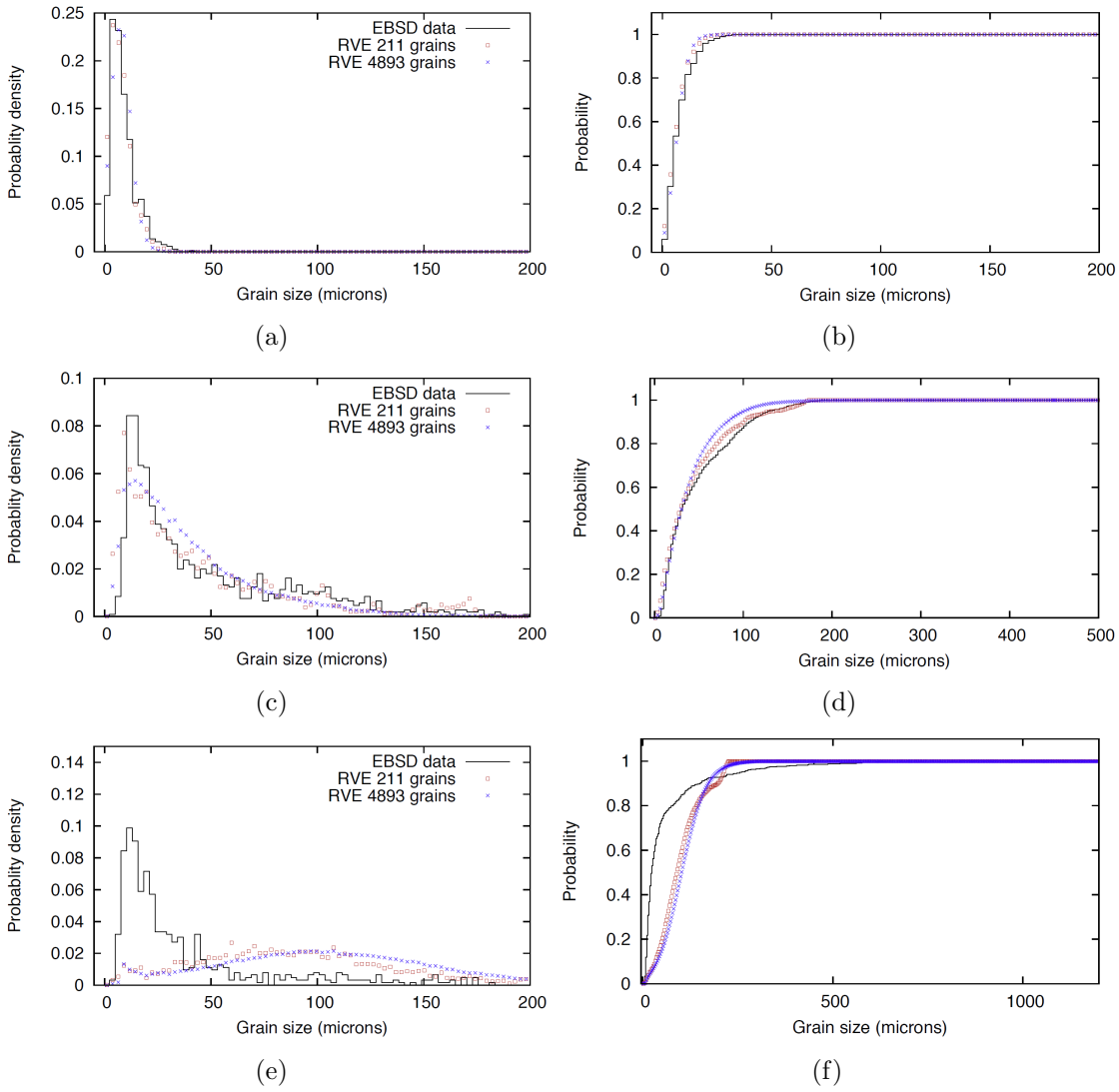

Figure 2.8: Comparison of grain size distributions from RVE's and observations, from [76]. (a) ND diameter probability distributions; (b) ND diameter cumulative distributions; (c) TD diameter probability distributions; (d) TD diameter cumulative distributions; (e) RD diameter probability distributions; and, (f) RD diameter cumulative distributions.

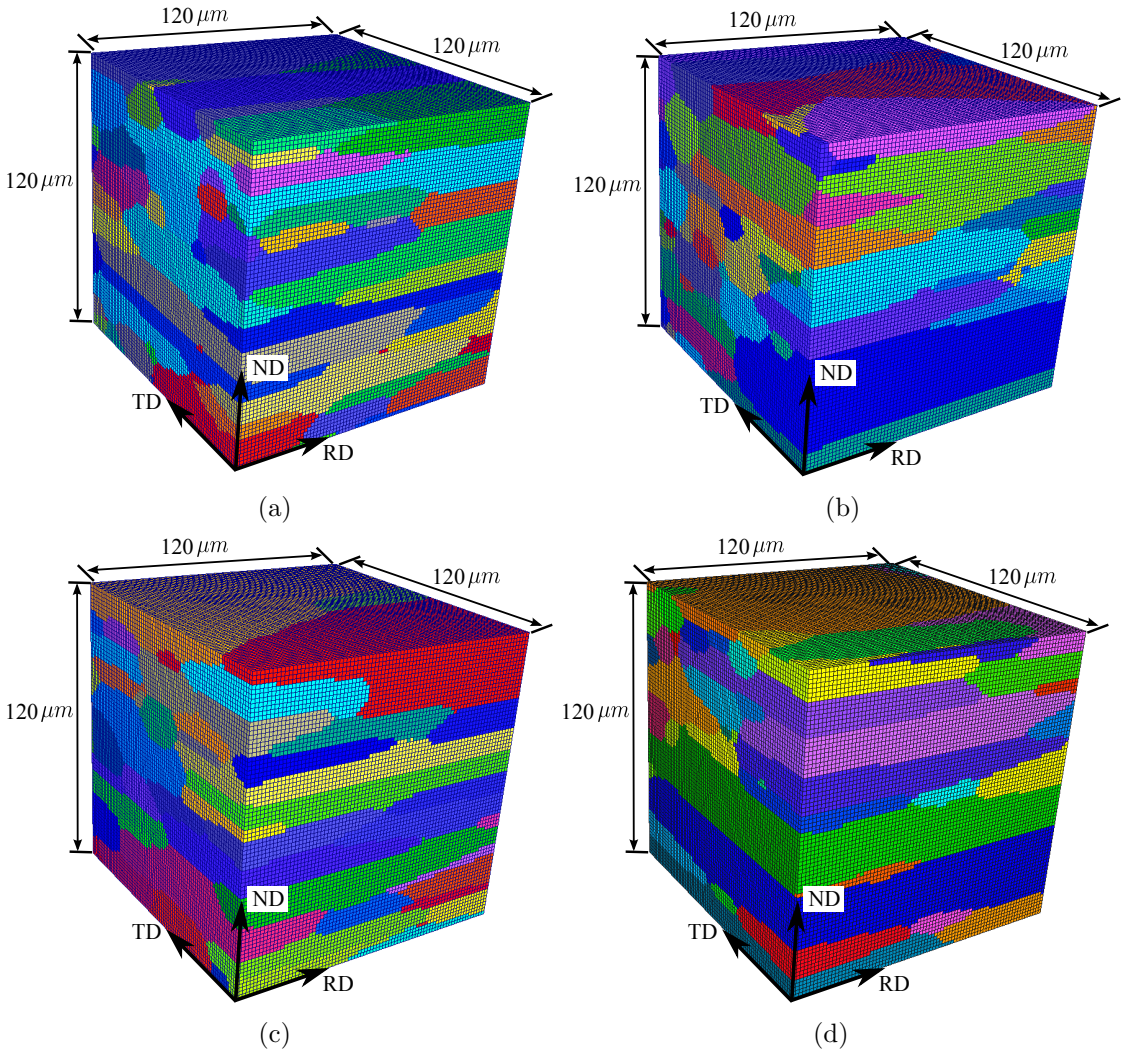

Figure 2.9: Cropped statistical realization geometry models from the RVE in Figure 2.7. (a) Crop 1; (b) Crop 2; (c) Crop 3; and (d) Crop 4. All four crops are 120 μm cubes with 2 μm voxels.

2.2.4 First-phase surface mesh*

The statistical realization geometry models, Figure 2.9, are provided as a voxelized scalar field, V, which is represented in the form of sampled function values

*Yongjie Zhang and Jun Ma, intended third and fourth authors, respectively, of the paper presented in this chapter, wrote the previously unpublished and uncopyrighted contents of this section. Zhang and Ma have granted, by written permission, use of their writing in this section. The written permission was submitted to Cornell University with this Dissertation.

on rectilinear grids, $V = F(i, j, k)$ where i, j, and k are indices of x, y, and z coordinates in the grid. At each grid point, the attached function value is the grain index, indicating which grain contains the grid point. Starting from V directly, an octree-based isocontouring approach [90, 91, 93] is utilized to detect automatically all boundaries and mesh the domain with multiple grains simultaneously, with the constraints of conformal meshes along boundaries and high quality mesh adaptation. This octree-based approach provides a robust framework to construct automatically and efficiently high-fidelity triangular meshes directly from voxelized digital data. For each octree cell, if it is intersected by the boundary surface, then a minimizer point is calculated within this cell by minimizing a pre-defined quadratic error function (QEF),

$$QEF(x) = \sum_i (n_i(x - p_i))^2, \tag{2.6}$$

where p_i and n_i represent the position vector and unit normal vector, respectively, of an intersection point. Only one minimizer point is calculated for each cell, and each octree cell has a unique index. This property allows one to index uniquely the minimizer point of octree cells without introducing any duplicates. In this method, a 'material change edge' is defined as an edge with two end points lying within two different grains. Each material change edge in the meshed domain is analyzed to construct triangular surface meshes. If a uniform mesh is to be generated, each material change edge is shared by four cells, and one minimizer point is calculated for each of these four cells to construct a quadrilateral element. Alternatively, if an adaptive mesh is to be generated, one material change edge is shared by either four cells or three cells, and a hybrid mesh is generated, including both quadrilateral and triangular elements. The quadrilateral elements are later split into triangles. In either method, the resulting triangles form the non-manifold boundaries of all grains, and the density of the surface mesh can be output as the necessary size for

finite element analysis.

Mesh quality is of particular focus here because this is a very important factor influencing the convergence and stability of the finite element solvers, especially for crystal plasticity material models. In the generated surface meshes, most elements have good aspect ratios, but the rare poor quality elements can cause finite element solver issues; therefore, mesh quality needs to be improved to guarantee good aspect ratios throughout. The surface element quality index utilized here is the ratio of the inscribed circle radius to the circumscribed circle radius. A geometric flow smoothing technique [92, 94], based on geometric partial differential equations (GPDE's), is used to improve mesh quality with feature preservation. All vertices in the mesh are categorized into six groups, and each group is optimized using different methods to improve the element quality indices of the mesh while preserving all boundary features [63]. The following are the six groups and methods:

GROUP 1 The eight corners of the model - fixed during the improvement to keep the model boundary.

GROUP 2 Vertices on the 12 edges of the model - can only move along the edge. This group has two sub-categories: vertices inside one grain - smoothed only along the edge; and, vertices shared by two or more grains - fixed during improvement.

GROUP 3 Vertices on the 6 faces of the model - can only move in the plane of the face. This group has three sub-categories: vertices shared by more than two grains (planar, non-manifold points) - fixed; vertices shared by two grains (planar curve points) - smoothed along the tangent direction of the planar curve; vertices inside one grain - smoothed in plane.

GROUP 4 Vertices located on the grain boundary surface patches between two grains - smoothed on the tangent plane of the grain boundary.

GROUP 5 Vertices located on interior curves - smoothed only along the tangent direction of the interior curve.

GROUP 6 Non-manifold vertices shared by more than two interior curves - fixed.

While the eight corner nodes and non-manifold points are fixed, and vertices on the model planes and edges are moved only on the respective planes and edges, the planar boundary curves and interior spatial curves are distinguished from their respective vertices and regularized using B-spline interpolation and resampling, and boundary surfaces are smoothed using geometric flows [92,94]. As a relaxation-based method, geometric flows or GPDE's have been extensively utilized in surface smoothing and mesh quality improvement. A discretized format of the Laplacian-Beltrami (LB) operator over triangular meshes has been derived and utilized to solve GPDE's numerically. Generally, the GPDE's are defined as

$$\frac{\delta x}{\delta t} = V_n(k_1, k_2, x)n(x) + v(x)T(x), \tag{2.7}$$

where $V_n n$ is the curvature normal, $v(x)$ is the velocity in the tangent direction $T(x)$. When V_n is defined in different ways, different geometric flows are obtained, such as mean curvature flow, average mean curvature flow, surface diffusion flow, and high order flows. Each GPDE has its own properties, and it is necessary to utilize these properties for various applications. Here, the average mean curvature flow is chosen due to its volume preserving property.

Figure 2.10 shows a triangular surface mesh before and after quality improvement, Figure 2.10(a) and Figure 2.10(b), respectively. The following section details how unstructured tetrahedral meshes are generated from these volume meshes.

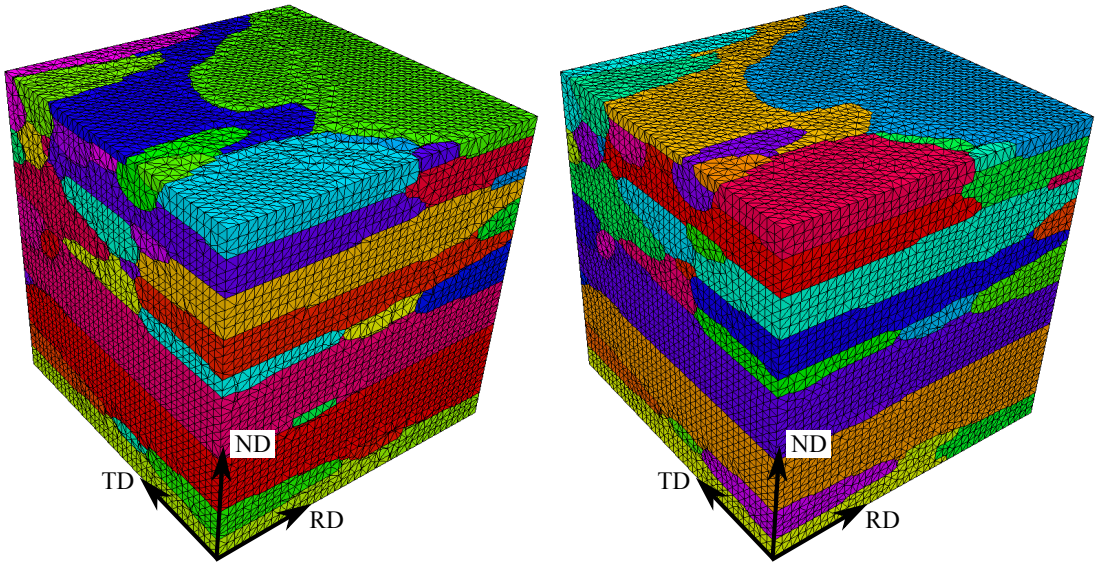

(a) (b)

Figure 2.10: Triangular surface meshes of a first-phase geometry realization model: (a) Before mesh improvement; and, (b) after mesh improvement. Mesh size is 53,838 triangular elements, and minimum element aspect ratio improves from 0.0562 before smoothing to 0.0716 after smoothing.

2.2.5 First-phase volume mesh

The three-dimensional volume meshing procedures from Cavalcante-Neto *et al.* [12, 55] are utilized to generate volume meshes from the surface meshes of the multiple-material first-phase models. These procedures are divided into three main steps: octree generation, advancing front volume meshing, and local mesh improvement. The octree generation step provides a non-uniform grid from which element sizes are determined during the advancing front routine. For each grain, an initial octree is constructed around the grain. Then, the octree is locally refined to the element sizes of the grain boundary surface mesh. The entire octree is then refined, as necessary, to the largest cell size on the grain boundary; this guarantees volume elements inside a grain will be no larger than surface elements on the

grain boundary. Finally, the octree is refined again such that all cells are no more than double the size of their neighboring cells. Subsequently, the advancing front volume meshing procedure begins from the front defined by the grain boundary surface mesh. The grain boundary element facets remain unchanged during the meshing procedure to maintain a conforming mesh with the grain boundary geometry and neighboring grain meshes. The front advances inward by generating tetrahedra that conform to the local element sizes defined by the octree cell sizes. A back-tracking procedure is utilized to improve mesh quality, as necessary, when sides of the front converge. After an initial volume mesh is generated, local mesh improvement is performed via smoothing routines and additional back-tracking.

Figure 2.11 is an element quality histogram for the volume mesh generated from the surface meshed model in Figure 2.10(b). This mesh has approximately 325,000 tetrahedral elements. The element quality metric shown here is the tetrahedron condition number from Freitag and Knupp [21], $3/K_w(A_n)$, where

$$K_w(A_n) = |A_n W^{-1}||(A_n W^{-1})^{-1}|, \tag{2.8}$$

$$A_n = (-1)^n [e_{n+1,n} \quad e_{n+2,n} \quad e_{n+3,n}], \tag{2.9}$$

and where W is the Jacobian of the linear transformation from the reference configuration to the ideal (equilateral) configuration of a tetrahedron, and $e_{i,j}$ is the edge vector from vertex i to vertex j. This tetrahedron condition number is always greater than 0 and no larger than 1, where values approaching 0 are slivers and 1 is ideal. A study of mesh quality needed for finite element solver convergence, with the crystal plasticity model utilized in this study, found that elements with $3/K_w(A_n) \geq 0.025$ resulted in convergence. The volume meshes generated for the realization models in this study always have $3/K_w(A_n) > 0.05$.

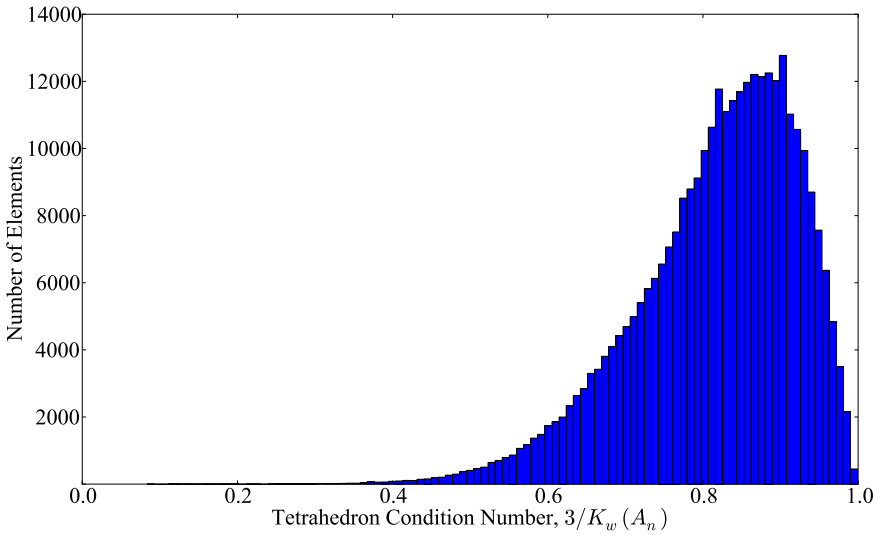

Figure 2.11: Element quality histogram of a tetrahedral mesh generated from the surface meshed first-phase realization model in Figure 2.10(b). The minimum element quality is 0.0834.

2.2.6 Second-phase statistical realization model

Particle geometries are generated, surface meshed, and inserted into the microstructure models after the first-phase has been volume meshed. The first step in the particle modeling process is to generate a realization of particle locations, shapes, and sizes. However, for the proof-test conditions simulated here, Figure 2.2, particle cracking is mostly confined to the highly stressed, traction-free surface of the notch root [87], and only approximately 5% of the particles on this surface are observed to crack under load [28, 59]. The surface where particle cracking occurs is referred herein as the 'traction-free surface'; this is the RD-ND face with minimum TD coordinates in the microstructure models. Since all uncracked particles are assumed to influence negligibly MSFC propagation [7] and particle size is much smaller than grain size, it is highly desirable to eliminate all uncracked particles prior to finite element simulation. With this as the goal, three methods have been

implemented to generate a statistically representative set of cracked particles.

Method #1 generates a particle realization within a domain with the same dimensions as the first-phase realization model, and then removes all particles predicted not to crack. The process for doing so is:

1. Use *mbuilder* to generate a realization of ellipsoids that match the particle shape, size, and location statistics from Section 2.2.2. Ellipsoids are generated inside a region sufficiently larger than the first-phase realization model to obtain a statistically realistic set of particles intersecting the traction-free surface of the model.
2. Remove all particles not intersecting the traction-free surface.
3. For every remaining particle, determine the orientation(s) of the grain(s) located at that particle in the first-phase realization model.
4. Determine the maximum principal strain in the neighborhood of the particle. This can either be approximated as the maximum strain applied on the model, ϵ_{max} from Figure 2.2, or computed through finite element simulation of the first-phase realization model and sampling the strains in the grain(s) located at the particle. Since the finite element simulations are strain-controlled, it is likely reasonable and more computationally efficient to assume the applied strain on the model, ϵ_{max}, is the maximum strain in the neighborhood of the particle; this eliminates the need for finite element simulation prior to particle insertion.
5. Input the particle dimensions, surrounding grain orientation(s), and maximum strain into the AA7075-T651 particle cracking filtering procedure from Bozek *et al.* [7]. This procedure is summarized in Section 2.3.1. The output is then the subset of surface particles predicted to crack.

6. Place only the particles predicted to crack into the microstructure model. Cracks are either placed into the model at this time or at the appropriate strain in the finite element analysis when particle cracking occurs.

Method #2 generates a particle realization much larger than the dimensions of the first-phase realization model, and then randomly selects a subregion of these particles. The motivation for this method over the first method is that the larger particle realization, *e.g.* Figure 2.12, only has to be generated once for generation of multiple two-phase microstructure models. Randomness among the two-phase microstructure models is introduced by changing the orientations and geometries of the grains and the selected subregions of the particle realization. The process for this method is:

1. Use *mbuilder* to generate a realization of ellipsoids that best match the particle shape, size, and location statistics from Section 2.2.2. Ellipsoids are generated inside a region much larger than the first-phase realization; for example, compare dimensions in Figure 2.12 and Figure 2.9.
2. Randomly place a slicing plane with the same dimensions as the traction-free surface of the first-phase realization model into the particle realization and select all particles intersecting this plane.
3. Follow steps 3 through 6 of Method #1.

Method #3 allows the user to choose manually the dimensions and locations of one or a few particles to model, with the constraint that these particles are predicted to crack. Combined observations of particle density on LS surfaces [29] and frequencies of particle cracking on these surfaces [28, 59] indicate that an average of between two and three particles will crack on the traction-free surface

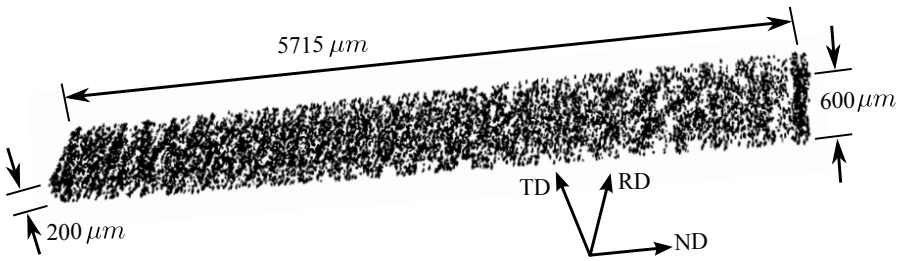

Figure 2.12: A 10,000 Al_7Cu_2Fe particle realization generated from the particle size, shape, and location statistics in Section 2.2.2

of a 120 μm cubic microstructure model. Therefore, manually defining and placing a few particles predicted to crack by the filtering procedure in [7] is reasonable. However, the statistical distributions of particle sizes, shapes, and locations, and grain orientations should be utilized to determine whether the manually generated set of particles predicted to crack is statistically reasonable.

2.2.7 Second-phase surface mesh

For all three methods of generating realizations of particles predicted to crack, the particle geometries and surface meshes are represented as follows. Since the particles are on the surface and their statistical descriptions are ellipsoids, each particle is geometrically defined as a semi-ellipsoid,

$$\frac{(x-x_0)^2}{a^2}+\frac{(y-y_0)^2}{b^2}+\frac{(z-z_0)^2}{c^2}=1, y \geq y_0, \tag{2.10}$$

where a, b, and c are the RD, TD, and ND radii, respectively, of the ellipsoid chosen from the statistical realization, x_0 and z_0 are the RD and ND position coordinates of the particle centroid in the statistical realization, and y_0 is the TD coordinate of the microstructure model surface where the particles are being placed (the traction-free surface). An inherent assertion here is that the centroids of all particles chosen from the statistical realization lie on this surface of the model,

when in reality the centroids of the particles chosen by one of the three methods in Section 2.2.6 can lie above or below the model surface, as long as some portion of the particle intersects this surface. Since particle RD and ND dimensions in the statistical data, Table 2.2, were measured from a RD-ND (LS) surface, these dimensions are used on the model surface for all particles. This is achieved by moving the ellipsoid centroids to the model surface. If necessary, this approach can easily be adapted to model alternative surface particle sizes and shapes.

The process for generating an explicit surface particle geometry is illustrated in two-dimensions in Figure 2.13 by steps (i), (ii), and (iii). In step (i), the particle shape is defined implicitly by Equation 2.10 with centroid, C=(x_0, y_0, z_0). Next, in step (ii), the particle is explicitly represented by vertices placed at the extrema coordinates of the semi-ellipse and edges connecting these vertices. Then, in step (iii), this discrete representation of the ellipse is refined by splitting edges approximating the curved surface of the ellipse into two equal-sized segments and moving the newly created vertices to the ellipse surface. The new vertices are translated by finding the ray that points from the ellipse centroid to the new vertex, and then moving the vertex to the intersection of the ray and the ellipse. Step (iii) is repeated as many times as necessary for geometrical accuracy. Extension of this procedure to three dimensions results in a triangulation as the discretization of the semi-ellipsoid's curved surface, Figure 2.14(a). At the end of this process, the flat surface of the semi-ellipsoid is an n-dimensional polygon. To convert the ellipsoid geometry to a surface mesh, this n-dimensional polygon is surface meshed by the two-dimensional versions of the advancing front meshing routines from Cavalcante-Neto *et al.* [12, 55]. An example of the resulting surface mesh of this polygon is shown in Figure 2.14(b). Since the other surfaces of the ellipsoid are already triangles, these can be used as surface elements, or, if necessary, these triangular faces

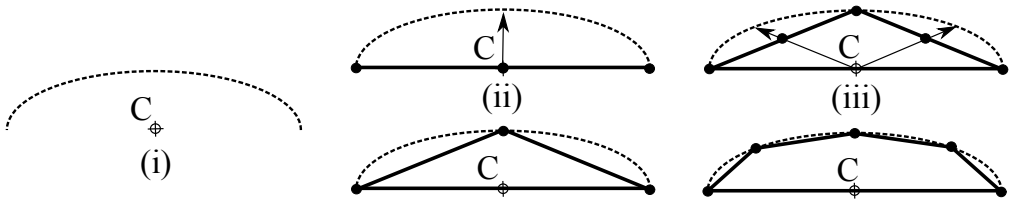

Figure 2.13: Two-dimensional illustration of the particle geometry generation procedure. The process in (iii), subdividing edges and moving to the ellipse surface, is repeated as many times as desired for geometrical accuracy.

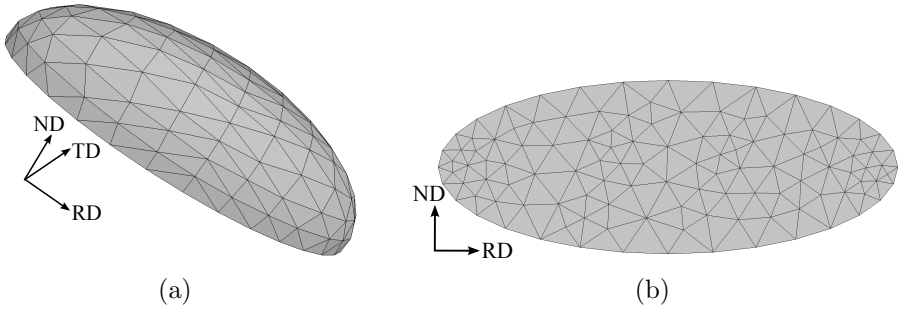

Figure 2.14: Triangular surface mesh of a typical surface particle geometry: (a) discretization of the curved surface of the semi-ellipsoid; and, (b) discretization of the flat surface of the semi-ellipsoid.

can be discretized further by the two-dimensional advancing front algorithms.

The particle geometry chosen here is the simplest morphological representation of the recorded particle statistics, and obviously an idealization of the actual particle surface morphologies, *e.g.* Figure 2.1(b). It could be argued that qualitatively more accurate morphologies should be included through synthetic representations, because the simplifications made by a semi-ellipsoid skew simulation results by missing the stress concentrations caused by irregular shapes on the particle-grain interfaces. However, local stress concentrations are likely decreased by the highly local plastic strain deformation they induce [22]. Therefore, irregular particle morphology is concluded to have little influence on particle cracking driving forces [7]. Conversely, localized plastic strain deformations can significantly influence nu-

cleation [31, 32]. However, synthetic representations of irregular particle surface morphologies can also skew simulation results, likely more than semi-ellipsoidal particle representations. Furthermore, semi-ellipsoidal geometries require a significantly less dense mesh than irregular geometries. Thus, until accurate particle surface roughness can be statistically classified and geometrically represented, semi-ellipsoidal particle geometries are modeled.

2.2.8 Microstructure geometry and mesh adaptation for particle and fatigue crack representation

After the particle surface meshes are generated, they must be placed into the microstructure finite element model. Also, as cracks are predicted to incubate, nucleate, and propagate through the microstructure, this model must be adapted accordingly. Since the number of finite element nodes, n, is typically $O(10^6)$ to $O(10^7)$ in the model, geometry and mesh adaptations for particle/crack insertion and crack propagation, which commonly require $O(n^2)$ algorithms, are computationally expensive. However, a very small percentage of the nodes in the microstructure model change during particle and crack adaptations, because the particle and crack sizes are typically much smaller than the finite element model. Therefore, a subvolume adaptation routine is implemented here, Figure 2.15, that allows for geometry adaptation algorithms to be performed only on a subset of nodes and elements from the microstructure finite element model. This routine follows four main steps:

STEP 1 *Subvolume extraction, Figure 2.15(a)*: given as input the microstructure finite element model and a bounding box defining the dimensions of a sub-

volume region, the subvolume is extracted by the following three steps:

1. The subvolume domain, Ω_s, is identified as all finite elements inside and crossing the bounding box.
2. The microstructure finite element model domain, Ω, is divided into two volume domains, Ω_s and $\Omega' = \Omega - \Omega \cap \Omega_s$.
3. All element surface facets and nodes on the boundary, Γ'_s, between Ω_s and Ω' are marked as unadaptable to maintain mesh conformity between Ω_s and Ω'.

STEP 2a *Particle inclusion, Figure 2.15(b)*: given as input Ω_s, Γ'_s, and the location and surface mesh of a surface particle, this particle is added to the subvolume via the following four sub-steps:

1. Elements of Ω_s in the neighborhood of the particle and not containing Γ'_s are deleted. An adequately sized element deletion region is chosen automatically for a smooth transition in mesh size from the particle to the surrounding grain mesh. The surface elements on the subvolume face containing the particle are converted into a polygon.
2. The particle is placed in the middle of this polygon, and the updated polygon (with a hole) is surface meshed.
3. The region where elements were deleted around the particle is volume meshed.
4. The particle is volume meshed.

All surface and volume meshing follows the routines from Cavalcante-Neto *et al.* [12, 55]. These steps assume the particle is embedded completely within a grain, so the particle must be moved slightly if it originally lies on a grain

boundary. However, if it is deemed necessary for accurate fatigue simulations to model particles on grain boundaries, then these routines can be augmented accordingly. If a particle does not need to be inserted into the subvolume, *i.e.* only crack adaptation needs to be performed, then **STEP 2a** is skipped during the submodel adaptation process.

STEP 2b *Crack adaptation, Figure 2.15(c)*: given as input Ω_s, Γ'_s, the crack front coordinates, and the regions to contain the crack (*e.g.* the particle), the 'fracture analysis code, next generation' (*FRANC3D/NG*) [85] is utilized to insert or propagate the crack. For a case when a crack needs to terminate exactly at a material interface, *e.g.* through-particle cracking as shown in Figure 2.16, *FRANC3D/NG* trims the crack along the interfaces between the crack-containing regions and the neighboring regions. Additionally, *FRANC3D/NG* is capable of representing arbitrarily non-planar fatigue crack propagation and variable propagation rates along the crack front. These tools are necessary for modeling accurately three-dimensional fatigue crack propagation in a heterogeneous microstructure. *FRANC3D/NG* also maintains all element facets and nodes on retained boundaries, *e.g.* Γ'_s, during crack adaptation and remeshing. If a crack does not need to be adapted in the subvolume, *i.e.* only particle insertion needs to be performed, then **STEP 2b** is skipped during the subvolume adaptation process.

STEP 3 *Subvolume insertion, Figure 2.15(d)*: given as input Ω_s^{new} (the subvolume after particle insertion and/or crack adaptation), Ω', and Γ'_s, the full finite element model is reassembled as $\Omega^{new} = \Omega' + \Omega_s^{new}$. The resulting mesh is conforming along Γ'_s.

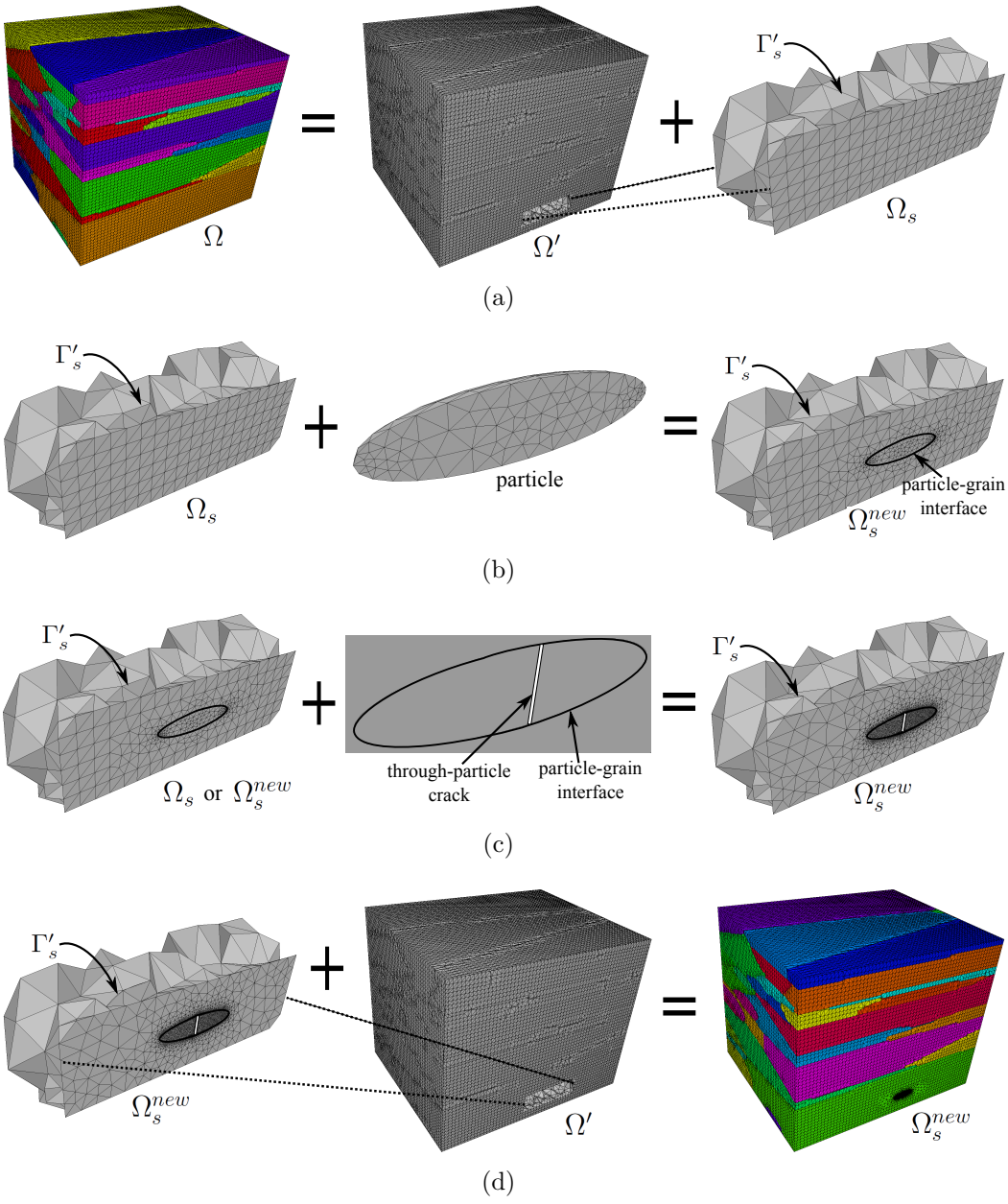

Figure 2.15: Subvolume extraction, adaptation, and insertion routines for local finite element model adaptation upon particle inclusion and/or crack insertion or propagation. (a) **STEP 1**: subvolume extraction; (b) **STEP 2a**: particle inclusion; (c) **STEP 2b**: crack adaptation; and, (d) **STEP 3**: subvolume insertion.

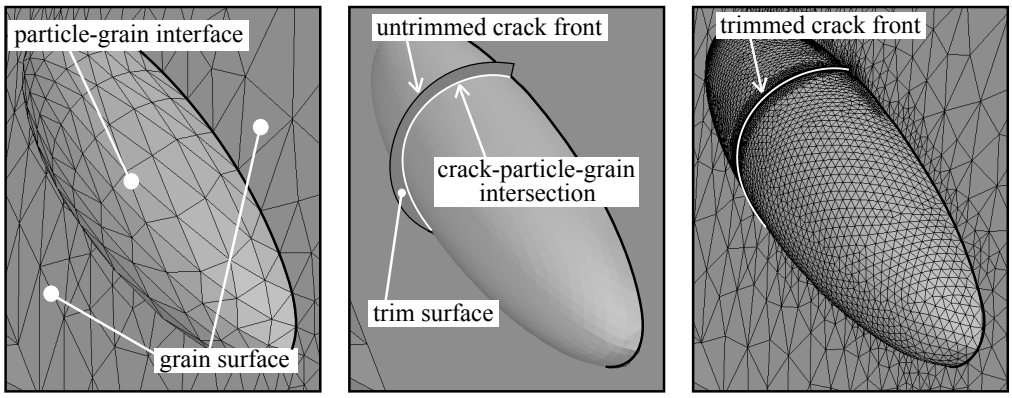

Figure 2.16: Process of crack trimming along a material interface, exemplified by insertion of a through-particle crack: (a) view from inside the grain at the particle-grain interface prior to crack insertion; (b) same view with an inserted crack geometry prior to trimming; and, (c) inserted through-particle crack after trimming along the particle-grain interface and re-meshing. All of the trim surface, *i.e.* the part of the crack in (b) extending into the grain, is trimmed.

2.2.9 Material state mapping

When geometry and mesh adaptations are made during a simulation to represent explicitly MSFC evolution, the history-dependent material state must be mapped from the old mesh to the new mesh. This is achieved by an inverse isoparametric mapping algorithm [33, 45]. This algorithm consists of two high level steps: (1) in the old mesh, mesh n, state variables stored at integration points are extrapolated to nodes using element shape functions; and, (2) displacements and state variables are transferred to either nodes or integration points in the new mesh, mesh $n+1$. The second step involves finding, for each point in mesh $n+1$, the element containing that point in mesh n and the natural coordinates (ξ, η) of that point in the element. This is an inverse problem: the standard isoparametric mapping

formula,

$$X_{n+1} = \sum N_i(\xi, \eta) X_n^i, \tag{2.11}$$

has to be solved for (ξ, η), where X_n^i are the global nodal coordinates of the element in mesh n, X_{n+1} are the global coordinates of the point in mesh $n+1$, and N_i are the nodal shape functions at (ξ, η). Therefore, (ξ, η) are determined by an iterative scheme. Once these natural coordinates are known, nodal displacements and state variables are transferred from mesh n to mesh $n+1$ using the same shape functions,

$$U_{n+1} = \sum N_i(\xi, \eta) U_n^i, \tag{2.12}$$

where U_n^i are nodal values in mesh n of the variable being transferred, and U_{n+1} is the value of the variable at the point in mesh $n+1$. When this mapping algorithm is performed, it is critical that mesh refinement is sufficient for both the old and new mesh in regions of high gradients, *e.g.* near crack fronts. Otherwise, unsatisfactory solution diffusion can occur as a result of extrapolation and interpolation. These effects can be compounded throughout an analysis where many mappings are performed.

Furthermore, specific criteria of the material models in mapped regions should be obeyed. For instance, in the microstructure analyses performed for this study, the implemented crystal plasticity model asserts volume preserving plastic deformation and multiplicative decomposition of the total deformation gradient [48]. Volume preserving plastic deformation is maintained during material state mapping by first performing scalar mappings of the plastic deformation tensor components, then scaling the tensor to re-establish volume preservation,

$$F_p = \frac{F_p^{map}}{(det(F_p^{map}))^{1/3}}, \tag{2.13}$$

where F_p^{map} is the mapped plastic deformation gradient and F_p is the deforma-

tion gradient after scaling. Multiplicative decomposition of the total deformation gradient,

$$F = F_p \cdot F_e, \tag{2.14}$$

where F is the total deformation gradient, F_e is the elastic part, and F_p is the plastic part, is maintained during mapping by only mapping F_p and F_e, and then calculating F from the multiplicative decomposition formula. Again, the meshes must be sufficiently refined to assure these adjustments to the deformation tensors do not significantly alter the deformation states in regions of high field gradients.

2.3 Criteria for microstructurally small fatigue crack stages

Within the geometrically explicit, statistically representative microstructure models, MSFC propagation is simulated via physically justified, microstructure-dependent criteria. Once again, the three MSFC stages, shown in Figure 2.1(c), are incubation, nucleation, and MSFC propagation, and the reader is directed to papers by Bozek *et al.* [7], Hochhalter *et al.* [31, 32], and Veilleux *et al.* [82] for detailed descriptions of the criteria implemented for simulating these three stages in AA7075-T651. The following briefly summarizes these criteria and how they are utilized in this geometrically explicit MSFC simulation framework.

2.3.1 Incubation

Incubation is predicted by the filtering framework from Bozek *et al.* [7]. As described in Section 2.2.6, this filtering framework is utilized to eliminate all parti-

cles predicted not to crack from the microstructure realization model. Specifically, Bozek *et al.* conjecture that linear elastic fracture mechanics (LEFM) criteria are valid due to the brittle nature of particle cracking. Particles are assumed to have an initial flaw, proportional in size to the particle size, that will propagate unstably through the particle if the highest stress in the particle, σ_p, reaches a critical value, the particle strength, σ_{cr}. The resulting formula for σ_{cr} is

$$\sigma_{cr} = \frac{K_{IC}}{\sqrt{\pi C F(a_p, b_p}} \tag{2.15}$$

where K_{IC} is the particle mode I fracture toughness, C is a statistically varying parameter defining the ratio of initial flaw size to particle size, and $F(a_p, b_p)$ is an initial flaw shape parameter dependent on particle size. Experimental studies and simulation studies of replicated experimental observations have focused on determining statistical descriptions of K_{IC} and C for Al_7Cu_2Fe particles. To eliminate the significant computational demand required to compute σ_p in a microstructure finite element model to then compare to σ_{cr}, Bozek *et al.* constructed a particle stress response surface from approximately 1300 finite element analyses of a simplified baseline model. Thus, for a given particle aspect ratio, surrounding grain orientation, and maximum strain level, the response surface is queried to obtain an approximation of σ_p. Only particles for which the queried σ_p is greater than or equal to σ_{cr} are included in the microstructure finite element models in this study.

2.3.2 Nucleation

Nucleation is predicted from the stress and irreversible slip fields immediately ahead of an incubated MSFC. In face-centered cubic crystals, such as AA7075-T651 grains, slip occurs on 12 primary systems. Hochhalter *et al.* [31] implemented

five nonlocal slip-based metrics,

$$D_1 = \max_{\alpha} \gamma^{\alpha}, \tag{2.16}$$

$$D_2 = \max_{p} \gamma^{p}, \tag{2.17}$$

$$D_3 = \gamma = \sum_{\alpha=0}^{N_s} \gamma^{\alpha}, \tag{2.18}$$

$$D_4 = \max_{p} \int_0^t \sum_{\alpha=0}^{N_d} \left| \dot{\gamma}_p^{\alpha} \tau_p^{\alpha} \right| dt, \tag{2.19}$$

$$D_5 = \max_{p} \int_0^t \sum_{\alpha=0}^{N_d} \left| \dot{\gamma}_p^{\alpha} \right| \left(1 + k \frac{\langle \sigma_n^p \rangle}{g_o} \right) dt, \tag{2.20}$$

D_1 is the maximum of the slips, γ^{α}, accumulated on the 12 slip systems, α. D_2 is the maximum of the slips, γ^{p}, accumulated on the 4 slip planes, p. D_3 is the sum of all slips accumulated on the 12 slip systems. D_4 is a measure of the maximum of energies dissipated due to plastic slip on the 4 slip planes, where energy is the product of the slip rate, $\dot{\gamma}_p^{\alpha}$, and resolved shear stress, τ_p^{α}, on a plane. D_5 is also a measure of the maximum of energies dissipated on the 4 slip planes, but this last metric includes stress normal to the plane, σ_n^p. The nonlocal distance for calculating these metrics ahead of a point on the crack front, r in Figure 2.17(a), should be between 10% and 25% of the crack diameter to be simultaneously in the crack influence zone and in a region of mesh convergence. According to Hochhalter *et al.* , mesh convergence is achieved in this region for crack front element sizes approximately equal to $2a/100$, where a is the crack radius.

Hochhalter *et al.* used this nonlocal approach to study near-crack stresses, as well as localization and accumulation of slip during fatigue loading on the FCC systems near cracked particles to provide mechanics-based insight into nucleation. It was found in a subsequent study by Hochhalter *et al.* [32], that high slip localization and accumulation rate are necessary, but not sufficient, conditions for

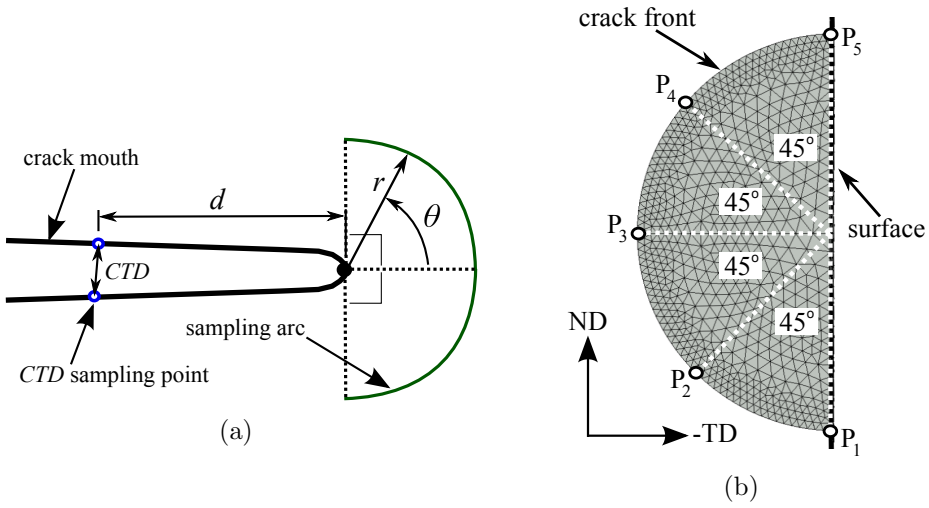

Figure 2.17: Delineation of crack data measurement locations. (a) Sampling arc and CTD sampling point in relation to a typical point on the crack front. (b) Coarse mesh of crack with labels of crack front points P_1 through P_5.

nucleation. The simulation results in this second study elucidated that the local principal tensile stress drives nucleation and that the critical value of this stress for nucleation reduces as slip is accumulated. Moreover, the stresses and slip-based metrics ahead of an incubated MSFC provide a semi-empirical model for the number of cycles required for nucleation, illustrated by Figure 2.18. The maximum tangential stress, $\sigma_{\theta\theta}^{max}$, ahead of an incubated crack was found to be approximately constant after the first load cycle. Therefore, for any $\sigma_{\theta\theta}^{max}$, enough plastic slip has to accumulate (likely over tens to thousands of cycles) for the monitored slip-based metric to reach a critical value, *e.g.* the value of maximum D_1 along the nonlocal arc reaching a critical value, ${}^{cr}D_1^{max}$, as shown in Figure 2.18(a). Furthermore, the values of the slip-based metrics are related bi-linearly to cycles, N, as shown in Figure 2.18(b). Therefore, nucleation can be predicted in simulations by computing $\sigma_{\theta\theta}^{max}$ at the end of the first cycle, then using the relationship in Figure 2.18(a) to obtain ${}^{cr}D_1^{max}$ and the relationship in Figure 2.18(b) to obtain the

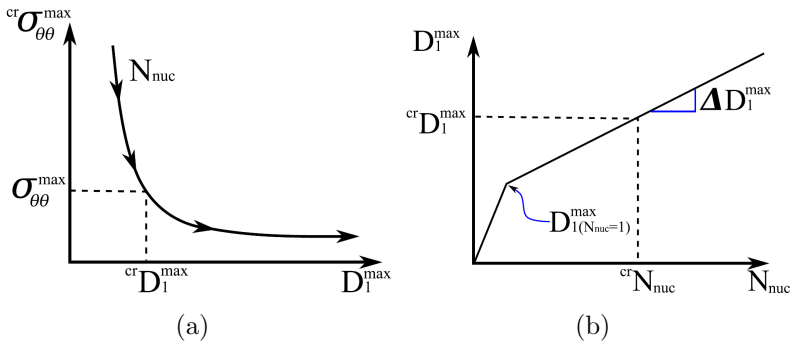

Figure 2.18: Illustration of the relationships governing the number of cycles to nucleate an incubated crack, from Hochhalter *et al.* [32]. (a) Stress required for nucleation dependence on slip near the crack front; (b) Number of cycles to nucleation dependence on the required slip for nucleation from (a).

number of cycles to nucleation, $^{cr}N_{nuc}$, from $^{cr}D_1^{max}$. Ongoing studies are focused on determining the formulae for the curves in Figure 2.18 and how these relationships depend on microstructural heterogeneities in the vicinity of a nucleated crack.

2.3.3 MSFC propagation

The third and final stage of the MSFC phase, MSFC propagation, is also addressed in this framework. A common criterion for MSFC propagation rate adopted by other MSFC researchers, *e.g.* [3, 49, 87], and being investigated in this framework, is the ΔCTD criterion,

$$\frac{da}{dN} = G(\Delta CTD - \Delta CTD_{TH}), \tag{2.21}$$

where da is the crack growth increment over a cycle increment dN, ΔCTD is the cyclic change in CTD, the crack tip displacement, ΔCTD_{TH} is the minimum ΔCTD required for propagation, and G is a material constant. The crack tip is

actually a point along the crack front when cracks are modeled three-dimensionally. CTD is the vector magnitude of the total crack tip displacement vector,

$$\overline{CTD} = \overline{CTOD} + \overline{CTSD_I} + \overline{CTSD_{II}}, \tag{2.22}$$

where $\overline{CTOD}$, $\overline{CTSD_I}$, and $\overline{CTSD_{II}}$ are the RD, ND, and TD vector components, respectively, for a crack in the TD-ND plane [82]. The ΔCTD_{TH} parameter is motivated by the well-known blunting observed prior to MSFC propagation in ductile crystals [39], which can be measured by high resolution microscopic images and/or simulations of experimentally observed MSFC's. For example, Hochhalter *et al.* [32] simulated ΔCTD in replications of MSFC's observed at nucleation and found there is a threshold ΔCTD required for nucleation. Future studies are planned to calibrate ΔCTD_{TH} and G, and validate the linear relationship in Equation 2.21, by performing finite element analyses on models that replicate experimental observations of MSFC propagation subsequent to nucleation. Such calculations involving the ΔCTD criterion are enabled by the explicit geometrical representation of MSFC's.

Figure 2.19 is from one of the studies performed by Veilleux *et al.* [82] to elucidate MSFC propagation dependence on various microstructural heterogeneities. In the study for which results are shown in this figure, the orientation of the grain containing the crack front, grain A, was set to three distinctly different AA7075-T651 grain textures, while all other features, *e.g.* crack size, particle size, and grain C orientation, were kept constant. The three figures show that orientation of the grain containing an MSFC immediately subsequent to nucleation significantly influences the driving force, *i.e.* stress, on the crack. Similar studies by Veilleux *et al.* found that other microstructural heterogeneities, such as the particle containing a nucleated crack and misorientations at grain boundaries significantly influence magnitudes of stresses and irreversible slip ahead of a crack, and, consequently,

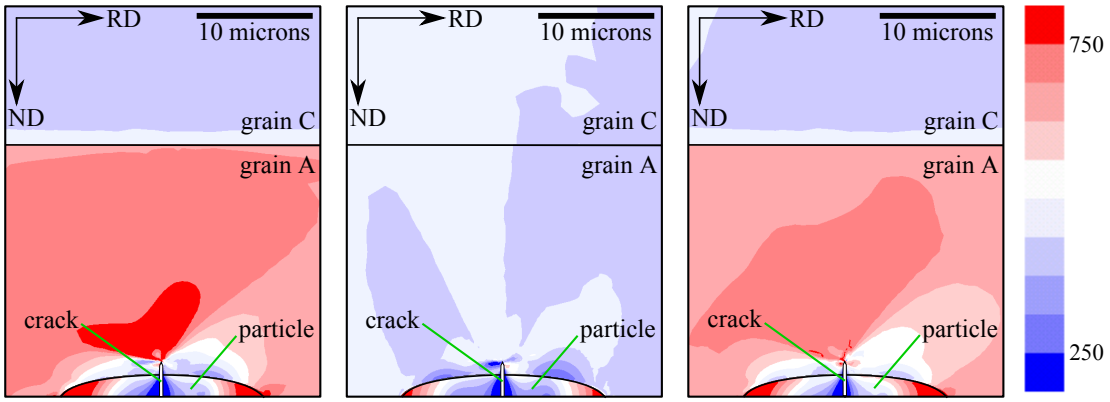

Figure 2.19: Contour plots of grain A orientation influence on first principal stress, σ_1 [MPa], for the three baseline model orientations studied in [82]. In all three plots, the crack length and grain C orientation are kept the same.

CTD is also influenced by these microstructural heterogeneities.

The statistical realization microstructure models developed herein are intended to be used for further studies on microstructural heterogeneity and geometry influences in realistic, polycrystalline models. Ultimately, when all criteria for MSFC stages are implemented and calibrated, these criteria and the statistical realization microstructure models will be combined to perform probabilistic simulations of MSFC evolution.

2.4 Proof-of-concept simulations

Two proof-of-concept simulations are detailed here to illustrate how fatigue is simulated with the framework detailed in Section 2.2 and Section 2.3. Both simulations were performed on a 125 μm cubic microstructure model with 44 grains and 3 particles predicted to crack. Boundary conditions and cyclic loading applied to these

models follow what is shown in Figure 2.2. The first simulation, Section 2.4.1, was performed up to the first load peak with no fatigue cracks. The second simulation, Section 2.4.2, was performed up to the second load peak with an incubated crack in each of the three particles. Simulation results and computation times are detailed in both of these sections.

2.4.1 Stress fields prior to incubation

As part of the framework for predicting fatigue cracking at particles, Bozek *et al.* [7] constructed the particle stress, σ_p, response surface from simulations of a simplified baseline model with a semi-ellipsoidal particle on the surface of a cubic grain. The simulated loading conditions were the first half-cycle of loading shown in Figure 2.2. Here, accuracy of the response surface is evaluated by comparing the predicted stresses from the response surface to those computed in a statistical realization model with three uncracked particles. For this limited sample size, the average difference between particle stresses predicted by the response surface and the maximum particle stresses simulated in the realization model is 18%, *i.e.* the average of the last column in Table 2.3, and the particle stresses from the response surface are always lower than the particle stresses in the realization model. These differences can be attributed to differences in the microstructure of the two models: the statistical realization model is a polycrystal while the baseline models simulated for the response surface were single crystals. In a single crystal model, there are no grain boundaries blocking slip, and, therefore, the increased softening that results in a single crystal leads to more of a decrease in load transferred to the particle than in a polycrystal. Also, the stress contour plot in Figure 2.20 shows that stresses in grains vary by as much as 300 MPa (75%) due to variations in orientation. This

Table 2.3: Maximum particle stresses computed by the response surface from Bozek *et al.* [7] and by simulation of the microstructure finite element model (μstructure FEM) of three uncracked particles shown in Figure 2.20.

particle	response surface σ_p [MPa]	μstructure FEM σ_{xx} [MPa]	difference
#1	910	1120	19 %
#2	1010	1160	13 %
#3	830	1080	20 %

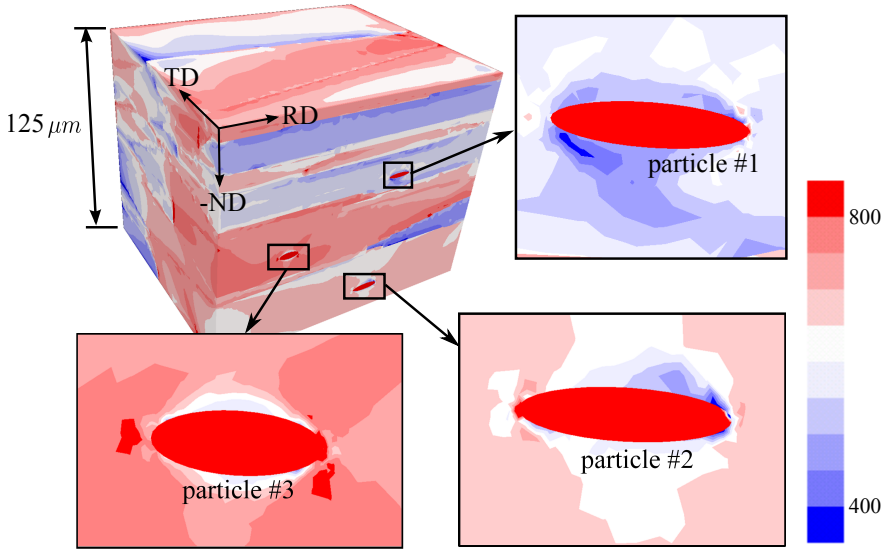

Figure 2.20: Simulated xx-stress, σ_{xx} [MPa], at 1% applied strain of the first load cycle for a microstructure finite element model with three uncracked particles.

likely has a significant effect on where and how fast MSFC's will propagate.

The computation time required for one-half cycle of loading of this microstructure realization model with three uncracked particles, which has approximately 3.5 million degrees of freedom, is approximately 50,000 CPU hours on a Cray XT4 system with Opteron 2.3 GHz Quad Core processors.

2.4.2 Field metrics in the neighborhood of an incubated crack

In this second proof-of-concept study, the same microstructure realization model as the first study is simulated, but with incubated cracks through the three particles. Without growing these cracks, cyclic loading is applied to the peak of the second load cycle. The resulting stress and irreversible slip fields at the peak of the second load cycle are shown in Figure 2.21(a) and Figure 2.21(b), respectively. A visual comparison of these stress fields with those from the previous simulation, Figure 2.20, shows the expected unloading of stresses in the wakes of the cracks; however, stress concentration still exist at the RD_{min} and RD_{max} tips of the particles. Veilleux *et al.* [82] found that these stress concentrations act to increase crack opening for crack lengths almost twice as large as the particle ND radius. Thus, the influence of the particle remains significant after incubation. The D_3 slip-based metric fields, Figure 2.21(b), show three regions of very high slip localization: (1) a region on the boundary of the model, which is likely an artifact of the boundary conditions; (2) lobes extending from the ND_{min} and ND_{max} ends of the particles, which are the slip localizations caused by the cracks; (3) small regions of slip intensification at the RD_{min} and RD_{max} ends of the particles, which are caused by the aforementioned stress localizations in the particle tips.

Crack displacements, stresses, and slip near the fronts of the three incubated cracks are plotted in Figure 2.22. These line plots are generated by performing non-local calculations at 100 evenly spaced sampling points along the crack front, from point P_1 to point P_5 shown in Figure 2.17(b). At each crack front sampling point, non-local measurements are made at the locations illustrated in Figure 2.17(a). ΔCTD is measured at a distance d behind the crack front sampling point, and

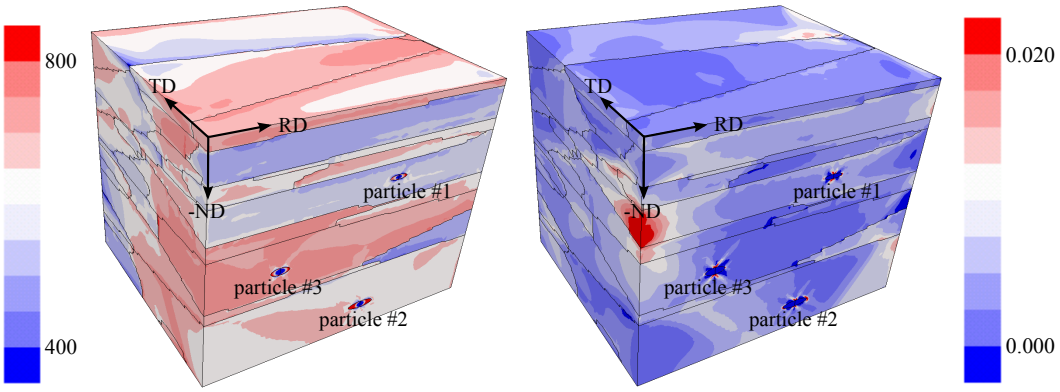

(a) (b)

Figure 2.21: Simulated fields at 1% strain of the second load cycle for a microstructure model with three incubated cracks. (a) xx-stress, σ_{xx} [MPa]; and, (b) D_3 slip-based metric.

stress and slip-based metrics are measured along an arc of radius r ahead of the crack front sampling point. The stress component plotted in Figure 2.22 is $\sigma_{\theta\theta}^{max}$, the maximum tangential stress calculated along the non-local arc. The slip-based metric plotted is D_3^{avg}, the average of slip-based metric D_3 calculated along the arc. Additionally, ΔD_3^{avg}, the change in D_3^{avg} from the first to second load cycle peaks, is calculated to measure slip accumulation rate. For all three incubated cracks, d = 0.5 μm and r = 0.5 μm, because both distances are simultaneously in the crack front influence regions and in regions of mesh convergence for these three cracks. The line plots in Figure 2.22(a) reveal that ΔCTD varies significantly among the particles even though the applied strain on the model is uniform; therefore, microstructural heterogeneities are the main contributors to these ΔCTD variations. Specifically, the highest ΔCTD variation observed is 33% between particles #1 and #2 at point P_3. $\sigma_{\theta\theta}^{max}$ generally follows the same trends as ΔCTD among the particles: for example, compare the line plots in Figure 2.22(a) and Figure 2.22(b) at point P_3. However, $\sigma_{\theta\theta}^{max}$ line plots are much less smooth along the crack front, due to the numerical sensitivity of measuring this non-regularized stress component

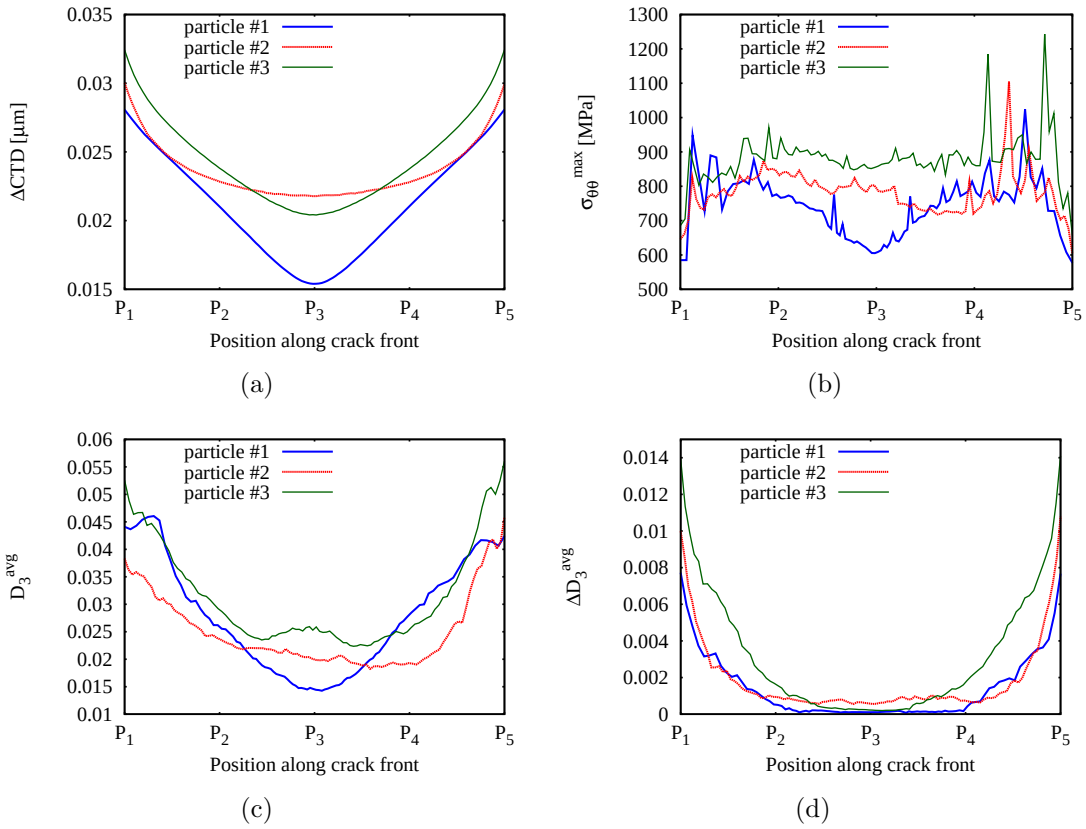

Figure 2.22: Line plots of field metrics in the neighborhood of the three incubated cracks shown in Figure 2.21. (a) ΔCTD for second load cycle; (b) $\sigma_{\theta\theta}^{max}$ at peak of second load cycle; (c) D_3^{avg} at peak of second load cycle; and, (d) ΔD_3^{avg} from first cycle to second cycle.

near a crack front in an anisotropic material. D_3^{avg} line plots in Figure 2.22(c) also show similar trends to ΔCTD among the three cracks, which is logical since crack blunting is directly a result of irreversible slip accumulation near the crack front. Based on the findings from Hochhalter *et al.* [32], the incubated crack at particle #3 will nucleate the soonest because it has the highest stress, most accumulated slip at the second cycle, and the fastest rate of slip accumulation (see ΔD_3^{avg} line plots in Figure 2.22(d)). The crack in particle #3 having the highest ΔCTD in Figure 2.22(a) further supports this conclusion.

The computation time required for loading to the second load peak cycle for this microstructure realization model with three nucleated cracks, which has approximately 6.5 million degrees of freedom, is approximately 270,000 CPU hours on a Cray XT4 system with Opteron 2.3 GHz Quad Core processors.

2.5 Summary, feasibility, and limitations of approach

The main thrust of the work presented in this paper was toward the creation of a computational framework that accurately and probabilistically models fatigue crack propagation at the microstructural length scale for a proof-test case, high strain fatigue in AA7075-T651. Toolsets were detailed that generate and discretize statistically accurate microstructure geometry models and explicitly simulate MSFC evolution by physically justified criteria. The combination of complex geometries, material behavior, and fatigue crack characteristics within the microstructure require substantial computation times. A 125 μm cubic microstructure with 44 grains and 3 cracked particles (6.5 million degrees of freedom) requires 270,000 CPU hours for 2 load cycles on a massively parallel supercomputer. Since MSFC propagation often consumes tens or hundreds of thousands of cycles, the total computation to explicitly model the entire MSFC history would be $O(10^9)$ CPU hours. Therefore, the following strategies should be considered to utilize this framework in a computationally tractable manner:

1. Develop non-linear cycle-jumping algorithms to project the fatigue crack and material states out to many cycles without simulating over those cycles. Such algorithms are common in the fatigue literature for MLFC propagation, but the authors of this paper are unaware of successful extension of these

strategies to polycrystalline plasticity.

2. Perform lower fidelity probabilistic approaches to determine which microstructural configurations cause the fastest MSFC propagation rates. For example, the MSFC incubation filtering procedure by Bozek *et al.* can be extended to determining which incubated cracks will nucleate based on the governing local microstructural heterogeneities, and similarly, which nucleated cracks will propagate the fastest through the neighboring grains. As shown by the study of the incubation filter's accuracy in Section 2.4.1, such filtering procedures are lower fidelity, but they do provide a good first-order determination of which microstructural heterogeneities to simulate in a high fidelity finite element analysis.

3. Also, perform statistical analyses *a priori* to determine how many high fidelity microstructural analyses are required to improve the minimum life tail of a low fidelity probabilistic fatigue life curve. For example, the reader is referred to the second and third levels of the damage and durability simulation (DDSIM) strategy developed by Emery *et al.* [16].

As stated by McDowell and Dunne [50], incorporation of microstructural scale fatigue simulations in fatigue life prognoses is still a long-term goal. The framework presented in this study provides a high risk, high reward, high fidelity foundation for achieving this goal.

ACKNOWLEDGEMENTS

Dr. Gerd Heber developed the parallel finite element code that was used for the finite element simulations presented here. The crystal plasticity model was implemented by Dr. Antoinette Maniatty, Dr. David Littlewood, and Dr. Paul Wawrzynek. Experimental observations were made by Joel Payne and Dr. Elias Anagnostou at the Northrop Grumman Corporation. This work is sponsored by the Defense Advanced Research Projects Agency under contract HR0011-04-C-0003 with Dr. Leo Christodoulou as the DARPA Program Manager. This work is also funded by NASA under contract ARMD-NNX07AB69A with Dr. Ed Glaessgen as the NASA Contract Monitor, and by the U.S. Department of Energy Computational Science Graduate Fellowship Program of the Office of Science and National Nuclear Security Administration in the Department of Energy under contract DE-FG02-97ER25308. The simulations needed to complete this study were carried out on a NASA AMES supercomputer, Pleiades, and on resources of the National Energy Research Scientific Computing Center, which is supported by the Office of Science of the U.S. Department of Energy under contract DE-AC02-05CH11231.

CHAPTER 3

A GEOMETRIC APPROACH TO MODELING MICROSTRUCTURALLY SMALL FATIGUE CRACK FORMATION: V. OBSERVATION AND SIMULATION OF PROPAGATION DEPENDENCE ON MICROSTRUCTURAL HETEROGENEITY

This is the fifth in a series of papers focused on developing a geometrically explicit, high fidelity approach to simulating microstructurally small fatigue crack evolution, with high strain conditions in aluminum alloy (AA)7075-T651 as the proof-test application. The research presented in the fourth paper in this series [82] simulated crack displacement, irreversible slip, and stress metrics near the crack front of a stationary MSFC immediately following nucleation. Simulations were performed on a baseline model to study the influences of various microstructural heterogeneities on these MSFC metrics. The research presented in the current paper further investigates the relationships between heterogeneities and each of these metrics, and evaluates how these metrics are related to MSFC propagation subsequent to nucleation. Observations of multiple propagating MSFC's over thousands of load cycles are inspected to determine microstructure-dependent patterns in MSFC propagation rates and directions. Simulations are then performed on a replication model of one of these experimental observations to compute the crack displacement, irreversible slip, and stress fields near the crack front of a nucleated MSFC. It is found that grain boundaries, when preferentially aligned with the crack, are the path of MSFC propagation, which is supported by determination of high stresses and slip pileup at these grain boundaries. When grain boundaries are absent or approximately normal to the crack front, MSFC propagation is intragranular and in Stage II. The rate of propagation is found to be proportional to

crack tip displacement, but the proportionality constant is an order of magnitude less than previously reported for AA7075-T651.

3.1 Introduction

Motivations for, and detailed descriptions of, the geometric modeling approach being developed in this series of papers are given in prior studies [7,31]. In this series, the incubation, nucleation, and MSFC propagation stages in AA7075-T651, as defined by Bozek *et al.* [7], are being individually investigated and modeled through high resolution observation and detailed finite element modeling of the microstructure. Bozek *et al.* addressed the incubation stage: cracking of Al_7Cu_2Fe particles. Hochhalter *et al.* [31,32] addressed the nucleation stage: extension of an incubated crack across the particle-grain interface. Most recently, Veilleux *et al.* [82] investigated metrics assumed to indicate crack behavior in the MSFC propagation stage: microstructure-governed fatigue crack evolution after nucleation. The three MSFC metrics studied for nucleation - near-crack accumulated slip, maximum tangential stress ahead of the crack, and crack tip displacement - were evaluated in polycrystalline baseline models to begin to understand the dependence of these metrics on various microstructural heterogeneities during the MSFC propagation stage.

This, the fifth paper in the series, is focused on understanding the dependence of MSFC propagation direction and rate on these MSFC metrics. First, prior related research is summarized to highlight which MSFC trends are expected in subsequent studies, and to reveal the novel contributions this paper is intended to provide to the fatigue community.

3.1.1 Background

MSFC propagation is governed by crack blunting characteristics, and microstructural heterogeneities and loads act to vary these characteristics [39]. Forsyth [20] delineated two distinct MSFC Stages, characterized by the type of crack blunting: Stage I - sliding dominated; and, Stage II - opening dominated. Moreover, Stage I is along the slip system(s) most favorably aligned with the direction(s) of maximum shear stress, while Stage II is in the direction normal to maximum tangential stress ahead of the crack front. Veilleux *et al.* [82] give a detailed description of the two stages and prior research thereof related to the MSFC propagation studies in this series of papers. Most importantly, Veilleux *et al.* theorize, from prior studies and observations, that MSFC propagation in AA7075-T651 is solely in Stage II. They also validate this theory in baseline model simulations of MSFC's, where the computed displacements along the crack front have opening components two orders of magnitude larger than the sliding components. This is certainly a large enough opening/sliding ratio for Stage II, since Li [43] showed that a sufficient approximation of Stage II is when the opening displacement simply exceeds the sliding displacement.

Although a Stage II MSFC mostly propagates in the direction normal to maximum tangential stress, heterogeneous fracture toughnesses among microstructural features have been found to cause local deviations from this direction. In aluminum alloy 7010, Patton *et al.* [58] found that MSFC propagation often transitions between intragranular and intergranular, causing slight deviations in the crack trajectory since intergranular crack paths (grain boundaries) are commonly misaligned from the average Stage II propagation direction. Frequent transitions between intergranular and intragranular propagation of a Stage II MSFC are most probable

if grain boundaries have a lower fracture toughness than the grains. However, for the material and loading direction studied in this series of papers, AA7075-T651 loaded in the rolling direction (RD), intergranular propagation paths are likely rare and short since the Stage II crack propagation direction is approximately normal to the RD and most grain boundaries encountered by the crack are aligned with the RD. Nevertheless, the influences of grain boundaries are investigated in Section 3.2 and Section 3.3 of this paper.

Microstructural heterogeneities are assumed also to influence the Stage II propagation rate. Laird [39] theorized that crack opening is the governing MSFC propagation rate mechanism in Stage II. Recently, numerous researchers have performed crack analysis at the microstructural length scale to illustrate MSFC opening dependence on grain orientation for various load ratios and materials, *e.g.* [3, 34, 65, 82, 84]. For the same material and loads studied here, the baseline model simulations performed by Veilleux *et al.* [82] revealed variation in grain orientation causes only mild variations in crack blunting, with no more than 6% variation immediately following nucleation and less than 1% variation once a nucleated crack nears the first grain boundary. These results are seemingly contradicted by prior observations of MSFC propagation in AA7075-T651, at much lower applied strains than those studied by Veilleux *et al.* , which show significant changes in fatigue striation distances within grains and across grain boundaries [87]. However, observations have also elucidated that increasing strain magnitude causes decreasing microstructure-dependent variations in striations and roughness-induced fatigue crack closure [67]. Observations and simulations presented in this paper are aimed at further determining the influence of orientations and misorientations on MSFC propagation at high strain levels in AA7075-T651.

Since the 1960's, many researchers have attempted to incorporate MSFC behavior into common macroscale fatigue crack growth rate equations. Multiple researchers have employed an effective ΔK formulation within the Paris model [57] to account for the higher rates of propagation at the microstructural length scale [34, 46, 67, 84]. Other researchers have employed modified Coffin-Manson relationships to model MSFC nucleation [51, 88] and MSFC propagation at varying load magnitudes [52]. However, such formulae either implicitly incorporate, or ignore altogether, MSFC dependence on the physical mechanism - crack blunting.

Consequently, more recent research, including this paper, has focused on developing and employing formulae that explicitly incorporate the dependence of MSFC propagation rate on crack blunting. Blunting is typically measured as the cyclic change in crack displacement near the crack 'tip', *i.e.* a point along the crack front. For consistency, the same crack tip displacement definitions and formulae used by Veilleux *et al.* [82] are used in this study. The vector crack tip displacement formulae are

$$\overline{CTSD} = \overline{CTSD_I} + \overline{CTSD_{II}}, \tag{3.1}$$

$$\overline{CTD} = \overline{CTOD} + \overline{CTSD_I} + \overline{CTSD_{II}}, \tag{3.2}$$

where $\overline{CTOD}$, $\overline{CTSD_I}$, and $\overline{CTSD_{II}}$ are the RD, ND, and TD components, respectively, for a crack in the TD-ND plane, the average crack plane of a Stage II MSFC loaded in the RD. The vector magnitudes are $CTOD$, $CTSD_I$, $CTSD_{II}$, $CTSD$, and CTD. $CTOD$ is crack tip opening displacement, $CTSD$ is crack tip sliding displacement, and CTD is crack tip displacement. The cyclic amplitude of crack tip displacement includes a 'Δ' in the symbols, *e.g.* $\Delta\overline{CTD}$ and ΔCTD. ΔCTD is the primary crack tip displacement discussed in this paper; however, simulation results not presented here showed that ΔCTD is approximately equal to $\Delta CTOD$ and $\Delta CTSD$ is negligible in comparison to $\Delta CTOD$. In a review of

MSFC propagation research, McClintock [49] shows that MSFC propagation rate is linear with respect to ΔCTD and a critical amount of ΔCTD is required for the onset of propagation. Therefore, researchers, *e.g.* [51, 88], have proposed a formula that models the observed behavior,

$$\frac{da}{dN} = G(\Delta CTD - \Delta CTD_{TH}), \tag{3.3}$$

where $\frac{da}{dN}$ is the cyclic crack growth rate, G is the linear constant relating ΔCTD to $\frac{da}{dN}$, and ΔCTD_{TH} is the minimum ΔCTD required for propagation. ΔCTD_{TH} is on the order of the Burger's vector during MSFC propagation [49]. Furthermore, G is commonly observed and modeled as being between 0.3 and 0.5 at the microstructural length scale [49, 51, 88]. However, G is also known to vary significantly during MSFC propagation, and the average value of G is highly dependent on material, maximum strain, and strain ratio [49].

The investigation by Veilleux *et al.* [82], continue herein, of near-crack slip and stress field metrics to predict MSFC propagation is motivated by previous studies of nucleation [31, 32]. Since the nucleation and MSFC propagation stages are characterized by a Stage II MSFC propagating into or through a face-centered cubic (FCC) lattice, it is hypothesized that similar field metrics can be applied to simulate both stages. In the prior nucleation studies, a non-local sampling arc was used to calculate mesh insensitive tangential stresses and irreversible slip accumulation near a point on the crack front. The non-local arc radius needs to be larger than 10% of the crack diameter to be sampling converged fields in a mesh with crack front element sizes approximately $1/100^{th}$ the size of the crack. The magnitude of the maximum tangential stress along this arc, $\sigma_{\theta\theta}^{max}$, proved to be a sufficient measure of the MSFC nucleation driving force. Furthermore, the cyclic accumulation of the average or the maximum slip-based metric, D_i^{max} or D_i^{avg}, for any of the five metrics ($i = 1...5$) given in [31] proved to measure sufficiently the

reduction in fracture toughness ahead of an incubated crack due to localization of irreversible slip along the 12 primary face-centered cubic (FCC) slip systems. The slip-based metric investigated in this study is D_3^{avg}, the average of

$$D_3 = \gamma = \sum_{\alpha=0}^{N_s} \gamma^{\alpha} \tag{3.4}$$

along the non-local arc, where α is one of the twelve slip systems, $N_s = 12$ is the number of slip systems, and γ^{α} is the total irreversible slip accumulated on slip system α. D_3^{avg} is chosen here because this is the most mesh insensitive metric.

Through baseline model simulations, Veilleux *et al.* [82] determined how the computed near-crack field metrics of an MSFC immediately subsequent to nucleation are dependent on microstructural heterogeneities. The field metrics studied were $\sigma_{\theta\theta}^{max}$ and D_3^{avg} along the non-local arc, and CTD calculated at a location of mesh insensitivity behind the crack front. Three-dimensional variations in these metrics were presented and evaluated by plotting the computed field metrics along the entire crack front. The load conditions were the same as those studied by Hochhalter *et al.* [31,32]: constrained, axial tension in the RD with 1% maximum strain and a strain ratio, R, equal to 0.1. For the simplified particle and grain geometries studied by Veilleux *et al.* , the micro-notch root influence region of the particle was found to extend at least 50% of the particle size beyond the particle-grain interface. When the simulated MSFC was 50% of the particle size beyond the particle-grain interface, the particle caused a 10% increase in CTD, a 5% increase in D_3^{avg}, and a 1% increase in $\sigma_{\theta\theta}^{max}$. Local grain orientation influences on the near-crack front fields were also studied by simulating three distinctly different orientations observed in AA7075-T651 grains. The three orientations, referenced by Veilleux *et al.* as the 'weak', 'rotated', and 'strong' orientations, were chosen because each have significantly different Schmid factors (for loading in the RD), which are likely to cause three different types of yielding. The terms 'weak' and

'strong' are chosen in reference to the relative yield strengths of these two orientations, rather than their relative fracture toughnesses. In fact, observations in Section 3.2 suggest the weak orientation is more resistant to fatigue fracture than the strong orientation. Previous studies have used 'hard' and 'soft' to define the 'strong' and 'weak' orientations, respectively, used here [13], but the former terminology suggests differences in the initial stiffness. Since all orientations herein have approximately the same initial stiffness, the terms 'soft' and 'hard' are not used. The term 'rotated' is defined in reference to the rotated cube (or twisted cube) family [58, 76] of textures to which this orientation belongs. The weak orientation has one slip system with a Schmid factor much higher than the others, which is most likely to cause early yielding with most slip accumulation in one direction. The rotated orientation has two slip systems with Schmid factors much higher than the others, which is most likely to cause early yielding with most slip accumulation in two directions. The strong orientation has no slip systems with high Schmid factors, which is most likely to cause later yielding than the other two orientations. For an MSFC nucleated 1 μm beyond the particle-grain interface, Veilleux *et al.* found the strong orientation to cause CTD approximately 5% higher than the rotated orientation and approximately 2% higher than the weak orientation. $\sigma_{\theta\theta}^{max}$ was much higher in the strong and weak orientations than the rotated orientation, and D_3^{avg} was highest in the weak orientation. However, the rotated orientation had significantly higher cyclic increase in D_3^{avg}, *i.e.* ΔD_3^{avg}, after the second load peak, than the other two orientations. In fact, the weak orientation showed no increase in D_3^{avg} after the second load peak. All orientations produced negligible increases in $\sigma_{\theta\theta}^{max}$ after the first load cycle. Therefore, if slip accumulation continues to indicate a reduction in fracture toughness during MSFC propagation (like it does for nucleation), and $\sigma_{\theta\theta}^{max}$ is not high enough to initially

drive the crack in the first few load cycles after a propagation step, then the weak orientation will never weaken enough over multiple cycles to allow for continued MSFC propagation. In contrast, the rotated orientation will weaken fastest and could allow for faster MSFC propagation even though this orientation has the lowest $\sigma_{\theta\theta}^{max}$. The rotated orientation maintains a direction of $\sigma_{\theta\theta}^{max}$ aligned with the applied loading direction, but the weak and strong orientations cause the direction of $\sigma_{\theta\theta}^{max}$ to tilt as much as 20° from the loading direction. Therefore, if the MSFC propagation direction is Stage II, *i.e.* normal to $\sigma_{\theta\theta}^{max}$, then variations in texture will cause variations in the MSFC propagation directions.

However, this is mostly speculation, motivating the need for a better understanding of the governing microstructural features and mechanisms for MSFC propagation. Meeting this need is facilitated herein through interpretation of experimental data and simulation through finite element models that replicate experimental observations.

3.1.2 Methodology of MSFC observation and replicated microstructure simulation

The goal of the research presented in this paper is to understand better the characteristics of MSFC propagation at high strain levels in AA7075-T651. To facilitate this goal, MSFC propagation is observed and simulated within the same highly stressed region of a double edge-notched specimen tested by Payne *et al.* [59] and investigated in previous studies of incubation [7] and nucleation [31, 32]. The reader is referred to these studies for detailed descriptions of the observation techniques, loading conditions, and material models. In summary, observations were

made in a 1.50 mm x 0.50 mm window within the notch root, and the loading conditions tested and simulated in this notch root are constrained, axial tension with approximately R=0.1 (min/max strain ratio) and approximately 1% maximum strain in the RD. The particles are modeled as linear elastic, with a stiffness more than twice the average grain stiffness [7], and the grains are modeled by the rate-dependent crystal plasticity formulation from Matous and Maniatty [48], with parameters calibrated for AA7075-T651 [7]. All particle-grain interfaces and grain boundaries are modeled as perfectly bonded, since debonding was not observed at these microstructural features under the aforementioned loading [59].

The following sections of this paper are focused on studying the mechanisms of MSFC propagation for this material and loading conditions. In Section 3.2, observations of four MSFC's propagating immediately subsequent to nucleation are critically evaluated to reveal relationships between MSFC propagation characteristics and microstructural heterogeneities. In Section 3.3, one of these four observations is replicated and simulated in a finite element model to further investigate the influences of microstructural heterogeneities on MSFC propagation and to begin to understand the dependence of MSFC propagation on ΔCTD, $\sigma_{\theta\theta}^{max}$, and D_3^{avg}. Finally, in Section 3.4, the most important findings of the previous two sections are summarized and future related work is recommended.

3.2 Observations of propagation subsequent to nucleation

Of the 1423 particles monitored by Payne *et al.* [59], a subset of 4 particles and the MSFC's they spawned are investigated in this study. The 7 high resolution observation regions in Figure 3.1 through Figure 3.7 were considered as candi-

dates for this study, because these observation regions contain the 7 particles from which fatigue crack nucleation was observed [32]. All 7 of these nucleated cracks also propagated subsequent to nucleation, which suggests MSFC arrest is unlikely immediately following nucleation. However, the direction and rates of MSFC propagation vary among these particles, so the focus here is on understanding how, if at all, these variations are caused by the three heterogeneous microstructural features most commonly encountered by an MSFC: grain texture, grain boundaries, and the micro-notch root of the particle originally spawning the crack. Consequently, 3 of the 7 observed MSFC's are not investigated here, because they have other features likely influencing MSFC propagation: observation region P87, Figure 3.1, has a micro-void that appears to have caused MSFC nucleation and approximately 1.5 μm of propagation on one side of the particle; observation region P22, Figure 3.2, has an incubated crack likely causing shielding at the +ND tip of the nearby nucleated crack; and, observation region P50, Figure 3.3, has a MSFC nucleating and propagating along a sub-surface particle-grain interface. Observation of these 3 features in a very small dataset suggests each feature is likely common enough to be addressed for the potential to cause or significantly influence a fatigue life-limiting crack. However, not enough data was provided for this study to observe and simulate accurately these features. Thus, MSFC propagation direction and rate are investigated here for the 4 remaining observation regions: P187, P208, P124, and P91, in Figure 3.4, Figure 3.5, Figure 3.6, and Figure 3.7, respectively.

3.2.1 Propagation direction characteristics

Since MSFC propagation is assumed here to be entirely in Stage II, the direction of propagation should be approximately normal to the local maximum tangential

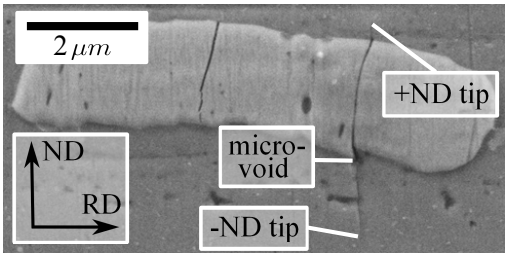

Figure 3.1: Scanning electron micrograph of the crack in observation region P87 from the study performed by Payne *et al.* [59]. Micrograph courtesy of Northrop Grumman Corporation.

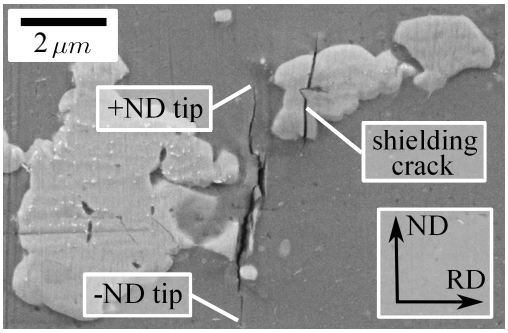

Figure 3.2: Scanning electron micrograph of the crack in observation region P22 from the study performed by Payne *et al.* [59]. Micrograph courtesy of Northrop Grumman Corporation.

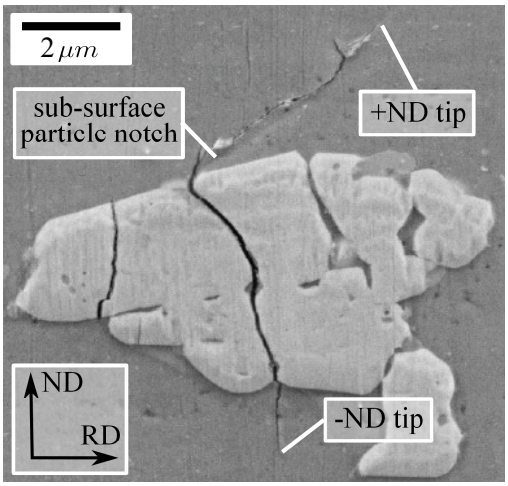

Figure 3.3: Scanning electron micrograph of the crack in observation region P50 from the study performed by Payne *et al.* [59]. Micrograph courtesy of Northrop Grumman Corporation.

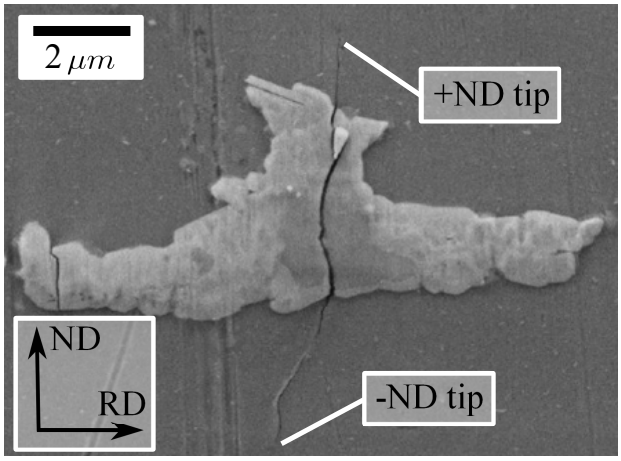

Figure 3.4: Scanning electron micrograph of the crack in observation region P187 from the study performed by Payne *et al.* [59]. Micrograph courtesy of Northrop Grumman Corporation.

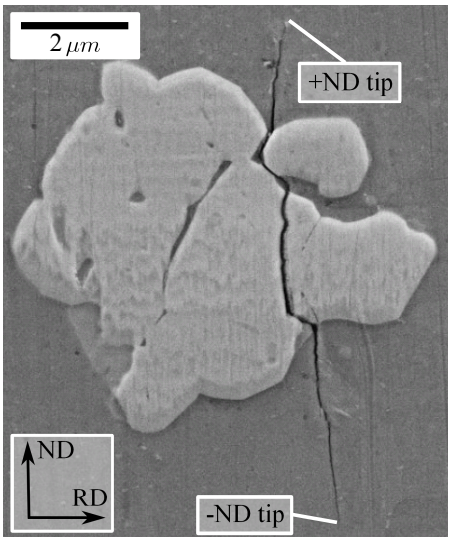

Figure 3.5: Scanning electron micrograph of the crack in observation region P208 from the study performed by Payne *et al.* [59]. Micrograph courtesy of Northrop Grumman Corporation.

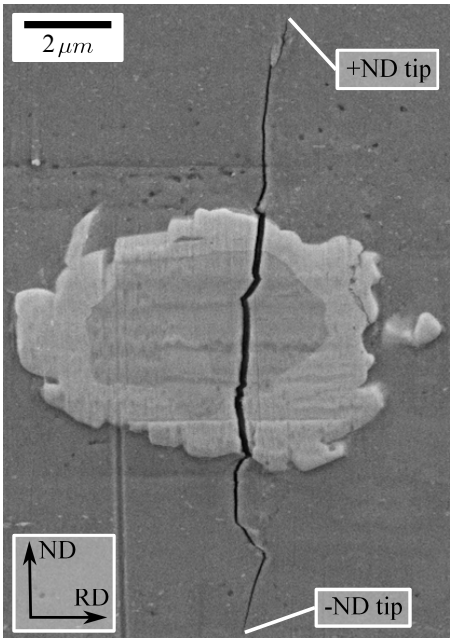

Figure 3.6: Scanning electron micrograph of the crack in observation region P124 from the study performed by Payne *et al.* [59]. Micrograph courtesy of Northrop Grumman Corporation.

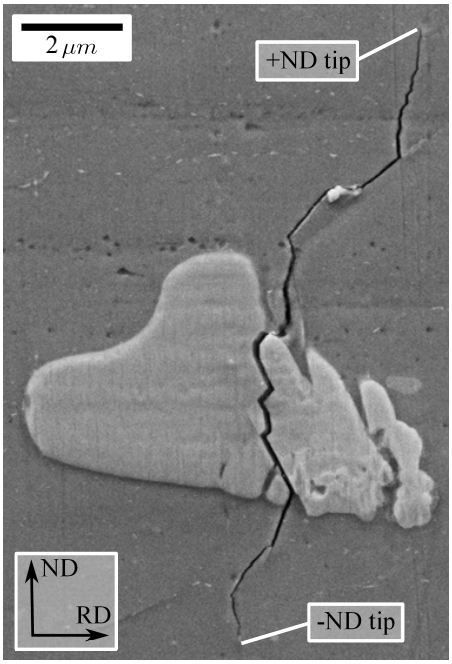

Figure 3.7: Scanning electron micrograph of the crack in observation region P91 from the study performed by Payne *et al.* [59]. Micrograph courtesy of Northrop Grumman Corporation.

stress direction. The observations in Figure 3.4 through Figure 3.7 support this Stage II assumption, since the average propagation direction is approximately normal to the applied loading direction for all 4 cracks. However, there are localized kinks in the crack trajectory for 3 of the 4 observations: in P187, between the particle and the -ND crack tip; in P124, also between the particle and the -ND crack tip; and, in P91, on both sides of the particle.

To evaluate whether texture heterogeneity influences these noticeable changes in MSFC propagation direction, the grain textures recorded from orientation imaging microscopy (OIM) observations are overlaid with the crack paths recorded from scanning electron microscopy (SEM) observations. Figure 3.8, Figure 3.10, Figure 3.12, and Figure 3.14 are plots of the highest Schmid factors for the grain textures observed in P187, P91, P208, and P124, respectively. Figure 3.9, Figure 3.11, Figure 3.13, and Figure 3.15, respectively, are plots of the second highest Schmid factors for these same four observations. These plots were generated by recording grain textures and sketching grain boundaries in high resolution OIM images. Grain boundaries were sketched between regions having a misorientation of 6° or greater. The rotations for each grain texture were then converted to equivalent Schmid factors for loading in the RD. For each grain, the Schmid factors were ordered from highest to lowest, and the first and second highest factors were plotted. Schmid factors are plotted from red to blue, with red signifying lower Schmid factor and blue signifying higher Schmid factor. Dark red in the highest Schmid factor plots is assumed to indicate grains with higher stresses at uniform applied strain levels above the macro-scale yield limit, such as the 1% maximum strain investigated here, because these grains have no slip systems preferentially aligned with the average directions of maximum yield stress (45° to the applied loading axis). Since all 12 primary slip systems are assumed to have the same critical shear

stress for slip onset, the first slip systems to yield in red grains will generally yield later than the first slip systems to yield in blue grains. Grains that are dark blue in both the highest and second highest Schmid factor plots will yield the earliest and likely soften the most, because these grains have two or more directions approximately aligned with the average direction of maximum yield stress. Furthermore, grains that are red highest Schmid factor plots have Schmid factors most similar to the 'strong' orientation studied by Veilleux *et al.* [82]; grains that are blue in both the highest and second highest Schmid factor plots have Schmid factors most similar to the 'rotated' orientation; and, grains that are blue in the highest Schmid factor plots and red in the second highest Schmid factor plots have Schmid factors most similar to the 'weak' orientation. The crack path through 3000 cycles of loading is sketched from SEM and overlaid in each of these plots to show crack propagation direction relative to the two highest Schmid factors.

Two types of microstructural heterogeneities appear to influence MSFC kinking in these plots. In P187, Figure 3.8 and Figure 3.9, the kinking near the -ND crack tip occurs when the crack crosses from a moderately weak, rotated grain, to a strong grain. If this crack is solely in Stage II, then significant variation in texture between these two grains is assumed to be causing a local rotation in the maximum tangential stress direction. However, simulation of stresses, like that presented in Section 3.3, is required to prove this assumption. In P124, Figure 3.14 and Figure 3.15, the observed locations of kinking between the particle and the -ND crack tip are along grain boundaries. This agrees with findings from Patton *et al.* [58] for aluminum alloy 7010: MSFC propagation temporarily transitions to intergranular propagation when grain boundaries immediately ahead of an MSFC are preferentially aligned with the propagation direction, presumably because grain boundaries have lower fatigue resistance than grains. In P91, Figure 3.10 and Fig-

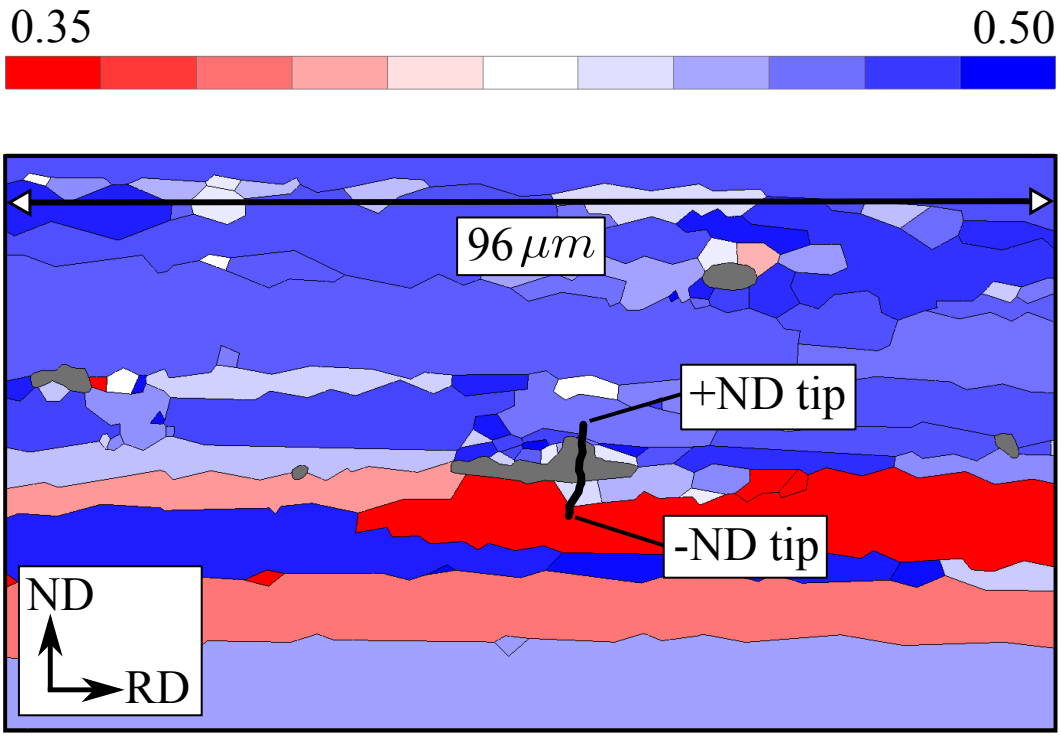

Figure 3.8: Highest Schmid factor plot of texture in MSFC observation region P187. The shape of the MSFC after 3000 load cycles is sketched.

ure 3.11, the kinking between the particle and the +ND crack tip again appears to be caused by the crack temporarily propagating along grain boundaries, and the kinking between the particle and the -ND crack tip appears to be caused by the crack propagating from a strong grain to a weak grain. Alternatively, for all observations of kinking, there could be sub-surface features, not observed here, causing or contributing to changes in the maximum tangential stress direction and/or the direction of lowest fatigue resistance. Nonetheless, simulation of a finite element model replicating the microstructure on the P124 observation surface is performed and presented in Section 3.3.1 to evaluate, as best as possible for the provided microstructural description, whether MSFC propagation direction is normal to local maximum tangential stress and why deviations from this propagation direction are caused by grain boundaries.

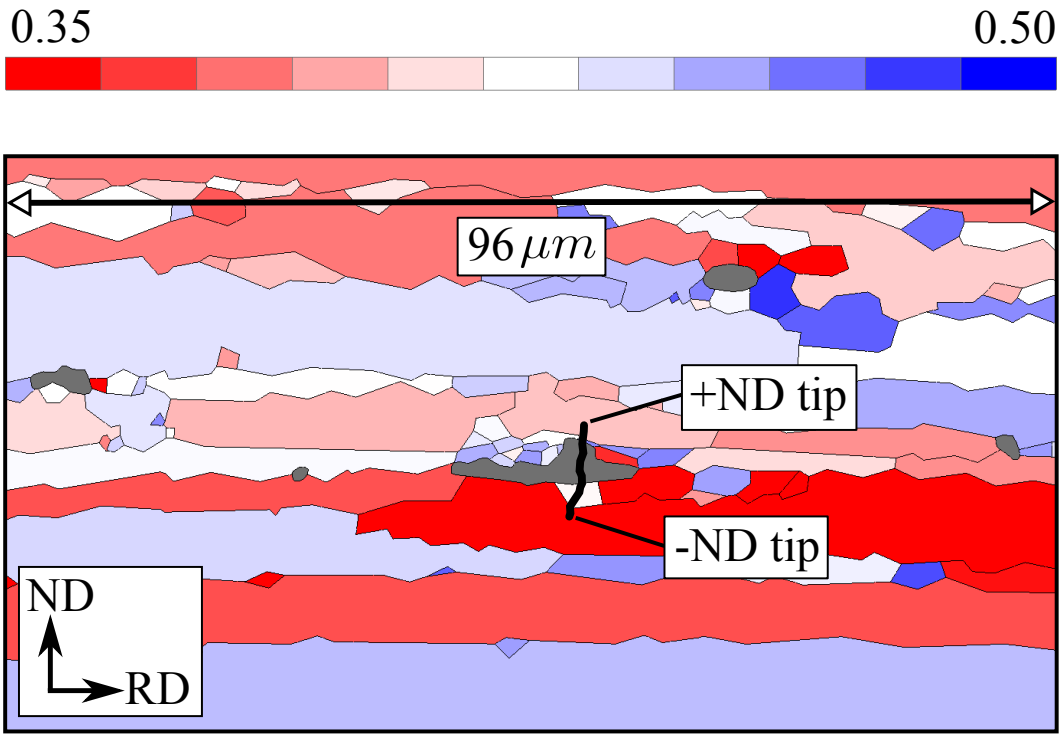

Figure 3.9: Second highest Schmid factor plot of texture in MSFC observation region P187. The shape of the MSFC after 3000 load cycles is sketched.

In the next sub-section, the Schmid factor plots are paired with the recorded MSFC size histories from these 4 observations to investigate microstructural heterogeneity influences on MSFC propagation rate.

3.2.2 Propagation rate characteristics

MSFC propagation rates are determined by the changes in crack lengths from one cycle of observation to the next for observations made after nucleation in P187, P91, P208, and P124. Observations were made at cycles 1, 3, 10, 30, 100, 300, 1000, and 3000. The MSFC's in P187 and P91 nucleated prior to cycle 30, so 4 intervals of fatigue crack growth are recorded from the intermittent observations:

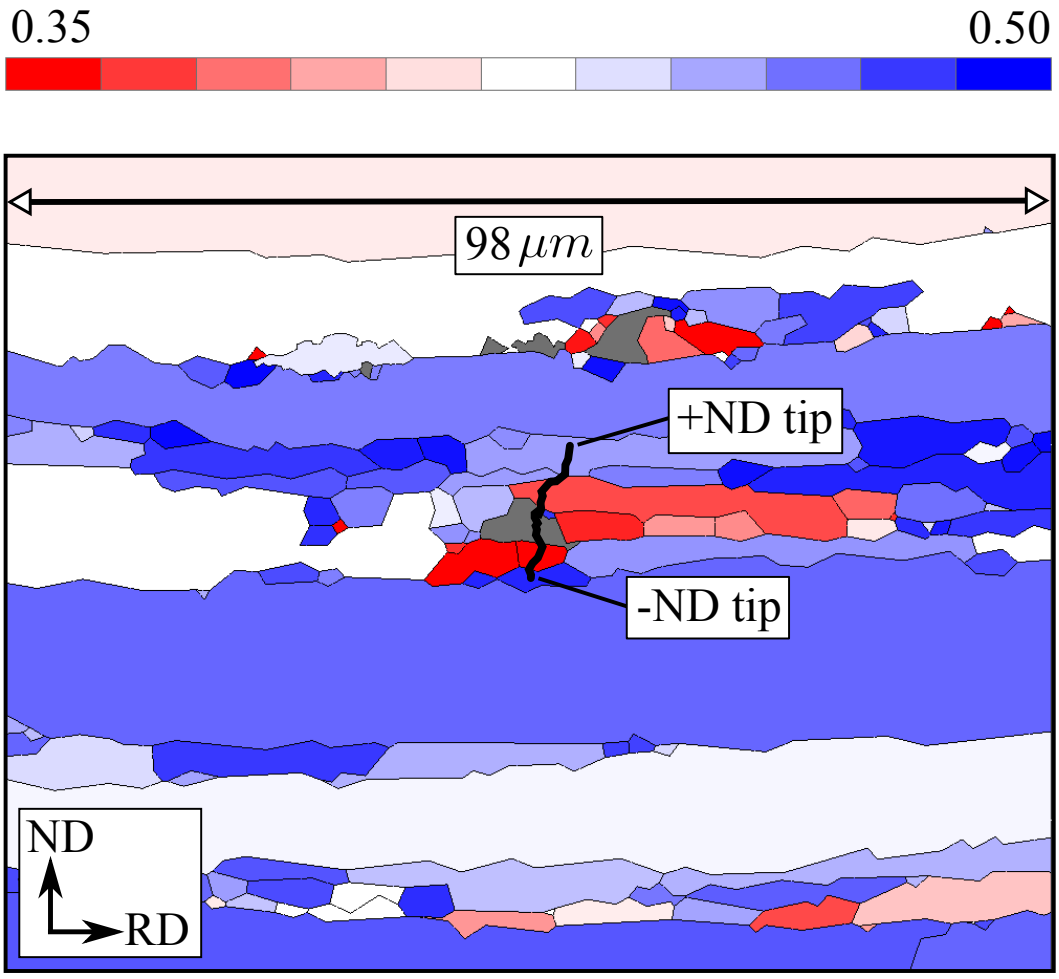

Figure 3.10: Highest Schmid factor plot of texture in MSFC observation region P91. The shape of the MSFC after 3000 load cycles is sketched.

from cycle 30 to 100, 100 to 300, 300 to 1000, and 1000 to 3000. The MSFC in P208 nucleated prior to cycle 1000, so only one interval of fatigue crack growth was recorded, and the MSFC in P124 nucleated prior to cycle 300, so two intervals of fatigue crack growth were recorded. The recorded fatigue crack growth rates are in Table 3.1, where the observation regions are listed from the slowest to the fastest propagating MSFC between cycles 1000 and 3000. For each cycle interval, N_{n-1} to N_n, the half-lengths of the crack paths in the observation surfaces at N_{n-1} and N_n are recorded as a_{n-1} and a_n, respectively, and the crack growth rate over

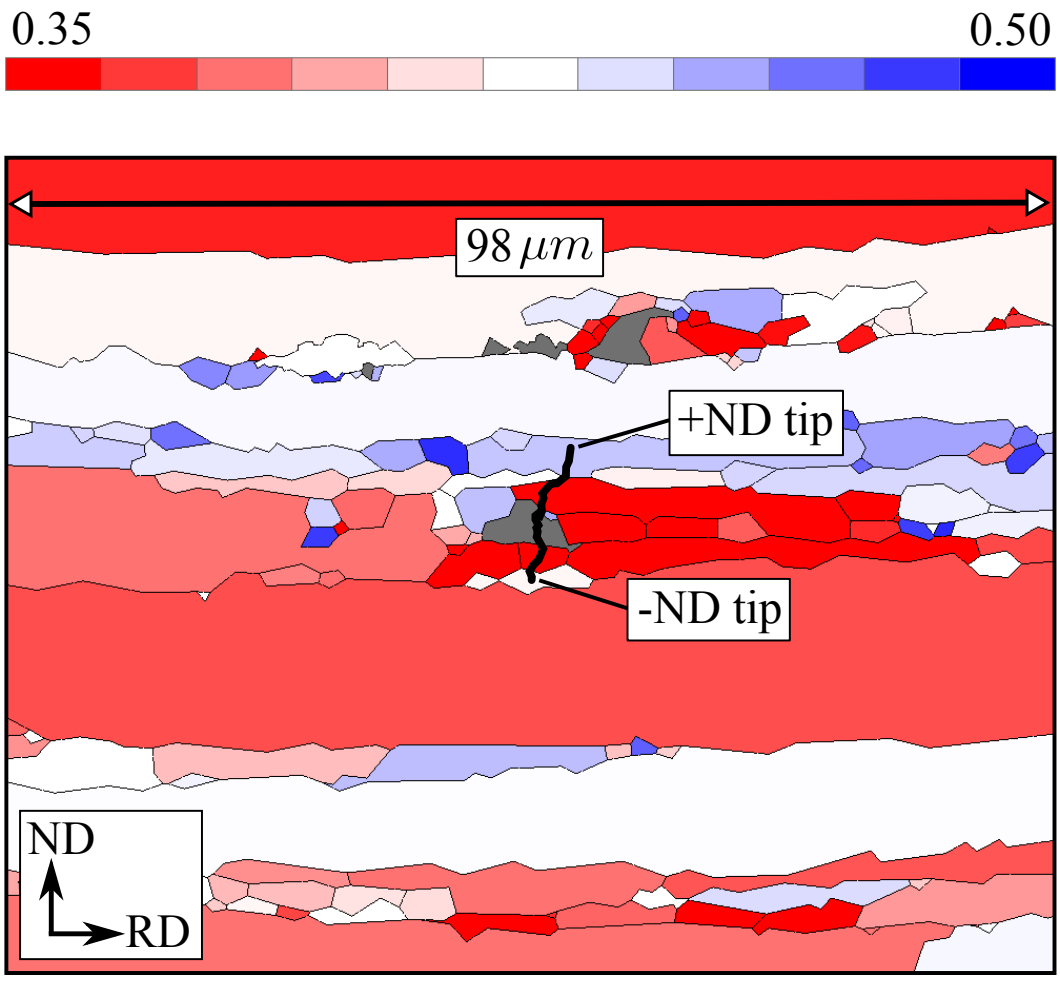

Figure 3.11: Second highest Schmid factor plot of texture in MSFC observation region P91. The shape of the MSFC after 3000 load cycles is sketched.

that interval is recorded as,

$$\frac{\Delta a}{\Delta N} = \frac{a_n - a_{n-1}}{N_n - N_{n-1}} \tag{3.5}$$

Therefore, $\frac{\Delta a}{\Delta N}$ is an estimate of the forward-looking crack growth rate at cycle N_{n-1} or the backward-looking crack growth rate at cycle N_n. The recorded lengths of the crack crack paths at step N_n, $2(a_n)$, are accurate within approximately 0.25 μm.

A comparison of the results in this table to prior observations reveals that trends

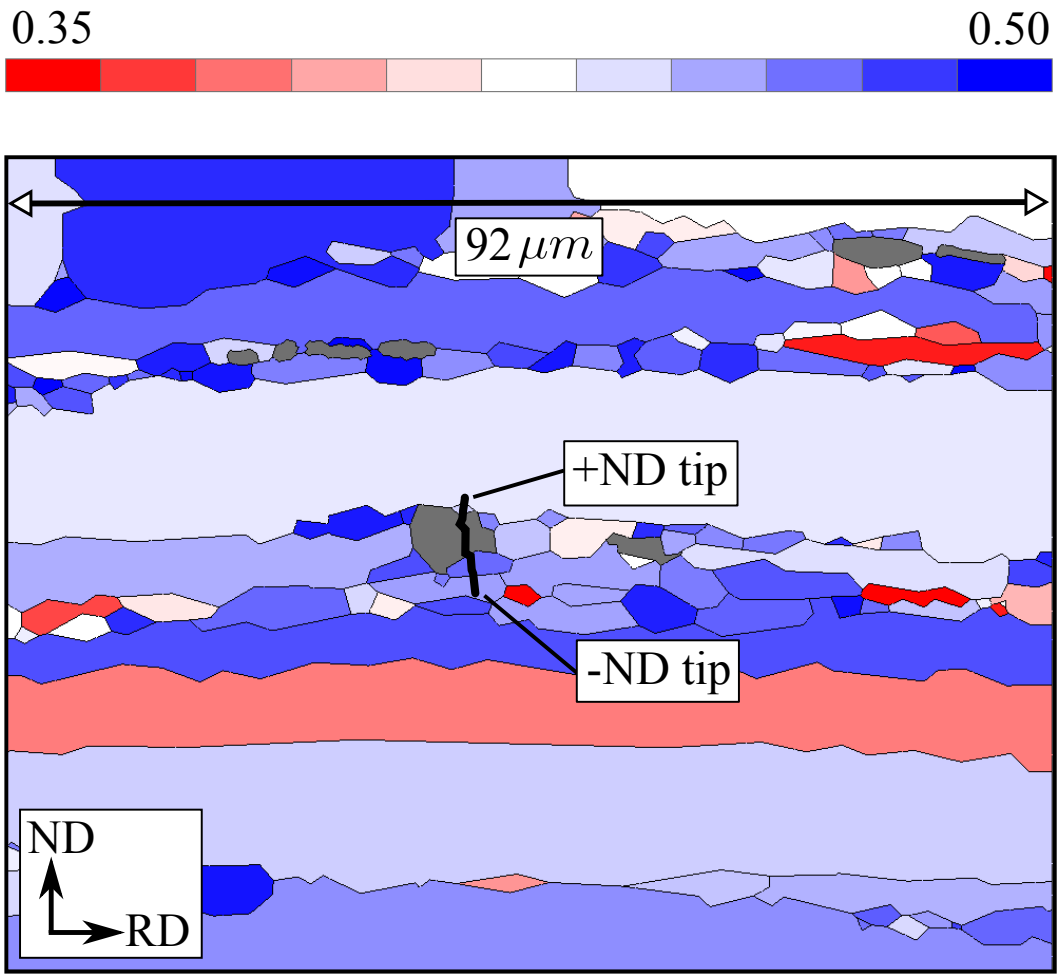

Figure 3.12: Highest Schmid factor plot of texture in MSFC observation region P208. The shape of the MSFC after 3000 load cycles is sketched.

in MSFC propagation rate are likely dependent on microstructural heterogeneities. The MSFC in P91 grows significantly faster than the other observed cracks immediately following nucleation. This is likely because, as shown in Figure 3.7, the +ND tip of the crack grows very close to a particle notch after nucleation; the close proximity of the particle likely acts to increase the local driving forces on the crack, because the particle is much more stiff than the surrounding grains. Additionally, the strong orientation grains immediately surrounding this MSFC at nucleation, as shown in Figure 3.10, are likely facilitating high driving forces. The subsequent

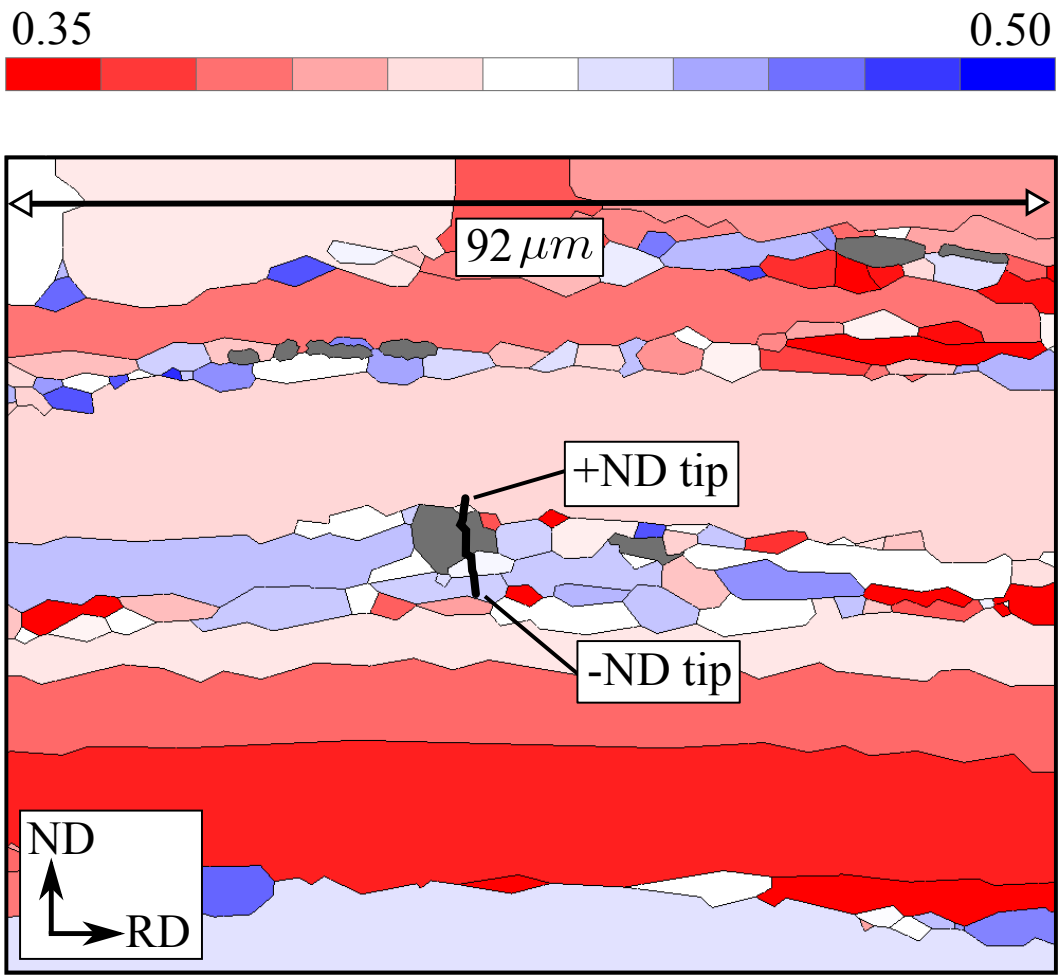

Figure 3.13: Second highest Schmid factor plot of texture in MSFC observation region P208. The shape of the MSFC after 3000 load cycles is sketched.

substantial decrease in MSFC propagation rate for this crack was observed to be coincident with the +ND and -ND crack tips approaching weak grains. The +ND tip eventually navigated around the weak grain and into a rotated grain, where propagation then commenced at a moderate rate from cycle 1000 to 3000. However, the -ND tip propagated a significantly shorter distance by cycle 3000 than the +ND tip, possibly because the only viable propagation path was through the weak grain. That is, weak grains appear to cause significant decreases in MSFC propagation rate, despite the crack being larger on arrival in them. This is sup-

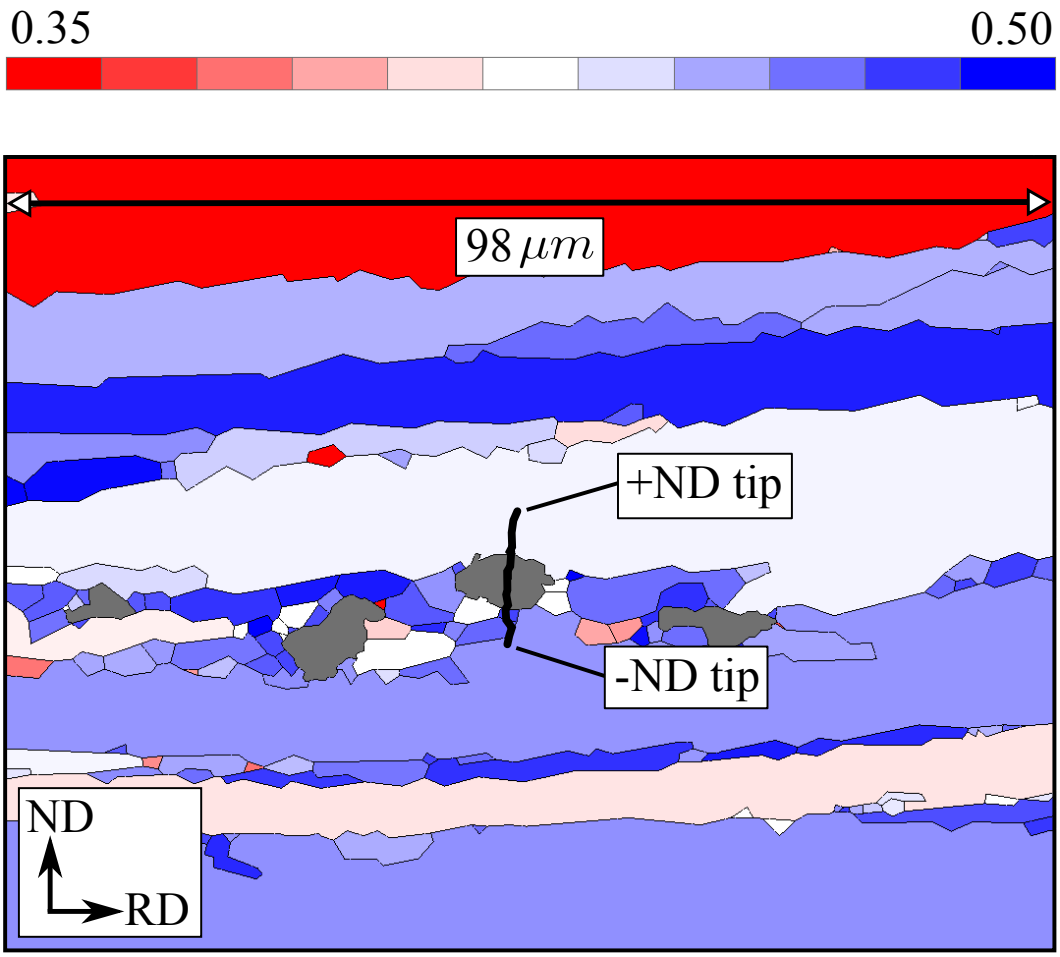

Figure 3.14: Highest Schmid factor plot of texture in MSFC observation region P124. The shape of the MSFC after 3000 load cycles is sketched.

ported mechanistically by simulations from Veilleux *et al.* [82], which showed that weak grains prevent cyclic slip accumulation. Therefore, it is hypothesized that an MSFC will propagate beyond a weak grain only when the driving forces are sufficiently high or when an alternate path, *e.g.* a grain or subgrain boundary, has lower fracture toughness than the grain, thus allowing for the crack to navigate around the weak grain.

The slow MSFC propagation rate in P187 also appears to have been due to interaction with a weak grain. Figure 3.8 and Figure 3.9 show that the +ND

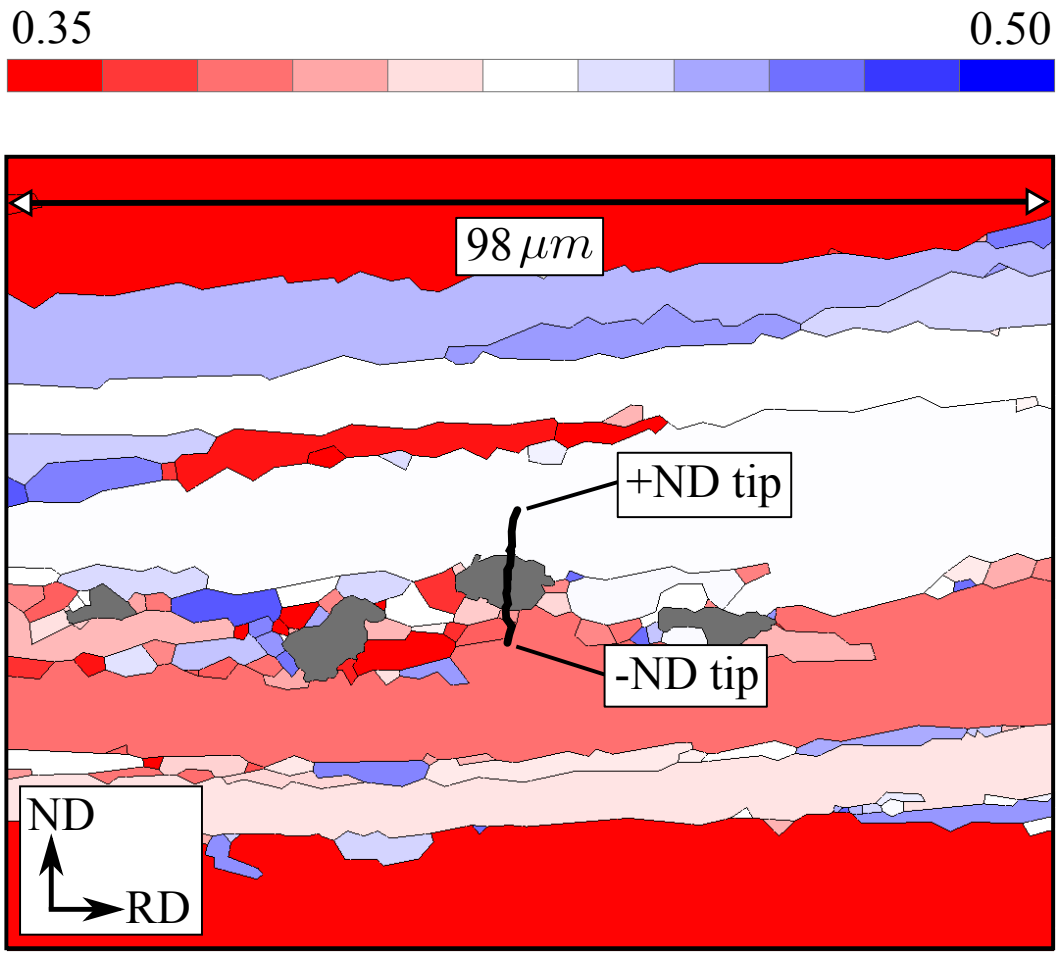

Figure 3.15: Second highest Schmid factor plot of texture in MSFC observation region P124. The shape of the MSFC after 3000 load cycles is sketched.

tip of this MSFC only propagated a short distance, approximately 50% of the particle diameter into a weak grain. Interestingly, 50% of the particle diameter was previously found to be the lower limit on the size of the particle micro-notch root influence region [82]. Possibly, the +ND tip of the MSFC in P187 arrested once the particle notch root influence was no longer sufficient to drive propagation, and subsequent propagation would only occur at the +ND tip if other portions of the crack grew large enough to sufficiently increase the local driving force.

Orientations of the grains immediately neighboring an incubated MSFC also

Table 3.1: Recorded propagation rates of 4 previously nucleated microstructurally small fatigue cracks. Rates are determined from high resolution microscopic images taken at 30, 100, 300, 1000, and 3000 load cycles. Observation data interpreted for this table were provided by Northrop Grumman Corporation.

observation region	a_{n-1} [μm]	a_n [μm]	N_{n-1} [cycles]	N_n [cycles]	$\frac{\Delta a}{\Delta N}$ [10^{-3} μm/cycle]
P187	2.00	2.00	30	100	0.00
	2.00	2.13	100	300	0.65
	2.13	3.13	300	1000	1.43
	3.13	4.13	1000	3000	0.50
P91	2.00	3.00	30	100	14.29
	3.00	3.75	100	300	3.75
	3.75	5.13	300	1000	1.97
	5.13	7.75	1000	3000	1.31
P208	2.50	5.25	1000	3000	1.38
P124	3.63	4.00	300	1000	0.53
	4.00	7.50	1000	3000	1.75

indicate a trend in the number of cycles to nucleation that agrees with previous findings from Veilleux *et al.* [82] and Hochhalter *et al.* [32]. The strong grain orientations, which were found by Veilleux *et al.* to cause the highest stresses near an MSFC, are the most prominent near the two cracks that nucleated the earliest, *i.e.* the cracks in observation regions P91 and P187. Furthermore, Hochhalter *et al.* found that high stress ahead of an incubated MSFC often indicates fewer cycles to nucleation, because less irreversible slip accumulation is required to reach the semi-empirical fracture envelope in their proposed stress-versus-slip plot. Therefore,

further investigations of MSFC nucleation are recommended to determine whether texture is the primary indicator of the cycles to nucleation.

The two observed MSFC's propagating the fastest from cycle 1000 to 3000, *i.e.* the cracks in observation regions P208 and P124, also have microstructural features likely contributing to their faster propagation rates. The MSFC in P208, Figure 3.5, Figure 3.12, and Figure 3.13, does not nucleate until cycle 1000, so the faster propagation rate from then to cycle 3000 is likely caused by this crack being the most influenced by the stress localization of the particle over this cycle interval. The -ND tip of this same MSFC nucleates into and propagates through a weak grain, so it is assumed that the particle influence provides sufficient driving forces to cause propagation through this unfavorable orientation. The +ND tip does not propagate that far through a large, moderately weak grain, so either grain size augments the crack deceleration effects of a weak grain or the driving forces are lower on this side of the crack. Interestingly, the fastest propagating MSFC, Figure 3.6, Figure 3.14, and Figure 3.15, is able to navigate around weak grains immediately following nucleation. The -ND tip of this crack in observation region P124 initially encounters three weak grains, but there appear to be preferentially aligned grain boundaries allowing the crack to navigate along them and around the weak grains. This tip appears to nucleate through a weak grain in Figure 3.14 and Figure 3.15, but further investigation of the texture surrounding this grain in Section 3.3 reveals that nucleation on this side of the particle is actually along a sub-grain boundary. By cycle 300, however, the -ND tip has not propagated as far as the +ND tip, seemingly because the -ND tip is propagating into a large, weak grain. Meanwhile, the +ND tip propagates at a steady, moderate rate through a rotated grain. Therefore, it is assumed that rotated grains allow for faster MSFC propagation than weak grains. This is supported by previous findings that rotated

grains allow for much more cyclic slip accumulation than the negligible accumulation in weak grains [82].

In summary, the 4 MSFC observations investigated here suggest the following dependencies of MSFC propagation on microstructural heterogeneities:

- The crack propagation direction is in Stage II, but grain textures and grain boundaries cause local deviations from a Mode I MLFC trajectory.
- A crack approaching a grain boundary closely aligned with the MSFC propagation direction will temporarily propagate intergranularly along that grain boundary.
- Intergranular propagation is most frequent when alternative crack paths are through a grain with one high Schmid factor.
- Grains with no high Schmid factors and grains with multiple high Schmid factors facilitate higher rates of MSFC propagation than grains with one high Schmid factor.
- The slowest MSFC propagation rates occur when an MSFC is propagating through a large grain with one high Schmid factor.

3.3 Replicated-microstructure simulation of an MSFC immediately following nucleation

Results are detailed here for a finite element simulation performed on a digital replication of the MSFC and microstructure in observation region P124. The main objective is to evaluate whether crack displacements, slips, and stresses near the

crack front provide effective metrics for predicting MSFC propagation direction and rate. Furthermore, the dependence of MSFC propagation and these metrics on microstructural heterogeneities are further evaluated and compared to prior findings in Section 3.2 and by Veilleux *et al.* [82]. The finite element model of the grains and particles in observation region P124 was previously generated by Hochhalter *et al.* [32], and the reader is referred to this paper for a description of the model generation process. In that study, however, the crack was only extended to the particle-grain interface to simulate MSFC behavior leading to nucleation. Here, MSFC behavior immediately subsequent to nucleation is simulated; therefore, the crack is extended approximately 1 μm beyond the particle-grain interface, as shown in Figure 3.16. The simulated crack approximates the size and shape of the crack observed at the 1000^{th} load cycle, which is sketched onto an OIM in Figure 3.17. The MSFC propagation trajectory after this simulated load cycle is also sketched in this OIM for reference in the following sections, wherein the simulated field metrics are compared to the observed crack trajectory from the 1000^{th} to 3000^{th} load cycles.

Due to the computational demand of modeling all 1000 load cycles, the crack in Figure 3.16 is simulated as stationary during 3 load cycles. From scoping studies performed prior to this study, it was determined that the mesh density required for convergence of near crack fields in this study consumes $O(10^4)$ CPU hours of run-time per load cycle on the Pleiades supercomputer at the NASA Ames research center. This is computationally tractable to thousands of load cycles for one model, but the CPU resource requirement is deemed unreasonable and unnecessary for this study. By the same arguments given for the baseline MSFC propagation simulations [82], ΔCTD computed for a stationary MSFC model should be a sufficient approximation of the ΔCTD for a propagating MSFC, but the actual stress and

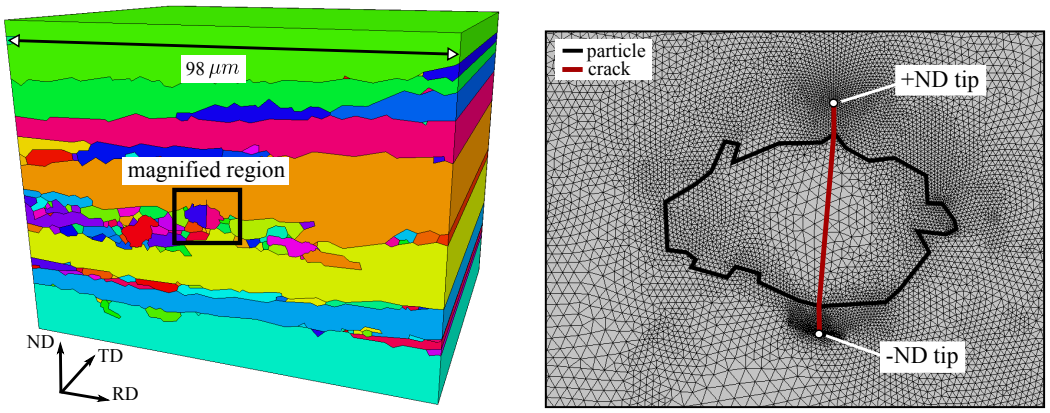

(a) (b)

Figure 3.16: Replication finite element model of the experimentally observed crack propagating from the particle in observation region P124: (a) perspective view; and, (b) magnified view of the particle, crack, and the two crack front endpoints on the observation surface, the '+ND tip' and '-ND tip'.

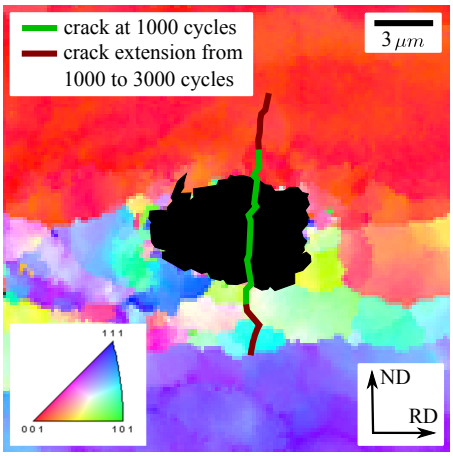

Figure 3.17: Inverse pole figure showing the texture surrounding the MSFC in observation region P124. Image courtesy of Northrop Grumman Corporation.

slip states simulated for a stationary MSFC are likely significantly different from a propagating MSFC. However, the intentions of this study - to begin to understand the dependence of MSFC propagation rate and direction on microstructural heterogeneities and to evaluate whether microstructure-dependent field metrics can be used to predict MSFC propagation behavior - can be satisfied by modeling a stationary crack. Nonetheless, future studies are recommended to evaluate how accurate simulation of MSFC evolution over thousands of load cycles changes results from those given here.

Finite element simulations of the stresses, slips, and crack displacements near the +ND and -ND crack tips are presented and critically evaluated in Section 3.3.1, Section 3.3.2, and Section 3.3.3, respectively.

3.3.1 Maximum tangential stress magnitude and direction

The simulated stresses at the second load peak for P124, Figure 3.18, reveal direct relationships to the observed textures, in Figure 3.14, Figure 3.15, and Figure 3.17, and the observed MSFC propagation direction, *e.g.* Figure 3.6. The simulated crack, outlined in green in Figure 3.18, extends to a grain boundary at the -ND crack tip and approximately 1.5 μm into a large grain adjacent to the particle at the +ND crack tip. The Schmid factor plots and inverse pole figure for this observation region show that the -ND tip has actually propagated between two small, weak subgrains and this crack tip is now at the grain boundary with another small, weak grain. The +ND tip is in a rotated grain with two moderately high Schmid factors (approximately 0.43). The values of $\sigma_{\theta\theta}^{max}$ measured along non-local arcs 1 μm ahead of the -ND and +ND crack tips are 610 MPa and 520 MPa, respectively. This agrees with prior findings by Veilleux *et al.* [82] that

an MSFC in a weak orientation grain will have $\sigma_{\theta\theta}^{max}$ significantly higher than an MSFC in a rotated orientation grain. Figure 3.18(b) also shows the direction of propagation and the direction normal to $\sigma_{\theta\theta}^{max}$ at the two crack tips. When there are no grain boundaries near the crack tip, *i.e.* at the +ND crack tip, the direction of propagation aligns approximately normal to $\sigma_{\theta\theta}^{max}$, which again supports the theory that an intragranular MSFC nucleates and propagates in Stage II. However, the grain boundaries near the -ND crack tip appear to be a direction of less resistance than the weak grain, thus causing the crack to take a path that deviates from the direction normal to $\sigma_{\theta\theta}^{max}$. However, Figure 3.18(b) shows that the direction taken is still within a lobe of higher stress than most other directions ahead of the -ND crack tip.

3.3.2 Magnitude and cyclic change of irreversible slip

Contours of the simulated irreversible slip metric D_3 at the second load peak for P124, Figure 3.19, also reveal direct relationships with the observed microstructure and MSFC propagation characteristics in Figure 3.6, Figure 3.14, Figure 3.15, and Figure 3.17. The simulated crack is again outlined in green in Figure 3.19 to emphasize the location of the +ND and -ND crack tips in relation to microstructural features and the slip localizations. A view of the slip accumulation on the entire replicated surface containing the crack, Figure 3.19(a), shows that the crack-induced slip localizations extend well beyond the particle, into neighboring grains not containing the crack. As expected, two large slip localization lobes extend from the +ND crack tip since this end of the crack is in a grain with two high Schmid factors, and one large localization lobe extends from the -ND crack tip since this end of the crack is encountering multiple grains with one high Schmid

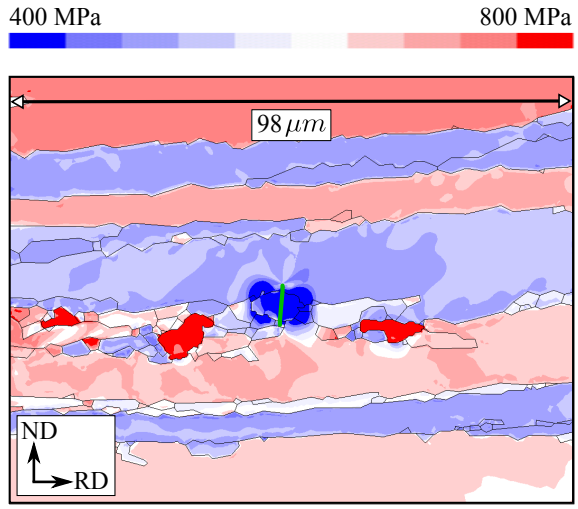

(a)

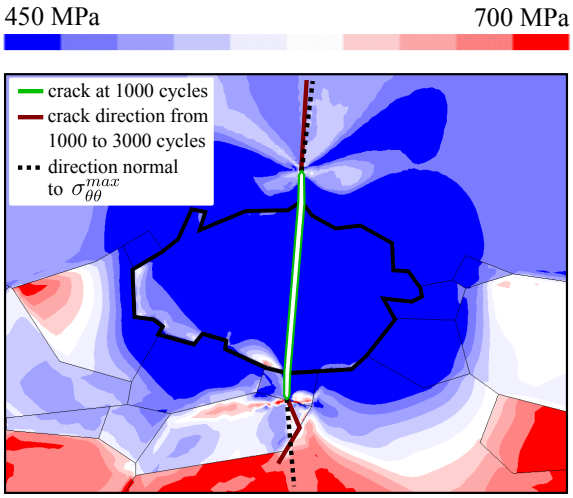

(b)

Figure 3.18: Maximum principal stress, σ_1, contours at the second load peak for the nucleated crack in observation region P124: (a) view of the RD-ND surface containing the particle and crack; and, (b) magnified view on this surface of the particle and crack. The ranges of stresses were set differently when plotting (a) and (b) to best show variations in stresses throughout the model and near the crack, respectively. However, the same computed fields were used to create both plots.

factor. Also, since the -ND crack tip is encountering multiple small grains and grain boundaries, the slip localization very close to the crack tip, Figure 3.19(b), is more diffuse, likely due to slip buildup at the grain boundaries. The values of D_3^{avg}, measured again along non-local arcs 1 μm ahead of the -ND and +ND crack tips, are 0.058 and 0.044, respectively, at the second load peak. The values of ΔD_3^{avg} from the second to third load peaks are 0.013 and 0.006, respectively. Interestingly, these results disagree with findings from Veilleux *et al.* [82], which showed that cracks in weak grains, *i.e.* the -ND crack tip, have negligible slip accumulation. However, this prior study did not investigate slip accumulation in small grains with complex grain boundary networks like those present in P124. Apparently, the misorientations at grain boundaries act to magnify slip accumulation, which agrees with observations showing that the -ND crack tip does indeed propagate along these grain boundaries. Therefore, it is theorized that slip pileup acts to decrease the fracture toughnesses along grain boundaries, so if the normal stresses are also high toward and along one such grain boundary, such as is observed in Figure 3.18(b), then the MSFC will propagate in that direction.

3.3.3 Cyclic change in crack tip displacement

Computed values of ΔCTD from the second to third load peaks for the simulated MSFC in P124 are given in Table 3.2. These ΔCTD values were computed 1 μm behind the -ND and +ND crack tips shown in Figure 3.16. The previously presented $\sigma_{\theta\theta}^{max}$ and D_3^{avg} values at the second load peak, ΔD_3^{avg} from the second to third load peaks, and the observed propagation rate from cycle 1000 to cycle 3000 are also included in this table to show trends among the computed near-crack field metrics and the recorded propagation rate. The propagation rate at each crack tip

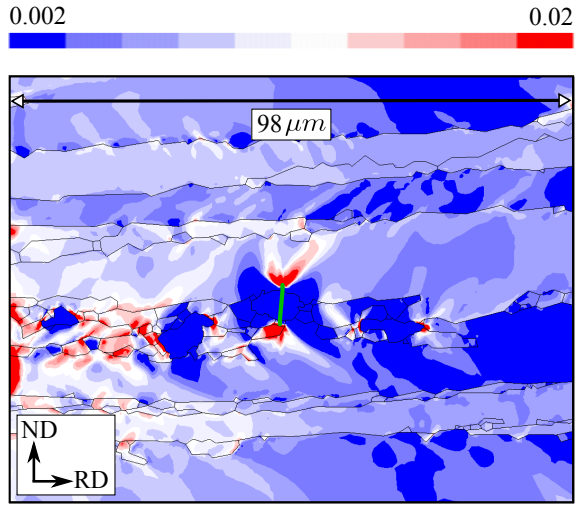

(a)

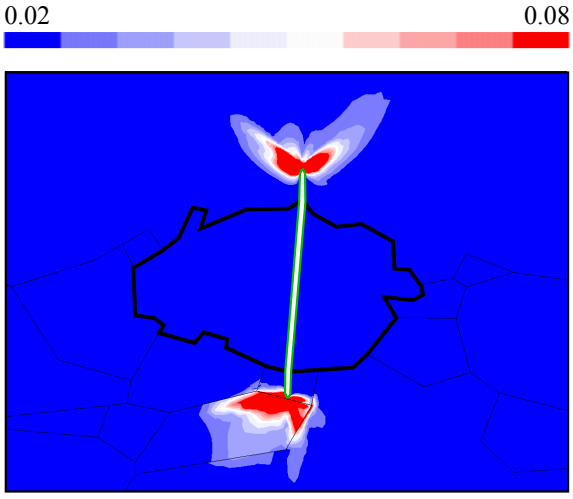

(b)

Figure 3.19: Irreversible slip metric D_3 contours at the second load peak for the nucleated MSFC in observation region P124: (a) view of the RD-ND surface containing the particle and crack; and, (b) magnified view on this surface of the particle and crack. The ranges of D_3 were set differently when plotting (a) and (b) to best show the lengths and intensities, respectively, of the crack-induced slip localization lobes. However, the same computed fields were used to create both plots.

Table 3.2: Computed field metrics for the MSFC length observed at the 1000^{th} load cycle in P124, and the observed propagation rates of the two observed crack tips between the 1000^{th} and 3000^{th} load cycles.

crack tip	ΔCTD [μm]	$\sigma_{\theta\theta}^{max}$ [MPa]	D_3^{avg}	ΔD_3^{avg}	$\frac{\Delta a}{\Delta N}$ [μm/cycle]
-ND	0.094	610	0.058	0.013	0.00188
+ND	0.088	520	0.044	0.006	0.00163

was measured from high resolution SEM images taken at the 1000^{th} and 3000^{th} load cycles. The computed ΔCTD values, 0.094 μm at the -ND crack tip and 0.088 μm at the +ND crack tip, varied by less than 0.5% from the second to third load peaks, so cyclic change in ΔCTD is assumed to be negligible for a stationary MSFC. Similar percent changes in $\sigma_{\theta\theta}^{max}$ were computed from the second to third load peaks, so the only values having substantial cyclic variation are the slip-based metric values, D_3^{avg}. For this sample size of two crack tips, it appears that $\frac{\Delta a}{\Delta N}$ follows the trends in all three metrics, ΔCTD, $\sigma_{\theta\theta}^{max}$, and D_3^{avg}. Therefore, more simulations of digitally replicated observations are recommended to formulate and calibrate semi-empirical MSFC propagation formulas from these metrics, like those formulated by Hochhalter *et al.* [32] for MSFC nucleation.

However, the common $\frac{da}{dN}$ versus ΔCTD formula in the MSFC literature, Equation 3.3, does have a consistent value of the linear constant, G, for the two crack tips observed and simulated in this study. Since ΔCTD_{TH} is on the order of the Burgers vector [49, 51, 88], and this is two orders of magnitude less than the computed ΔCTD values in Table 3.2, the MSFC in P124 is far above the propagation

threshhold. Furthermore, Equation 3.3 reduces to

$$\frac{da}{dN} = G(\Delta CTD). \tag{3.6}$$

Solving this equation for G with the two pairs of ΔCTD and $\frac{\Delta a}{\Delta N}$ values in Table 3.2 gives $G = 0.02$ at both observed crack tips. This is one order of magnitude lower than the values of G used by others who have simulated MSFC propagation in AA7075-T651 [88]. Therefore, either the observation simulated here is a significant exception or the values of G previously used in MSFC simulations need to be revisited. McClintock [49] showed that G of an MSFC is dependent on load magnitudes and ratios, and ΔCTD of MSFC's in high strength alloys can be much higher than in other alloys. The results in these papers certainly suggest G is relatively low and ΔCTD is relatively high in AA7075-T651 at R=0.1 and 1% maximum strain (*i.e.* large-scale yielding), but more simulations of MSFC's replicated from observations are recommended to validate these findings.

3.4 Summary and future work

The research presented in this paper investigated microstructurally small fatigue crack (MSFC) propagation dependence on microstructural heterogeneities in AA7075-T651, and whether microstructure-dependent crack displacement, irreversible slip, and stress metrics near the crack front of a stationary MSFC relate to observed MSFC propagation characteristics immediately subsequent to nucleation. From observations of 4 nucleated MSFC's over thousands of high strain load cycles, it was theorized that:

- The crack propagation direction is in Stage II, but grains and grain boundaries cause local deviations from a Mode I microstructurally large fatigue

crack (MLFC) trajectory;

- A crack approaching a grain boundary closely aligned with the MSFC propagation direction will temporarily propagate intergranularly along that grain boundary;
- Intergranular propagation is most frequent when all other possible crack paths are through a grain with one high Schmid factor;
- Grains with no high Schmid factors and grains with multiple high Schmid factors facilitate higher rates of MSFC propagation than grains with one high Schmid factor; and,
- The slowest MSFC propagation rates occur when an MSFC is propagating through a large grain with one high Schmid factor.

More observations are recommended to further validate these theories and determine which microstructural features cause the fastest MSFC propagation rates.

From one simulation of a finite element model replication of an experimentally observed MSFC, it was found that:

- Intragranular MSFC propagation was in the direction normal to maximum tangential stress ahead of the crack;
- Intergranular MSFC propagation occurred when: a grain boundary ahead of the crack was aligned closely with the MSFC propagation direction, slip localized at this grain boundary, and this grain boundary was in a region of high tangential stress ahead of the crack; and,
- The constant G, *i.e.* the ratio of $\frac{da}{dN}$ to ΔCTD, was equal to approximately 0.02 at the two simulated crack front points.

More simulations are recommended to:

- Determine whether slip and stress metrics also relate to the transition from intergranular propagation to transgranular propagation;
- Determine whether semi-empirical models of intergranular and transgranular propagation direction can be formulated from the near-crack stress and slip localization metrics; and,
- Continue to calibrate and validate a constant G in Equation 3.3 for modeling MSFC propagation rate.

In conclusion, this paper has contributed to the geometrically explicit MSFC simulation approach being developed in this series of papers by revealing prominent microstructural features influencing MSFC propagation characteristics immediately subsequent to nucleation and showing how MSFC-dependent metrics indicate these characteristics.

ACKNOWLEDGEMENTS

Dr. Gerd Heber developed the parallel finite element code that was used for the finite element simulations presented here. The crystal plasticity model was implemented by Dr. Antoinette Maniatty, Dr. David Littlewood, and Dr. Paul Wawrzynek. Experimental observations were made by Joel Payne and Dr. Elias Anagnostou at the Northrop Grumman Corporation. This work is sponsored by the Defense Advanced Research Projects Agency under contract HR0011-04-C-0003 with Dr. Leo Christodoulou as the DARPA Program Manager. This work is also funded by NASA under contract ARMD-NNX07AB69A with Dr. Ed Glaessgen as the NASA Contract Monitor, and by the U.S. Department of Energy Computational Science Graduate Fellowship Program of the Office of Science and National Nuclear Security Administration in the Department of Energy under contract DE-FG02-97ER25308. The simulations needed to complete this study were carried out on a NASA AMES supercomputer, Pleiades.

APPENDIX A

CRYSTAL PLASTICITY CONSTITUTIVE MODEL

The implemented crystal plasticity constitutive model for this study is described by Matous and Maniatty [48]. The model is elasto-viscoplastic with various hardening rules and material parameters. For AA7075-T651, precipitation hardening is applied to represent the strong self-hardening typical of Orowan looping evident in this material. The material parameters in Table A.1 are applied in the following formulation. For a more complete description of the implementation of this model for AA7075-T651, the reader is referred to [7].

The deformation response is assumed to follow a multiplicative decomposition, with elastic lattice deformation and volume-preserving viscoplastic slip along crystallographic slip systems,

$$F = F^e F^p, \tag{A.1}$$

$$det(F^p) = 1, \tag{A.2}$$

$$L = \dot{F}^p F^{e^{-1}} + F^e \hat{L}^p F^{e^{-1}}, \tag{A.3}$$

$$\hat{L}^p = \dot{F}^p F^{p^{-1}} = \sum_{\alpha=1}^{N_s} \dot{\gamma}^\alpha P^\alpha, \tag{A.4}$$

$$P^\alpha = s^\alpha \otimes m^\alpha, \tag{A.5}$$

where F^e is the elastic deformation gradient, F^p is the plastic deformation gradient, L is the velocity gradient, $\hat{L}^p$ is the plastic velocity gradient in the relaxed, intermediate configuration, $\dot{\gamma}^\alpha$ is the shear rate on slip system α, N_s is the number of slip systems (12 for FCC), s^α is the slip direction of slip system α, m^α is the normal of the slip plane containing slip system α, and $\otimes$ symbolizes dyadic product. P^α is the Schmid tensor for slip system α.

Table A.1: Crystal plasticity parameters for AA7075-T651, from [7].

parameter	value
m	0.005
g_0	220 MPa
$\dot{\gamma}_0$	1.0 s^{-1}
G_0	120 MPa
g_s	250 MPa
μ	28300 MPa
λ	60900 MPa
η	5100 MPa

The elastic response is assumed by a linear relationship with cubic symmetry between the second Piola-Kirchhoff stress, $\hat{S}$, and the Green elastic strain, $\hat{E}^e$,

$$\hat{S} = \det\left(F^e\right) F^{e^{-1}} \sigma F^{e^{-T}} = \hat{C} : \hat{E}^e = 2\mu\hat{E}^e + \lambda tr\left(\hat{E}^e\right) I - 2\eta\Xi : \hat{E}^e, \tag{A.6}$$

$$\hat{E}^e = \frac{1}{2}\left(F^{e^T} F^e - I\right), \tag{A.7}$$

where σ is the Cauchy stress, $\hat{C}$ is the fourth-order elasticity tensor, I is the second-order identity tensor, Ξ is a fourth order tensor defined, with respect to the lattice coordinates, as

$$\Xi_{\hat{i}\hat{j}\hat{k}\hat{l}} = 1 \quad \text{if} \quad \hat{i} = \hat{j} = \hat{k} = \hat{l}; \quad \Xi_{\hat{i}\hat{j}\hat{k}\hat{l}} = 1 \quad \text{otherwise}, \tag{A.8}$$

where the hat indices indicate the lattice configuration. μ, λ, and η are elasticity parameters related to the stiffness matrix: $\mu = C_{44}$, $\lambda = C_{12}$, and $2\eta = 2C_{44} + C_{12} - C_{11}$.

The plastic deformation is governed by the rates of slip, $\dot{\gamma}^\alpha$, on each primary slip system, α, where $\dot{\gamma}^\alpha$ is defined by a power relationship,

$$\dot{\gamma}^\alpha = \dot{\gamma}_0 \frac{\tau^\alpha}{g^\alpha} \left| \frac{\tau^\alpha}{g^\alpha} \right|^{\frac{1}{m-1}}, \tag{A.9}$$

$$\tau^\alpha = \left(F^{e^T} F^e \hat{S} \right) : P^\alpha, \tag{A.10}$$

$$\dot{g}^\alpha = G_0 \left(\frac{g_s - g^\alpha}{g_s - g_0} \right) \sum_{\beta=1}^{N_s} H^{\alpha\beta} \left| \dot{\gamma}^\beta \right|, \tag{A.11}$$

where $\dot{\gamma}_0$ is a reference shear rate parameter, m is a strain rate sensitivity parameter, g^α is the resistance to slip on system α that evolves by $\dot{g}^\alpha$, τ^α is the resolved shear stress on slip system α, g_0 is an initial slip resistance parameter, g_s is the saturation hardening, G_0 is a hardening rate parameter, and $H^{\alpha\beta}$ is a slip interaction matrix defining the relative strengths of self-hardening and latent-hardening on the slip systems. For all values of $H^{\alpha\beta}$, and justification thereof, the reader is referred to [7]. The hardening mechanism for AA7075-T651, and modeled here, is precipitation hardening.

BIBLIOGRAPHY

[1] M Anahid, P Chakraborty, D S Joseph, and S Ghosh. Wavelet decomposed dual-time scale crystal plasticity fe model for analyzing cyclic deformation induced crack nucleation in polycrystals. *Modelling and Simulation in Materials Science and Engineering*, 17(6), 2009.

[2] Z P Bazant and S-D Pang. Mechanics-based statistics of failure risk of quasibrittle structures and size effect on safety factors. *Proceedings of the National Academy of Sciences of the United States of America*, 103(25):9434–9439, 2006.

[3] V P Bennett and D L McDowell. Cyclic crystal plasticity analyses of stationary, microstructurally small surface cracks in ductile single phase polycrystals. *Fatigue and Fracture of Engineering Materials and Structures*, 25(7):677–693, 2002.

[4] M Bernacki, H Resk, T Coupez, and R E Loge. Finite element model of primary recrystallization in polycrystalline aggregates using a level set framework. *Modelling and Simulation in Materials Science and Engineering*, 17(6), 2009.

[5] Y Bhandari, S Sarkar, M Groeber, M D Uchic, D M Dimiduk, and S Ghosh. 3D polycrystalline microstructure reconstruction from FIB generated serial sections for FE analysis. *Computational Materials Science*, 41(2):222–235, 2007.

[6] D Boltcheva, M Yvinec, and J-D Boissonnat. Mesh generation from 3D multimaterial images. In *Medical Image Computing and Computer-Assisted Intervention, MICCAI 2009*, pages 283–290. Springer-Verlag, Berlin, 2009.

[7] J E Bozek, J D Hochhalter, M G Veilleux, M Liu, G Heber, S D Sintay, A D Rollett, D J Littlewood, A M Maniatty, H Weiland, R J Christ Jr, J Payne, G Welsh, D G Harlow, P A Wawrzynek, and A R Ingraffea. A geometric approach to modeling microstructurally small fatigue crack formation: I. Probabilistic simulation of constituent particle cracking in AA 7075-T651. *Modelling and Simulation in Materials Science and Engineering*, 16(6), 2008.

[8] A Brahme, M H Alvi, D Saylor, J Fridy, and A D Rollett. 3D reconstruction of microstructure in a commercial purity aluminum. *Scripta Materialia*, 55(1):75–80, 2006.

[9] A Brahme, J Fridy, and A D Rollett. Modeling recrystallization in aluminum using input from experimental observations. In *Materials Science Forum*, volume 558-559, pages 1057–1061, Switzerland, 2007. Trans Tech Publications Ltd.

[10] J R Brockenbrough, A J Hinkle, P E Magnusen, and R J Bucci. Microstructurally based model of fatigue and growth. In C E Harris, editor, *Proceedings, FAA/NASA International Symposium on Advanced Structural Integrity Methods for Airframe Durability and Damage Tolerance*, volume NASA Conference Publication 3274, Part I, pages 71–84, Hampton, VA, September 1994.

[11] R M Campman. Statistical analysis of second phase particles in AA7075-T651. Master's thesis, Carnegie Mellon University, 2005.

[12] J B Cavalcante-Neto, L F Martha, P A Wawrzynek, and A R Ingraffea. A back-tracking procedure for optimization of simplex meshes. *Communications in Numerical Methods in Engineering*, 21(12):711 – 722, 2005.

[13] K-S Cheong and E P Busso. Effects of lattice misorientations on strain heterogeneities in FCC polycrystals. *Journal of the Mechanics and Physics of Solids*, 54(4):671 – 689, 2006.

[14] L Christodoulou and J M Larsen. Using materials prognosis to maximize the utilization potential of complex mechanical systems. *Journal of the Minerals, Metals and Materials Society*, 56(3):15–19, 2004.

[15] S E Dillard, J F Bingert, D Thoma, and B Hamann. Construction of simplified boundary surfaces from serial-sectioned metal micrographs. *IEEE Transactions on Visualization and Computer Graphics*, 13(6):1528–1535, 2007.

[16] J M Emery, J D Hochhalter, P A Wawrzynek, G Heber, and A R Ingraffea. DDSim: A hierarchical, probabilistic, multiscale damage and durability simulation system - Part I: Methodology and Level I. *Engineering Fracture Mechanics*, 76(10):1500 – 1530, 2009.

[17] J Fan, D L McDowell, M F Horstemeyer, and K Gall. Computational micromechanics analysis of cyclic crack-tip behavior for microstructurally small cracks in dual-phase Al-Si alloys. *Engineering Fracture Mechanics*, 68(15):1687 – 1706, 2001.

[18] A Fatemi and D F Socie. A critical plane approach to multiaxial fatigue damage including out-of-phase loading. *Fatigue and Fracture of Engineering Materials and Structures*, 11(3):149–165, 1988.

[19] S Flouriot, S Forest, G Cailletaud, A Koster, L Remy, B Burgardt, V Gros, S Mosset, and J Delautre. Strain localization at the crack tip in single crystal CT specimens under monotonous loading: 3D finite element analyses and application to nickel-base superalloys. *International Journal of Fracture*, 124(1):43 – 77, 2003.

[20] P J E Forsyth. A two stage process of fatigue crack growth. In *Proceedings, Crack Propagation Symposium*, Cranfield, 1961.

[21] L A Freitag and P M Knupp. Tetrahedral mesh improvement via optimization of the element condition number. *International Journal for Numerical Methods in Engineering*, 53(6):1377 – 1391, 2002.

[22] Y X Gao, J Z Li, P D Lee, and T C Lindley. The effects of porosity on the fatigue life of cast aluminum-silicon alloys. *Fatigue and Fracture of Engineering Materials and Structures*, 27(1):559–570, 2004.

[23] S Ghosh, Y Bhandari, and M Groeber. CAD-based reconstruction from 3D polycrystalline alloy microstructures from FIB generated serial sections. *Computer-Aided Design*, 40(3):293–310, 2008.

[24] S Ghosh, D M Valiveti, C Hu, and J Bai. A multiscale framework for characterization and modeling ductile fracture in heterogeneous aluminum alloys. *Journal of Multiscale Modelling*, 1(1):21–55, 2009.

[25] M Groeber, S Ghosh, M D Uchic, and D M Dimiduk. A framework for automated analysis and simulation of 3D polycrystalline microstructures. Part I: Statistical characterization. *Acta Materialia*, 56(6):1257–1273, 2008.

[26] M Groeber, S Ghosh, M D Uchic, and D M Dimiduk. A framework for automated analysis and simulation of 3D polycrystalline microstructures. Part II: Synthetic structure generation. *Acta Materialia*, 56(6):1274–1287, 2008.

[27] M A Groeber, M D Uchic, D M Dimiduk, Y Bhandari, and S Ghosh. A framework for automated 3D microstructure analysis and representation. *Journal of Computer-Aided Materials Design*, 14(1):63–74, 2007.

[28] D G Harlow, J Nardiello, and J Payne. The effect of constituent particles in aluminum alloys on fatigue damage evolution: Statistical observations. *International Journal of Fatigue*, 32(3):505 – 511, 2010. Symposium on Competing Failure Modes and Variability in Fatigue.

[29] D G Harlow, M Z Wang, and R P Wei. Statistical analysis of constituent particles in 7075-T6 aluminum alloy. *Metallurgical and Materials Transactions A*, 37(11):3367 – 3373, 2006.

[30] R Hill. Elastic properties of reinforced solids: Some theoretical principles. *Journal of the Mechanics and Physics of Solids*, 11(5):357–372, 1963.

[31] J D Hochhalter, D J Littlewood, R J Christ Jr, M G Veilleux, J E Bozek, A R Ingraffea, and A M Maniatty. A geometric approach to modeling microstructurally small fatigue crack formation: II. physically based modeling of microstructure-dependent slip localization and actuation of the crack nucleation mechanism in AA 7075-T651. *Modelling and Simulation in Materials Science and Engineering*, 18(4), 2010.

[32] J D Hochhalter, D J Littlewood, M G Veilleux, J E Bozek, , A M Maniatty, A D Rollett, and A R Ingraffea. A geometric approach to modeling microstructurally small fatigue crack formation: III. Development of a semi-empirical model for nucleation. *Modelling and Simulation in Materials Science and Engineering*, 2010. In preparation.

[33] M James. *A plane stress finite element model for elastic-plastic mode I/II crack growth.* PhD thesis, Kansas State University, 1998.

[34] S R Johnston, G P Potirniche, S R Daniewicz, and M F Horstemeyer. Three-dimensional finite element simulations of microstructurally small fatigue crack growth in 7075 aluminum alloy. *Fatigue and Fracture of Engineering Materials and Structures*, 29(8):597 – 605, 2006.

[35] Y Kim, S Sheehy, and D Lenhardt. Structure-life management: A survey of programs in the US Navy, the Canadian Forces, and the US Air Force. *Air Force Journal of Logistics*, XXIX(3/4):37–46, 2005.

[36] D A Koss and K S Chan. Fracture along planar slip bands. *Acta Metallurgica*, 28(9):1245 – 1252, 1980.

[37] B Kunkler, O Duber, P Koster, U Krupp, C-P Fritzen, and H-J Christ. Modelling of short crack propagation - Transition from stage I to stage II. *Engineering Fracture Mechanics*, 75(3-4):715 – 725, 2008. International Conference of Crack Paths.

[38] A Kuprat, A Khamayseh, D George, and L Larkey. Volume conserving smoothing for piecewise linear curves, surfaces, and triple lines. *Journal of Computational Physics*, 172(1):99–118, 2001.

[39] C Laird. The influence of metallurgical structure on the mechanisms of fatigue crack propagation. In *Fatigue Crack Propagation*, volume ASTM STP 415, pages 131–168. American Society for Testing and Materials, 1967.

[40] J Lankford, D L Davidson, and K S Chan. The influence of crack tip plasticity in the growth of small fatigue cracks. *Metallurgical Transactions A*, 15A:1579–1588, 1984.

[41] P J Laz and B M Hillberry. Fatigue life prediction from inclusion initiated cracks. *International Journal of Fatigue*, 20(4):263 – 270, 1998.

[42] C Li. Vector CTD analysis for crystallographic crack growth. *Acta Metallurgica et Materialia*, 38(11):2129 – 2134, 1990.

[43] X D Li. Micromechanical model of stage I to stage II crack growth transition for aluminum alloys. *Theoretical and Applied Fracture Mechanics*, 24(3):217 – 231, 1996.

[44] M Liao. Probabilistic modeling of fatigue related microstructural parameters in aluminum alloys. *Engineering Fracture Mechanics*, 76(5):668 – 680, 2009. Material Damage Prognosis and Life-Cycle Engineering.

[45] I L Lim, I W Johnston, S K Choi, and V Murti. An improved numerical inverse isoparametric mapping technique for 2D mesh rezoning. *Engineering Fracture Mechanics*, 41(3):417 – 435, 1992.

[46] P E Magnusen, R J Bucci, A J Hinkle, J R Brockenbrough, and H J Konish. Analysis and prediction of microstructural effects on long-term fatigue performance of an aluminum aerospace alloy. *International Journal of Fatigue*, 19(93):275 – 283, 1997.

[47] Y Mao, A M Gokhale, and J Harris. Computer simulations of realistic microstructures of coarse constituent particles in a hot-rolled aluminum alloy. *Computational Materials Science*, 37(4):543–556, 2006.

[48] K Matous and A M Maniatty. Finite element formulation for modelling large deformations in elasto-viscoplastic polycrystals. *International Journal for Numerical Methods in Engineering*, 60(14):2313 – 2333, 2004.

[49] F A McClintock. Considerations for fatigue crack growth relative to crack tip displacement. In J H Beynon, M W Brown, R A Smith, T C Lindley, and

B Tomkins, editors, *Engineering Against Fatigue*, pages 227–241, Rotterdam, Netherlands, 1999. A.A.Balkema.

[50] D L McDowell and F P E Dunne. Microstructure-sensitive computational modeling of fatigue crack formation. *International Journal of Fatigue*, 32(9):1521–1542, 2010.

[51] D L McDowell, K Gall, M F Horstemeyer, and J Fan. Microstructure-based fatigue modeling of cast A356-T6 alloy. *Engineering Fracture Mechanics*, 70(1):49 – 80, 2003.

[52] K J Miller. Metal fatigue - past, current and future. In *Proceedings of the Institution of Mechanical Engineers, Part C: Journal of Mechanical Engineering Science 1989-1996*, volume 205, pages 291–304, London, 1991. Professional Engineering Publishing.

[53] R H Moore, G S Rohrer, and S Saigal. Reconstruction and simplification of high-quality multiple-region models from planar sections. *Engineering with Computers*, 25(3):221–235, 2009.

[54] C R Myers, T Cretegny, N P Bailey, C S Chen, A J Dolgert, L O Eastgate, E Iesulauro, A R Ingraffea, M Rauscher, and J P Sethna. Software methodologies for multiscale descriptions of defects, deformation and fracture. In K Ravi-Chandar, editor, *Proceedings of the 10th International Conference on Fracture: Advances in Fracture Research*, pages CD–ROM, Honolulu, 2001.

[55] J B Cavalcante Neto, P A Wawrzynek, M T M Carvalho, L F Martha, and A R Ingraffea. An algorithm for three-dimensional mesh generation for arbitrary regions with cracks. *Engineering with Computers*, 17(1):75–91, 2001.

[56] G M Nielson and R Franke. Computing the separating surface for segmented data. In *Proceedings of the 8th Conference on Visualization 1997*, pages 229–233, Los Alamitos, CA, 1997. IEEE Computer Society Press.

[57] P Paris and F Erdogan. A critical analysis of crack propagation laws. *Journal of Basic Engineering, Transactions of the American Society of Mechanical Engineers*, pages 528–534, 1963.

[58] G Patton, C Rinaldi, Y Brechet, G Lormand, and R Fougeres. Study of fatigue damage in 7010 aluminum alloy. *Materials Science and Engineering: A*, 254(1-2):207 – 218, 1998.

[59] J Payne, G Welsh, R J Christ Jr, J Nardiello, and J M Papazian. Observations of fatigue crack initiation in 7075-T651. *International Journal of Fatigue*, 32(2):247 – 255, 2010.

[60] G P Potirniche and S R Daniewicz. Finite element modeling of microstructurally small cracks using single crystal plasticity. *International Journal of Fatigue*, 25(9-11):877 – 884, 2003.

[61] G P Potirniche, S R Daniewicz, and J C Newman Jr. Simulating small crack growth behaviour using crystal plasticity theory and finite element analysis. *Fatigue and Fracture of Engineering Materials and Structures*, 27(1):59 – 71, 2004.

[62] W H Press, W T Vetterling, S A Teukolsky, and B P Flannery. *Numerical Recipes in C++: The Art of Scientific Computing*. Cambridge University Press, New York, NY, 2002.

[63] J Qian, Y Zhang, W Wang, A C Lewis, M A S Qidwai, and A B Geltmacher. Quality improvement of non-manifold hexahedral meshes for critical feature determination of microstructure materials. *International Journal for Numerical Methods in Engineering*, 82(11):1406–1423, 2009.

[64] H Resk, L Delannay, M Bernacki, T Coupez, and R Loge. Adaptive mesh refinement and automatic remeshing in crystal plasticity finite element simulations. *Modelling and Simulation in Materials Science and Engineering*, 17(7), 2009.

[65] J R Rice, D E Hawk, and R J Asaro. Crack tip fields in ductile crystals. *International Journal of Fracture*, 42(4):301 – 321, 1990.

[66] F O Riemelmoser, P Gumbsch, and R Pippan. Dislocation modeling of fatigue cracks: An overview. *Materials Transactions*, 42(1):2 – 13, 2001.

[67] R O Ritchie and S Suresh. Some considerations on fatigue crack closure at near-threshold stress intensities due to fracture surface morphology. *Metallurgical Transactions A*, 13A:937–940, 1982.

[68] A D Rollett, R Campman, and D Saylor. Three dimensional microstructures: Statistical analysis of second phase particles in AA7075-T651. In *Materials Science Forum*, volume 519-521, pages 1–10, Switzerland, 2006. Trans Tech Publications Ltd.

[69] A D Rollett and P Manohar. The Monte Carlo method. In D Raabe, F Roters, F Barlat, and L Q Chen, editors, *Continuum Scale Simulation of Engineering Materials*, pages 77–114. Wiley-VCH, Weinheim, Germany, 1 edition, 2004.

[70] A D Rollett, D Saylor, B S El-Dasher, A Brahme, S-B Lee, C Cornwell, and R Noack. Modeling polycrystalline microstructures in 3D. In S Ghosh, J C Castro, and J K Lee, editors, *Materials Processing and Design: Modeling, Simulation and Applications - NUMIFORM 2004 - Proceedings of the 8th International Conference on Numerical Methods in Industrial Forming Processes*, volume 712, pages 71–77, 2004.

[71] D M Saylor, J Fridy, B S El-Dasher, K-Y Jung, and A D Rollett. Statistically representative three-dimensional microstructures based on orthogonal observation sections. *Metallurgical and Materials Transactions A*, 35A(7):1969–1979, 2004.

[72] J Schreiner, C E Scheidegger, and C T Silva. High-quality extraction of isosurfaces from regular and irregular grids. *IEEE Transactions on Visualization and Computer Graphics*, 12(5):1205–1212, 2006.

[73] M M Shenoy, R S Kumar, and D L McDowell. Modeling effects of nonmetallic inclusions on LCF in DS nickel-base superalloys. *International Journal of Fatigue*, 27(2):113 – 127, 2005.

[74] I Simonovski and L Cizelj. The influence of the grain structure size on microstructurally short cracks. *Journal of Engineering for Gas Turbines and Power*, 131(4), 2009.

[75] I Simonovski, K-F Nilsson, and L Cizelj. Crack tip displacements of microstructurally small cracks in 316L steel and their dependence on crystallographic orientations of grains. *Fatigue and Fracture of Engineering Materials and Structures*, 30(6):463 – 478, 2007.

[76] S D Sintay. *Statistical Microstructure Generation and 3D Microstructure Geometry Extraction*. PhD thesis, Carnegie Mellon University, 2010.

[77] S Suresh. *Fatigue of Materials*. Cambridge University Press, Cambridge, UK, 1998.

[78] S Swaminathan and S Ghosh. Statistically equivalent representative volume elements for unidirectional composite microstructures: Part II - With interfacial debonding. *Journal of Composite Materials*, 40(7):605–621, 2006.

[79] S Swaminathan, S Ghosh, and N J Pagano. Statistically equivalent representative volume elements for unidirectional composite microstructures: Part I - Without damage. *Journal of Composite Materials*, 40(7):583–603, 2006.

[80] R G Tryon and T A Cruse. Probabilistic mesomechanical fatigue crack nucleation model. *Journal of Engineering Materials and Technology*, 119(1):65 – 70, 1997.

[81] R G Tryon and T A Cruse. A reliability-based model to predict scatter in fatigue crack nucleation life. *Fatigue and Fracture of Engineering Materials and Structures*, 21(3):257 – 267, 1998.

[82] M G Veilleux, J D Hochhalter, J E Bozek, and A R Ingraffea. A geometric approach to modeling microstructurally small fatigue crack formation: V. Simulation of material heterogeneity and crack size influence on propagation mechanisms after nucleation. *Modelling and Simulation in Materials Science and Engineering*, 2010. In preparation.

[83] C C L Wang. Direct extraction of surface meshes from implicitly represented heterogeneous volumes. *Computer-Aided Design*, 39(1):35–50, 2007.

[84] L Wang, S R Daniewicz, M F Horstemeyer, S Sintay, and A D Rollett. Three-dimensional finite element analysis using crystal plasticity for a parameter study of microstructurally small fatigue crack growth in a AA7075 aluminum alloy. *International Journal of Fatigue*, 31(4):651 – 658, 2009.

[85] P A Wawrzynek, B J Carter, and A R Ingraffea. Advances in simulation of arbitrary 3D crack growth using FRANC3D/NG. In *Proceedings of the 12th International Conterence of Fracture*, pages CD–ROM, Ottawa, Canad, 2009.

[86] H Weiland, J Nardiello, S Zaefferer, S Cheong, J Papazian, and D Raabe. Microstructural aspects of crack nucleation during cyclic loading of AA7075-T651. *Engineering Fracture Mechanics*, 76(5):709 – 714, 2009. Material Damage Prognosis and Life-Cycle Engineering.

[87] Y Xue, H El Kadiri, M F Horstemeyer, J B Jordon, and H Weiland. Micromechanisms of multistage fatigue crack growth in a high-strength aluminum alloy. *Acta Materialia*, 55(6):1975 – 1984, 2007.

[88] Y Xue, D L McDowell, M F Horstemeyer, M H Dale, and J B Jordon. Microstructure-based multistage fatigue modeling of aluminum alloy 7075-T651. *Engineering Fracture Mechanics*, 74(17):2810 – 2823, 2007.

[89] T Zhai, A J Wilkinson, and J W Martin. A crystallographic mechanism for fatigue crack propagation through grain boundaries. *Acta Metallurgica*, 48(20):4917 – 4927, 2000.

[90] Y Zhang and C Bajaj. Adaptive and quality qudrilateral/hexahedral meshing from volumetric data. *Computer Methods in Applied Mechanics and Engineering*, 195(9-12):942–960, 2006.

[91] Y Zhang, C Bajaj, and B-S Sohn. 3D finite element meshing from imaging data. *Computer Methods in Applied Mechanics and Engineering*, 194(48-49):5083–5106, 2005.

[92] Y Zhang, C Bajaj, and G Xu. Surface smoothing and quality improvement of quadrilateral/hexahedral meshes with geometric flow. *Communications in Numerical Methods in Engineering*, 25(1):1–18, 2007.

[93] Y Zhang, T J R Hughes, and C L Bajaj. An automatic 3D mesh generation method for domains with multiple materials. *Computer Methods in Applied Mechanics and Engineering*, 199(5-8):405 – 415, 2010. Computational Geometry and Analysis.

[94] Y Zhang, G Xu, and C Bajaj. Quality meshing of implicit solvation models of biomolecular structures. *Computer Aided Geometric Design*, 23(6):510–530, 2006.